THE RATIONAL DESIGN OF **META-IMPLANTS** USING A COMBINATION OF **AUXETIC** AND **CONVENTIONAL** MICROSTRUCTURES

Eline (H.M.A.) Kolken
STUDENT NO. 4154363
BIOMEDICAL ENGINEERING - TISSUE BIOMECHANICS AND IMPLANTS

SUPERVISED BY

Dr. Amir A. Zadpoor
DEPARTMENT OF BIOMATERIALS AND TISSUE BIOMECHANICS ● TU DELFT

Ir. Shahram Janbaz
DEPARTMENT OF BIOMATERIALS AND TISSUE BIOMECHANICS ● TU DELFT

TU Delft

June 14, 2017

TU Delft

THE RATIONAL DESIGN OF META-IMPLANTS USING A COMBINATION OF AUXETIC AND CONVENTIONAL MICROSTRUCTURES

BY

Eline (H.M.A.) Kolken

IN PARTIAL FULFILMENT OF THE REQUIREMENTS FOR THE DEGREE OF

MASTER OF SCIENCE

IN BIOMEDICAL ENGINEERING

AT THE **DELFT UNIVERSITY OF TECHNOLOGY**,

TO BE DEFENDED ON WEDNESDAY 14TH OF JUNE, 2017 AT 15:00

SUPERVISED BY

Dr.Ir. Amir A. Zadpoor

DEPARTMENT OF BIOMATERIALS AND TISSUE BIOMECHANICS ● TU DELFT

Ir. Shahram Janbaz

DEPARTMENT OF BIOMATERIALS AND TISSUE BIOMECHANICS ● TU DELFT

THESIS COMMITTEE

Prof.Dr.Ir. Harrie H. Weinans

DEPARTMENT OF ORTHOPEDICS ● UNIVERSITY MEDICAL CENTER UTRECHT

Dr.Ir. Dick H. Plettenburg

DEPARTMENT OF BIOMECHANICAL ENGINEERING ● TU DELFT

Dr.Ir. Gerwin Smit

DEPARTMENT OF BIOMECHANICAL ENGINEERING ● TU DELFT

TU Delft

TUDelft

Preface

Total hip replacements (THR) are among the most common orthopedic procedures carried out to date. Although initially intended to treat the elderly, their increasing utilization among the younger population changes its requirements. These individuals do not only have special needs, they will most certainly outlive their implants too. Where today's implants last for more than 20 years, the implants of tomorrow should ideally last a lifetime. It is therefore of utter importance to study the implant's performance, and innovate towards higher quality and less revisions.

I would therefore like to thank Amir Zadpoor for introducing me to this thesis subject. Even though the project did not appeal to me from the very beginning, I am more than satisfied now that it is finished. The novelty of the work is what interested me the most, since this could really make a difference. I would also like to thank him for sharing his expertise, and providing me with valuable feedback. The road has been bumpy, especially timewise, but his continuous support definitely kept me going.

This road may have turned into a highway to hell if it was not for Wim Veldt, Sander Leeflang and Karel Litaert who helped me out with the technical details of my specimens and experiments. I would like to thank Wim for his patience, his humor, and most importantly his support during the process of building my own experimental set-up. Sander has been of great value during the production of my specimens. Without his 3D printing expertise, I would not have been able to print these complex and delicate structures. Subsequently, Karel Litaert helped me out with the second batch of hybrid mechanical metamaterials, when my first attempt to test them without the titanium flanges failed. Together we found a way to adjust the designs and print them accordingly.

Furthermore, I would like to thank Berthil Grashof and Gertjan Mulder for their continuous support during the mechanical evaluation of my specimens. DIC calibration appeared to be a huge challenge, but thanks to their patience and expertise I have managed to obtain a valuable set of results. Additionally, I would like to thank Johan Boender and Misja Huizinga for their technical support during the experiments. I felt more than welcome in the Aeroplane hall at the faculty of Aerospace Engineering.

I would not have made it through this bumpy ride, if it was not for my family and friends. They kept me motivated when the SLM machine broke down, more than twice, and encouraged me to have faith in myself. A special thanks to my boyfriend Shannon, who managed to keep me calm when things got beyond my control. I am forever grateful.

Last, but definitely not least, I would like to thank Shahram Janbaz for his daily support. He really surprised me with his daily enthusiasm and novel ideas. There is no road too heavy.

~ The road may have been rough, but the results made it all worthwhile ~

Abstract

With the aging population growing, the increasing prevalence of osteoarthritis (OA) seems inevitable. As a result, the number of joint replacements is expected to grow substantially within the next decade. Today's hip replacements have the potential to function for more than 20 years, but due to risk factors such as aseptic loosening, the younger patients will most certainly outlive their prostheses. Aseptic loosening refers to the mechanical failure of the implant-bone interface, which may arise as the end result of stress shielding or improper design. In places where the bone is understressed for prolonged periods of time, bone resorption will set in, which can eventually lead to implant failure. Optimization of this bone-implant interface is therefore of utter importance to increase the implant's longevity. Recent advances in additive manufacturing (AM) have enabled the fabrication of highly-complex micro-architectures, which can be designed to exhibit novel mechanical properties at the macroscale. The development of these mechanical metamaterials has paved the way for personalized, life-lasting implants. This explorative study aimed to investigate the mechanical properties of 3D AM (hybrid) mechanical metamaterials and their potential to improve the mechanical fixation of off-axially loaded AM meta-implants, using the mechanical responsiveness of bone. The mechanical properties of six different 3D AM mechanical metamaterials were assessed during axial compression, with the help of Digital Image Correlation (DIC). Combinations of mechanical metamaterials were made to obtain novel 3D hybrid mechanical metamaterials, for which the expansions and initiated strain distributions were determined using DIC, upon off-axial compression. Finally, five different meta-implants (femoral stems) were designed. A compression was applied at the femoral head to examine the strain distributions in the surrounding, bone-mimicking foam blocks. Hybrid meta-implant Type 2 showed the most continuous compressive strain distribution, with a considerably different lateral strain profile compared to the current generation of femoral stems. These studies therefore demonstrate the potential of applying hybrid mechanical metamaterials in off-axially loaded meta-implants, such as the femoral stem, to initiate bilateral strains and potentially stimulate osseointegration at the bone-implant interface.

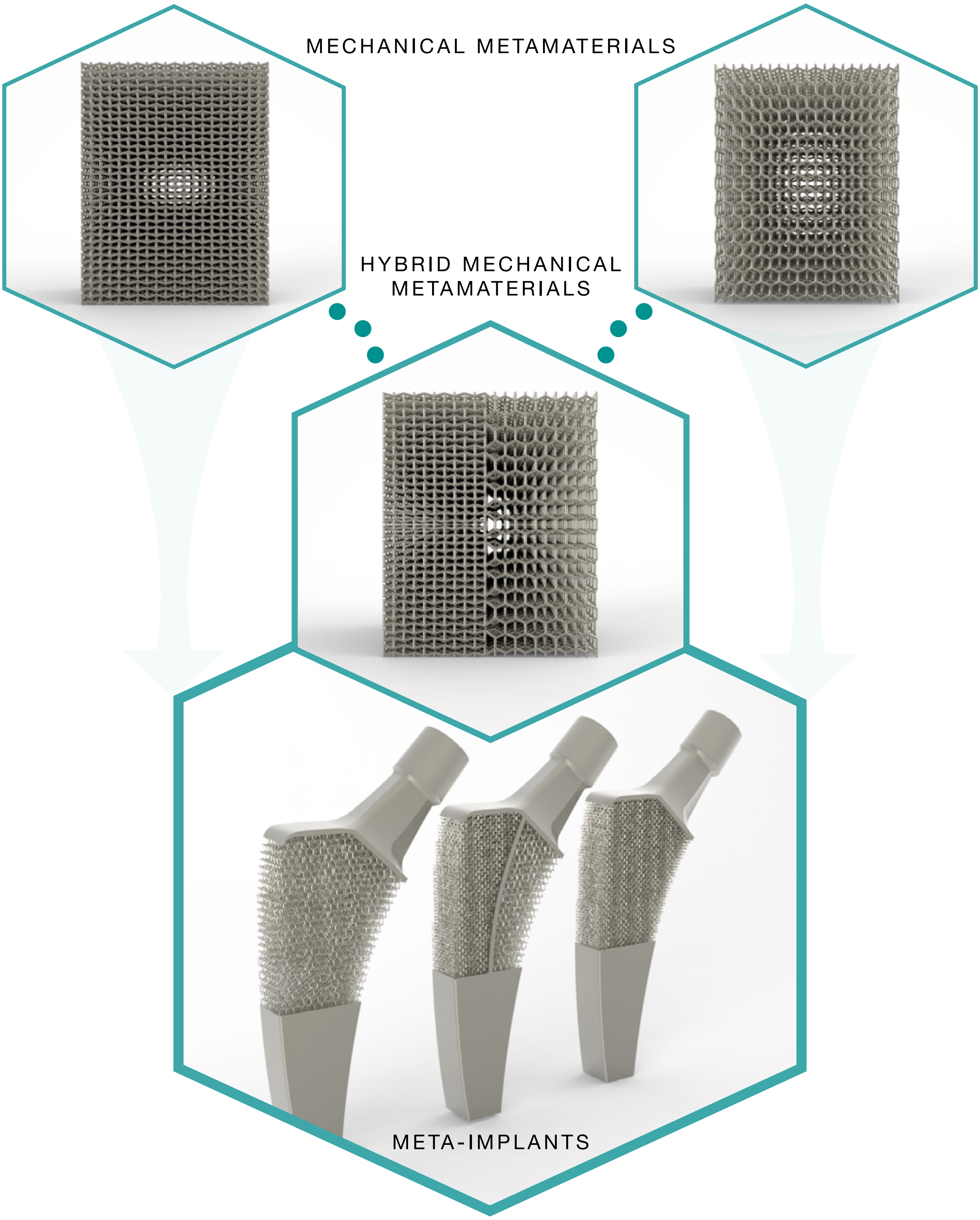
MECHANICAL METAMATERIALS
HYBRID MECHANICAL METAMATERIALS
META-IMPLANTS

CONTENTS

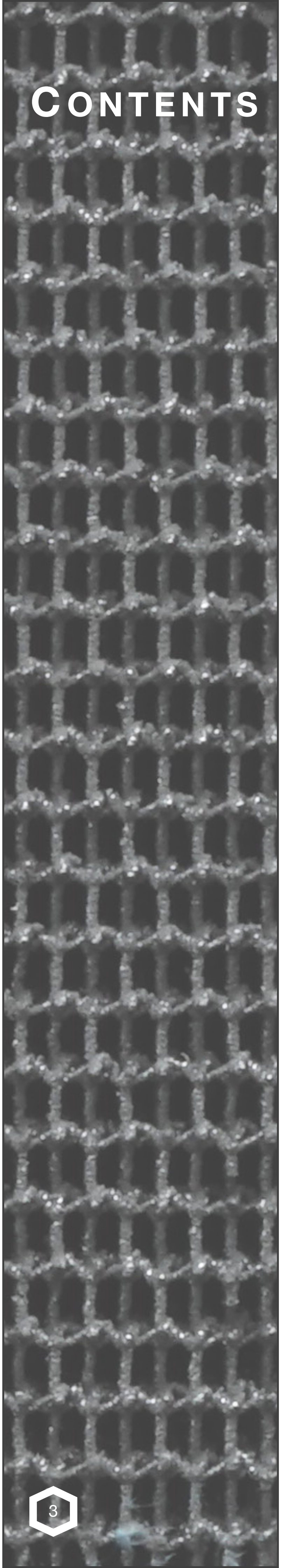

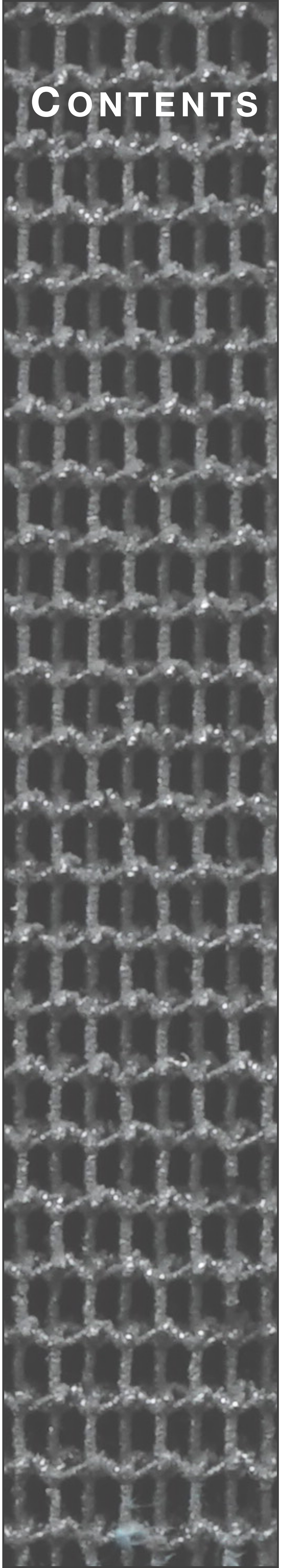

CONTENTS

1. Introduction

Total hip replacements (THR) are among the most common orthopedic procedures carried out to date, in 2011 alone, more than 1.5 million people received a THR in OECD countries.[1] Their incidence is expected to double within the next decade[2], as a direct consequence of the growing aging population and the increasing utilization among younger patients.[3] Today's implants have the potential to function for more than 20 years[4,5], but their success rate goes down with time. Statistics show that 10 years after surgery 5-20% of the patients will be in need of a revision[6,7], and this number is projected to grow substantially[2]. Improvements in implant design and surgical techniques have reduced the incidence of deep sepsis, dislocation and fracture, but aseptic loosening still accounts for more than half of the revisions carried out to date.[8-10]

The term aseptic loosening refers to the mechanical failure of the implant-bone interface, which primarily arises as the end result of inflammatory bone loss.[8] Subsequently, it may be the result of micro motion, stress shielding or improper design, which eventually leads to inadequate mechanical fixation.[11,12] Stress shielding has since been extensively studied[13-15], and designs have been proposed to limit this phenomenon[16,17]. Most studies have been focusing on the stiffness mismatch between implant and bone, whereas research on the implant's Poisson's effect[18] is ignored. In fact, the lateral side of a femoral stem will tend to move away from the bone-implant interface upon loading at the femoral head. This can be explained by the tensile forces imposed by the applied bending moment. Just like stress shielding, this will reduce the bone load. As a result, the bone will adapt to a lack of external loading, and bone wastage will set in once the bone is understressed for prolonged periods of time[19,20]. This may lead to serious complications, including implant failure. Subsequently, bone atrophy will create an unfavorable basis for a revision surgery, for which sufficient bone stock is needed.[16,21]

The emerging concept of mechanical metamaterials offers a great route of attaining materials with unusual mechanical properties and advanced functionalities.[22,23] The term "metamaterials' was initially used within the field of electromagnetism and optics[24-26], but today refers to all materials engineered to exhibit novel properties. Their extraordinary mechanical properties include negative elasticity, negative compressibility and negative Poisson's ratio (NPR). The latter are better known as auxetic mechanical materials, and are perhaps the most widely studied.[23] Stretching a piece of auxetic material will result in a lateral expansion instead of contraction. The macro-scale properties of metamaterials originate from their micro-architecture, which can be rationally designed to exhibit specific mechanical properties.[23] Metamaterials are therefore also known as "designer materials", which due to recent advances in additive manufacturing (AM) can be fabricated fairly easily. Mechanical metamaterials are increasingly utilized in the field of soft-robotics, acoustics and biomedicine.[27,28] By adding an extra "nano" dimension to the arbitrarily complex three-dimensional (3D) microstructures, meta-biomaterials are created. Extraordinary combinations of mechanical, mass transport and biological properties originate from their 3D microstructure[29,30], whereas the nano-topology can be used to communicate with cells and enhance tissue regeneration.[31]

The development of these mechanical metamaterials has paved the way for personalized, life-lasting implants. Together with bone tissue regeneration, osseointegration is among the most important goals in the design of orthopedic implants.[32] Implants are considered osseointegrated when there is a tight connection between the implant surface and the surrounding bone, as a result of direct bone apposition within the defined healing period.[33] Fibrous encapsulation should therefore be prevented, which may be the direct result of a bio-incompatible material, and prevents the bone cells from adhering to the implant's surface.[33] Therefore, to enhance osseointegration in femoral stems, the implant should be in continuous contact with the bone To reverse the laterally observed shrinkage in the femoral stem as a result of the Poisson's effect, a combination of auxetic and conventional (positive Poisson's ratio) mechanical metamaterials should be utilized. Despite their long-term solo existence[18,34], experimental research on hybrid combinations of negative and positive Poisson's ratio materials is rare.[35,36] This explorative study therefore aimed to investigate the mechanical properties of rationally designed 3D AM (hybrid-) mechanical metamaterials and their potential to improve the mechanical fixation of off-axially loaded orthopedic meta-implants, using the mechanical responsiveness of bone. Optimization of the meta-implant for optimal bone regeneration falls beyond the scope of this project.

2. Materials and Methods

2.1 Rational design of 3D lattice structures

The first part of this research involves the design of mechanical metamaterials: re-entrant hexagonal honeycomb structures and conventional hexagonal honeycomb structures. Subsequently, re-entrant hexagonal honeycombs and conventional hexagonal honeycombs were combined to form so-called "hybrid" mechanical metamaterials. These hybrid mechanical metamaterials were later implemented in a femoral stem, later referred to as a "meta-implant". The designs were created in Solidworks 2016 3D CAD software (Dassault Systemes, Waltham, USA) and the meta-implants were subsequently edited in the 3D modelling software Materialise 3-Matic (Materialise, Leuven, Belgium).

2.1.1 Mechanical metamaterials

A recent publication on the topology-property relationship in auxetic mechanical metamaterials revealed that the re-entrant angle (*θ*, Figure 1) strongly influences the mechanical properties of re-entrant hexagonal structures.[23,37] Subsequently, cell rib length ratios (*a/b*, Figure 1) were also found to influence the Poisson's ratio. The cell rib lengths were chosen out of convenience, and with ratios ranging between 1.0 and 1.5, a maximum NPR should be reached with a re-entrant angle of about 30 degrees.[37]

A re-entrant angle of 15 degrees was chosen as the initial value and two designs were systematically added, (+/-) 10 degrees from this starting point. The 3D re-entrant hexagonal structures were formed by arraying the 2D re-entrant cells ad depicted in Figure 1a. This resulted in a variety of structures with different mechanical properties. To minimize production variability, the size of the structures was adjusted to fit four samples on one build plate. With a cell width of 5 mm the base was formed by a 5 x 5 cell array (Figure 1a). The height of the unit cell was designed at 2.5 mm for design 1 and 2, but was altered to 3.5 mm to accommodate the re-entrant angle in design 3. The number of cell layers was adjusted to approach a total height of 25 mm, which made the samples approach a cube of 25 x 25 x 25 mm. Ribs were added on both sides of the structure, to efficiently transfer the forces to those vertices floating above/underneath the horizontal plane. The final designs were exported as .STL files with a coarse resolution and a binary output.

The same rational approach was used to design the 3D conventional hexagonal honeycombs (Figure 1b). Starting +15 degrees from a 90-degree angle, a deviation of (+/-) 10 degrees was used to create the second and third design. For a proper comparison to be made, the conventional structures were made to approach the same cube of 25 x 25 x 25 mm. The final designs were exported as .STL files with a coarse resolution and a binary output.

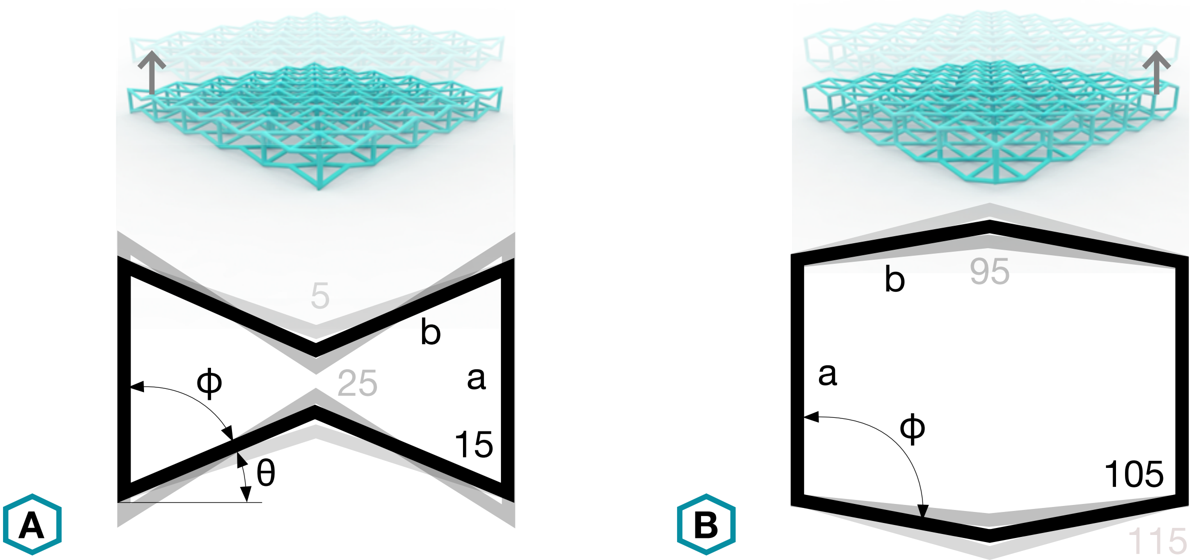

Figure 1: Design of mechanical metamaterials with re-entrant angle *θ*, internal angle *ϕ* and rib length ratio *a/b*. (A) Re-entrant unit cell with its repetitive array in 3D (B) Conventional unit cell with its repetitive array in 3D.

Table 1: Solidworks dimensions of auxetic and conventional mechanical metamaterials.

Design Type	Internal angle ϕ (°)	a (mm)	b (mm)	H x W x D (mm)
Auxetic Type 1	75	2.5	2.59	24.82 x 25.7 x 25.7
Auxetic Type 2	85	2.5	2.51	25.65 x 25.7 x 25.7
Auxetic Type 3	65	3.5	2.76	27.21 x 25.7 x 25.7
Conventional Type 1	105	2.5	2.59	23.21 x 25.7 x 15.7
Conventional Type 2	115	2.5	2.76	27.20 x 25.7 x 15.7
Conventional Type 3	95	3.5	2.51	15.03 x 25.7 x 25.7
Strutt thickness	350 μm			

The above-mentioned rational design process resulted in a total of six different mechanical metamaterials, three re-entrant types (A1, A2 and A3) and three conventional Types (C1, C2 and C3), of which the exact Solidworks dimensions can be found in Table 1. The terms auxetic and re-entrant have been used interchangeably to refer to NPR materials.

2.1.2 HYBRID MECHANICAL METAMATERIALS

According to the laws of modern mechanics, a hybrid combination of re-entrant and conventional unit cells should create beneficial effects in bending situations where expansion on both sides of the structure is desired. The novelty of this structure lies in the application of re-entrant unit cells on the lateral side of a medially loaded structure. The dimensions of the aforementioned auxetic mechanical metamaterials were therefore used as a starting point in the rational design process of these hybrid mechanical metamaterials. The connection between the two types of mechanical metamaterials can either be done through a so-called "transitional region" or through a direct connection established by the addition of continuous vertical ribs (Figure 2, Type 4, 5 and 6).

The presence of a transitional region was used to determine the composition of the hybrid structure. The conventional cells were given the same vertical rib length (*a*), total cell width and total cell depth as their auxetic counterpart on the other side of the construct. Two "fish-like" transitional cells were created, connecting three re-entrant cells to one conventional cell (Figure 2). These choices narrowed down the design space of the conventional cells, and to acquire the stereotypical honeycomb pattern, the internal angle could only take on one value (Table 2). Just like the mechanical metamaterials, the hybrids were obtained by arraying the corresponding 2D unit cells. Transitional cells were manually connected to the next one in line (Figure 2). A 5 x 10 cell array was used as a base for both sides of the structure, connected by a 1 x 10 transitional array this resulted in a total base of 11 x 10 unit cells.

The above-mentioned design choices resulted in six designs (Figure 2). Design Types 4, 5 and 6 have the same geometrical dimensions as design Types 1, 2 and 3, respectively, but lack the transitional region. Instead, both types of mechanical metamaterials were connected through continuous vertical ribs. This change led to a decrease in total sample width by 1.25 mm, which corresponds to half a unit cell. A summary of the dimensions has been presented in Table 2.

Table 2: Solidworks dimensions of hybrid mechanical metamaterials with A = auxetic and C = conventional geometry.

Design Type	Internal angle ϕ (°)		a (mm)		b (mm)		H x W x D (mm)
	A	C	A	C	A	C	
Hybrid Type 1 (4)	75	114.90	1.25	1.25	1.30	1.38	25.7 x 26.43 x 25.7
Hybrid Type 2 (5)	85	129.52	1.25	1.25	1.26	1.62	25.7 x 26.43 x 25.7
Hybrid Type 3 (6)	65	115.05	1.75	1.75	1.38	1.38	25.7 x 26.43 x 25.7
Hybrid Type 4	75	114.90	1.25	1.25	1.30	1.38	25.7 x 25.18 x 25.7
Hybrid Type 5	85	129.52	1.25	1.25	1.26	1.62	25.7 x 25.18 x 25.7
Hybrid Type 6	65	115.05	1.75	1.75	1.38	1.38	25.7 x 25.18 x 25.7
Strutt thickness	350 μm						

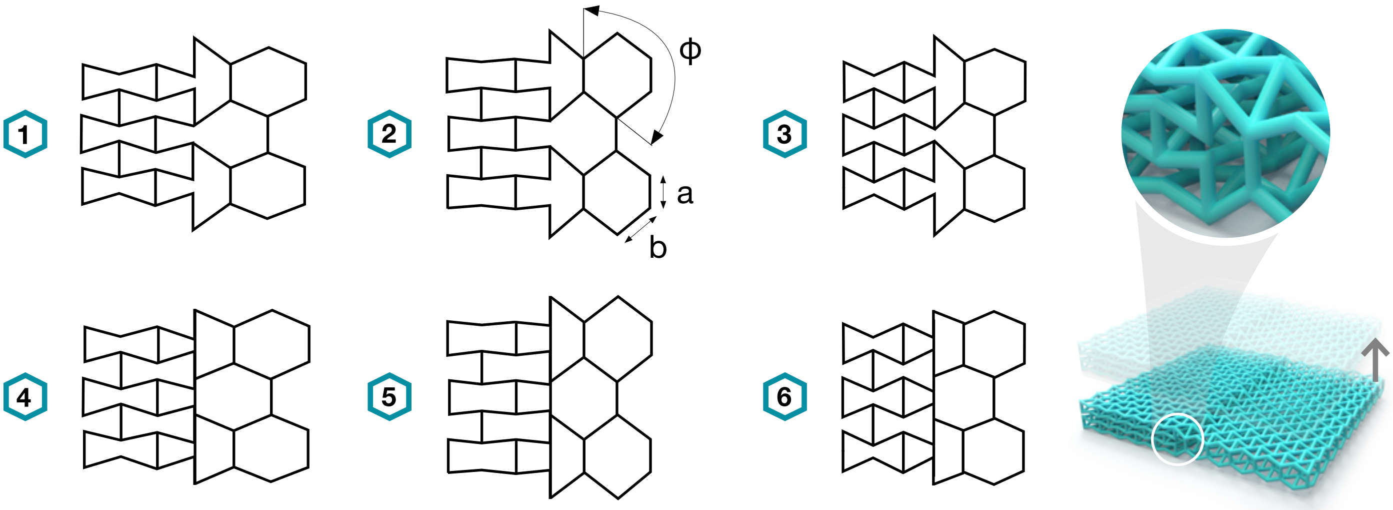

Figure 2: Design of hybrid mechanical metamaterials with internal angle *ϕ* and rib length ratio *a*/*b*. (1) Type 1 (75-degree auxetic side with a transitional region). (2) Type 2 (85-degree auxetic side with a transitional region). (3) Type 3 (65-degree auxetic side with a transitional region). (4) Type 4 (Type 1 without a transitional region). (5) Type 5 (Type 2 without a transitional region). (6) Type 6 (Type 3 without a transitional region). The 3D repetitive array of Hybrid Type 1 is shown on the right.

To ease the printing process, the samples were scaled to 50% to approach the 25 x 25 x 25 mm cube. Consequently, the total cell size decreased by 50% and therefore more closely resembled the final application as a bone-substituting material. Additionally, a 5-mm thick flange was added to the top and bottom, to enable off-axial loading on the conventional side of the structure. A ridge was added to accommodate a steel cylinder, which will enable the load to be uniformly distributed along the depth of the structure (Figure 6b).

2.1.3 META-IMPLANTS

One of the applications that would theoretically benefit from the bilateral expansion described in section 2.1.2, is the femoral stem. Today's implants have the potential to function for more than 20 years[4,5], but aseptic loosening is one of the reasons this does not happen in 5-20% of the patients.[6,7] Aseptic loosening may be the result of micro motion, stress shielding or improper design, which eventually leads to inadequate mechanical fixation.[11,12] Bilateral expansion would stress the surrounding bone and therefore mitigate stress shielding.[19,38]

To prove this concept, at least three designs were needed. Two control meta-implants were designed, which are either fully filled with a conventional mechanical metamaterial (Figure 3a) or an auxetic mechanical metamaterial (Figure 3c). The former represents the current generation of femoral stems with a positive Poisson's ratio. The hybrid meta-implant contains two porous subvolumes (Figure 3b), a medial and a lateral compartment. The medial sub volume is filled with a conventional mechanical metamaterial, whereas the lateral sub volume is filled with an auxetic mechanical metamaterial.

Based on the results of the previously described auxetic -, conventional - and hybrid mechanical metamaterials, the decision was made to proceed with Hybrid Type 6. The control meta-implants were therefore given the corresponding geometrical dimensions of the unit cells involved (Table 2). Two designs were added to explore the effects of a solid core (Figure 3d) and a 70/30 ratio of re-entrant vs. conventional unit cells (Figure 3f) on the bilateral expansion.

The rational design of the meta-implants was inspired by the Zimmer Fitmore system.[39] This system consists of cementless, bone-preserving implants of which the proximal surface is treated with a Ti-plasma coating to enhance bone ingrowth. The overall shape of the implant was designed in SolidWorks, and in contrast to the trapezoidal cross-section of the Fitmore stem, the design was given a square cross-section to ease clamping in the experimental set-up. The volume enclosed by the Ti-plasma coating was separated to be filled with a hybrid mechanical metamaterial using Materialise 3-Matic (Materialise, Leuven, Belgium). The re-entrant hexagonal unit cell and the conventional hexagonal unit cell were designed and added to the program's unit cell library. The lightweight module of the program was used to fill the proximal volume with the given unit cells, creating a unit graph, which could then be exported to .STL given the desired thickness of the struts.

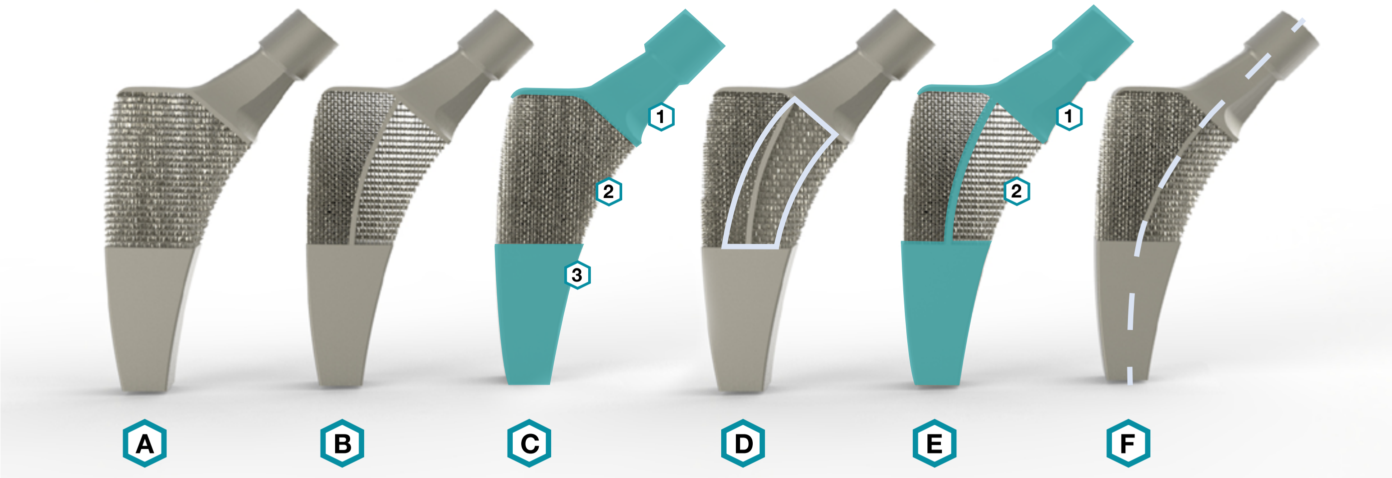

Figure 3: Meta-implant designs. (A) Control Type 1 with conventional hexagonal honeycomb cells. (B) Hybrid Type 1 with a 50/50 division. (C) Control Type 2 with re-entrant hexagonal honeycomb cells, showing the different .STL parts: (1) Top, (2) Porous region, (3) Bottom. (D) Hybrid Type 2 with a 50/50 division and a solid core. (E) Hybrid Type 1 showing the different .STL parts: (1) Top-middle-Bottom, (2) Porous region. (F) Hybrid Type 3 with a 70/30 division, following the implant's centerline.

A hole was made at the bottom of the stem to mimic the distal fixation of a cementless femoral stem.

Due to the complexity of the design, the meta-implants had to be divided into several .STL files in order for them to be downloaded into the building preparation software RDesigner (Realizer GmbH, Borchen, Germany). The controls were separated into three different .STL files; the top, the porous region and the bottom (Figure 3C). The hybrid meta-implants could be separated into two .STL files (Figure 3E), since the bottom and top are connected through a continuous vertical wall marking the border between the two mechanical metamaterials. All of the parts were manually cleared from any mesh defects using the Remeshing functions of Materialise 3-Matic.

2.2 ADDITIVE AND SUBTRACTIVE MANUFACTURING

For the actual realization of the designs, additive and subtractive manufacturing techniques have been used. The following paragraphs thoroughly describe these production processes.

2.2.1 SELECTIVE LASER MELTING

The powder bed fusion process of selective laser melting was used to manufacture the 3D lattice structures (Figure 4). As its name suggests, a high-power laser beam selectively melts metal particles by scanning cross-sections on the surface of a powder bed.[40] Having fulfilled one full cross-section, the powder bed is lowered by one layer thickness, after which a new spread of metal powder is added.[40] This process will be repeated until a fully dense, three-dimensional metallic part is created. Since its commercial introduction in the late 1990s, the process has been widely applied in various high-value added industries, including medicine.[41]

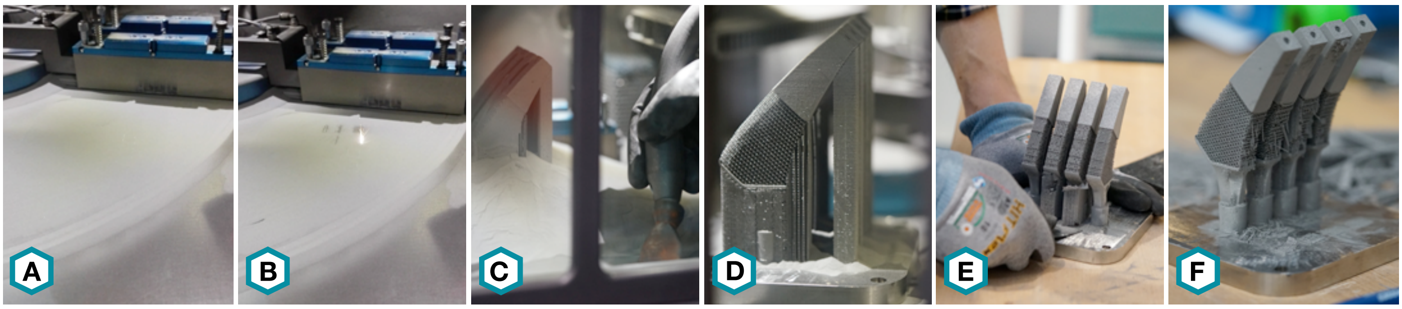

Figure 4: Process of Selective Laser Melting. (A) A fresh layer of Ti-6Al-4V powder is laid down by the wiper. (B) Powder particles are selectively melted by a high-power laser. (C) After printing, the excess powder is removed using a vacuum cleaner. (D) Build plate with parts and support structures. (E) The supports are carefully cut loose. (F) Build plate with parts and without the support structures.

2.2.1.1 MECHANICAL METAMATERIALS

Before the actual synthesis of the mechanical metamaterials, the .STL files were imported into RDesigner software (Realizer GmbH, Borchen, Germany) for building preparation. Four specimens of each design were built using a commercially available SLM125 Selective Laser Melting (SLM) machine (Realizer GmbH, Borchen, Germany). The SLM machine was equipped with a YLM-400-AC Ytterbium fiber laser (IPG Photonics Corporation, Oxford, USA) with the ability to emit 400 W of radiation in the wavelength range of 1070 ± 10 nm. As a feedstock, plasma-atomized, spherical Ti-6Al-4V ELI (Extra Low Interstitials) grade 23 powder (ASTM B348), with a particle size range of 10 to 45 µm, was acquired from AP&C (AP&C Advanced Powders and Coatings Inc., Boisbriand, Canada). This grade is the high purity variant of Ti-6Al-4V and is particularly useful in the medical industry for its high strength, light weight, good corrosion resistance and outstanding damage tolerance.[42] During fabrication, the building chamber was kept under argon atmosphere ([O^2] = 0.1-0.2%) and the mild steel building substrate was kept constant at 100 °C.

The specimens were built with a slice distance of 50 µm in a position where its basal plate was tilted 45° on the x-axis and 35° on the y-axis, relative to the slice plane (Figure 5). In this manner, any critical overhanging in the structure was avoided. The outer structure was manufactured with a laser current of 1100 mA, while exposure time and point distance were kept at 20 µs and 10 µm, respectively. The hatching of the internal structure was fabricated with a hatch distance of 0.15 mm and its hatch direction rotated 90° every subsequent slice. The laser current was set at 1100 mA while exposure time and point distance were kept at 5 µs and 10 µm, respectively.

The standard RDesigner point generator was used to create the support structures. The laser current was set at 1000 mA and exposure time was kept at 200 µs to create a structure strong enough to maintain the integrity of the specimen during building, but weak enough to be easily removed afterwards. The point generator selects all surfaces up till a certain angle threshold to be supported, which means surfaces within the core of the lattice structure are not excluded. This makes support removal impossible, which is why additional phantom designs were prepared in Solidworks. All struts were cut from the original structure, except the ones located on the three outer planes facing the build plate. The designs were exported as .STL files and imported into RDesigner where they were positioned and rotated to exactly overlap their parent structure. The scan definitions of the outer and the internal structures were deleted, after which the support structure could be generated. This way the support structure will support the three planes of the phantom facing the build plate, carrying the specimen that can now be manufactured without internal supports. The phantom structure itself was not build as the scan definitions were deleted.

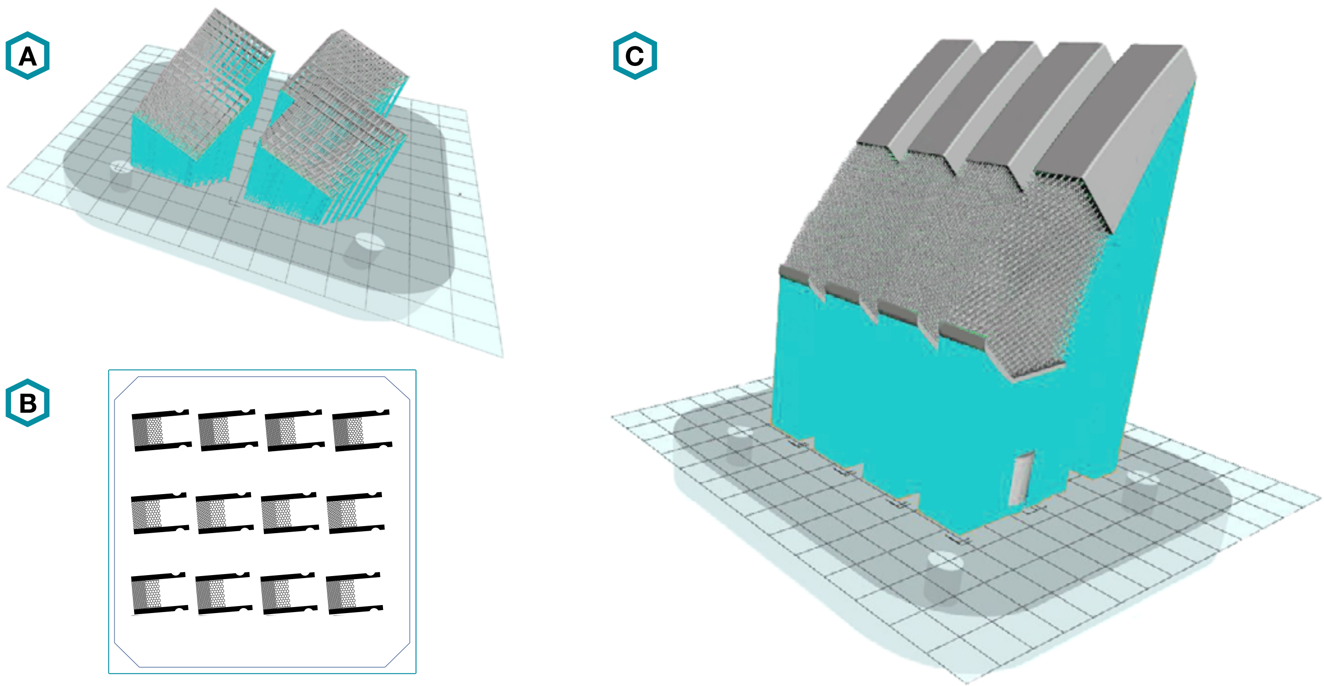

Figure 5: 3D-printing lay-outs with supports structures. (A) Tilted printing configuration of mechanical metamaterials. (B) Top view of 3D-systems' printing configuration of hybrid mechanical metamaterials. (C) Printing configuration of meta-implants.

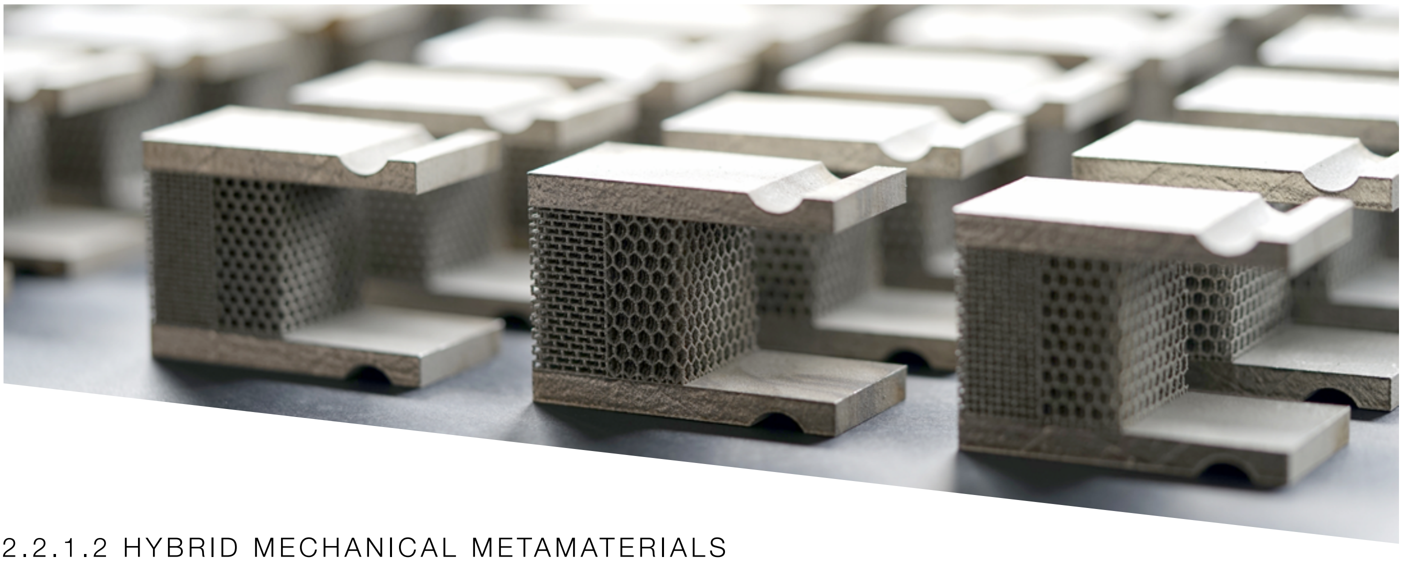

2.2.1.2 HYBRID MECHANICAL METAMATERIALS

Just like the mechanical metamaterials, the hybrid mechanical metamaterials were first prepared in a data preparation and .STL editor software, this time in Magics (Materialise, Leuven, Belgium) and DMP Control software (3D Systems, Leuven, Belgium). The job lay-out has been presented in Figure 5b, which shows the top view of the build plate. Eight specimens were built per hybrid design, using a Prox DMP 320 machine (3D systems), which complies with ASTM F3001 standards. Amongst other things, this standard lists the chemical composition of the Ti-6Al-4V ELI powder that is used and the mechanical property requirements of the printed components. The parts were printed with a slice distance of 60 μm and during printing the building chamber was kept under argon atmosphere ([O^2] < 0.5%).

2.2.1.3 META-IMPLANTS

Due to the meta-implant's complexity, data preparation and trials were essential. The .STL files were combined in RDesigner, after they had been transformed to the right printing configuration in Materialise 3-Matic (Figure 5c). After three trials, a successful print was obtained with the SLM125 SLM machine (Realizer GmbH, Borchen, Germany), using the aforementioned plasma-atomized, spherical Ti-6Al-4V ELI grade 23 powder (ASTM B348).

During fabrication, the building chamber was kept under argon atmosphere ([O^2] = 0.1-0.2%) and the mild steel building substrate was kept constant at 100 °C. The inner and outer structure were printed with a laser current of 1100 mA while exposure time and point distance were kept at 20 μs and 10 μm, respectively. The inner hatching was fabricated with a hatch distance of 0.15 mm and an xy-pattern. The laser current was set at 1100 mA, while exposure time and point distance were kept at 5 μs and 10 μm, respectively.

The RDesigner point generator was used to create the support structures, and just like the mechanical metamaterials, phantom designs were created to maintain the integrity of the specimens. The inner struts were removed from the porous region in Figure 3c-2, resulting in phantoms containing just the strut ends along the curved faces of the implants. The procedure in section 2.2.1.1 was repeated, which resulted in the support structure of Figure 5c. Given that earlier prints had failed due to an unstable base, the settings for the supports underneath the femoral head were adjusted. A current of 1200 mA was send to the laser, while exposure time and point distance were kept at 200 μs and 120 μm, respectively. The supports underneath the porous region and solid stem needed less strength and were therefore printed with a current of 1000 mA, an exposure time of 200 μs and a point distance of 120 μm.

2.2.2 POST-PRINTING TREATMENT

The excess powder was removed from the printed parts (Figure 4c), after which manual cutting procedures were used to remove the mechanical metamaterials and meta-implants from the build plate (Figure 4e). Electrical Discharge Machining (EDM) was used to remove the hybrid mechanical metamaterials from their build plate.

The high degree of porosity in the mechanical metamaterials made subsequent cleaning unnecessary. However, the 50% reduction in cell size made it more difficult to remove all loose metal particles from the hybrid mechanical metamaterials and meta-implants. Those specimens were therefore submerged in 96% ethanol and ultrasonically cleaned for 10 minutes, using a Branson 5510 ultrasonic cleaning bath (Branson, Danbury, USA).

2.3 MECHANICAL TESTING

Once the specimens were acquired, several test set-ups were created to assess their mechanical properties. The procedure that was followed to fulfil the experiments, has been described below.

2.3.1 AXIAL AND OFF-AXIAL COMPRESSION

The mechanical metamaterials were compressed in between two tool steel platens, with a constant deformation rate of 1 mm/min using a Zwick/Roell (Zwick GmbH & Co. KG, Ulm, Germany) static test machine (BZ1-MM14550.ZW02 with a 20 kN load cell) (Figure 6a). The specimens were loaded up till 10 mm deformation (±40% strain).

The hybrid mechanical metamaterials were off-axially compressed with a constant deformation rate of 1 mm/min using the same Zwick/Roell static test machine (Figure 6b). A maximum deformation of 2 mm was directed at the steel cylinder, using a tool steel rod, to create a bending moment around the structure. Initially, the bottom flange was added to prevent the side opposite to the deformation, from moving upwards. Unfortunately, the structure did come up during trials. 3M double-sided tape did not do the trick, but instead a clamp was used to apply a consistent load of 140 N.

One of the hybrid mechanical metamaterials was processed into a series of meta-implants. In order to proof the concept, the implanted configuration of the meta-implant had to be imitated. In real life, the uncemented meta-implant would be hammered into the medullary cavity of the femur, creating a tight fit between the implant's surface and the surrounding bone. Rigid foam blocks (model #: 1522-03, 20 PCF, $E_{compressive}$ = 210 MPa and $E_{tensile}$ = 284 MPa[43]) were therefore acquired from Sawbones (Sawbones Europe AB, Malmö, Sweden) to simulate the surrounding healthy bone. They were manually cut and filed to size, aligning with the medial and lateral sides of the meta-implant. An aluminum bottom plate was milled to accommodate the tip of the meta-implant, as well as two 6 mm acrylic plates. The acrylic plates closed off the "medullary cavity", while maintaining the implant's visibility during testing. Two stainless steel plates were laser cut and subsequently bended to form the side panels. In order to keep the acrylic plates in place, two shallow slits were milled. Holes were drilled to accommodate the necessary screws for optimal clamping of the meta-implant and the surrounding "bone". The hole at the bottom of the meta-implant was threaded, to enable its connection to the aluminum plate. Two threaded rods were used to tie the top of the side panels to one another with the help of a moment wrench (1 Nm) to ensure test repeatability. A belt sander was used to make the meta-implants fit in between the two acrylic plates. The complete set-up has been presented in Figure 6c and 7. A Zwick/Roell static test machine (BZ2-MM14450.ZW14 with a 10 kN load cell) was used to apply a maximum deformation of 1.5 mm. The same tool steel rod was used to locally apply this deformation to the femoral head (Figure 6c). This deformation is relatively small, but since each stem was tested twice, plastic deformations had to be prevented. For the same reason, the rate of deformation was reduced to 0.5 mm/min. The foam blocks were refreshed every single test.

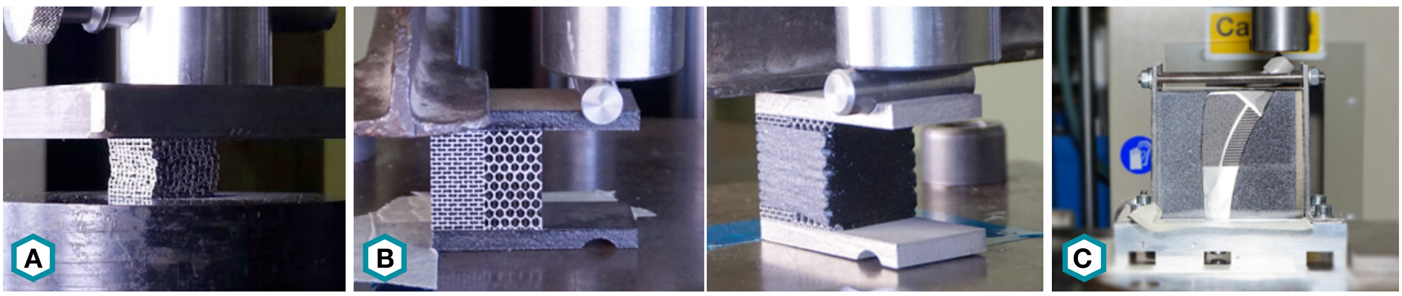

Figure 6: Compression testing. (A) Axial compression of mechanical metamaterials, (B) Off-axial compression of and hybrid mechanical metamaterials, (C) Off-axial compression of meta-implants.

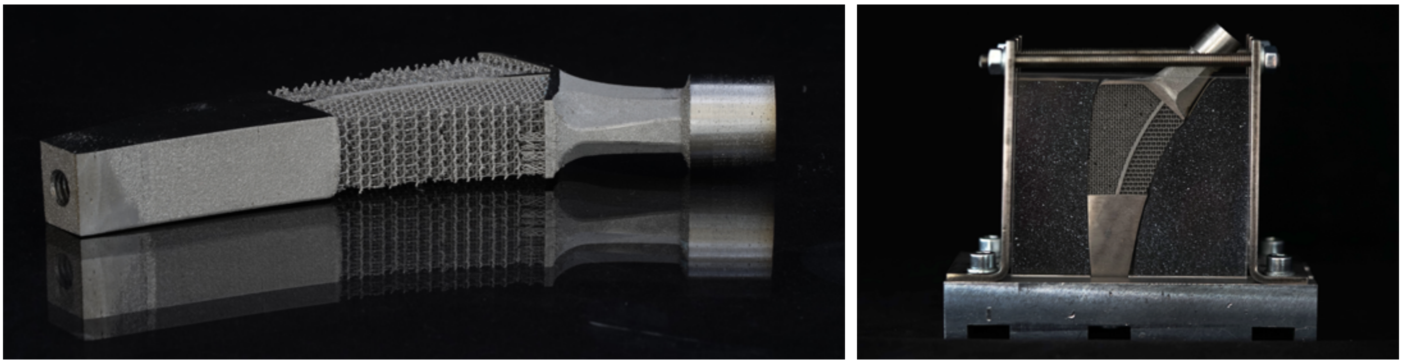

Figure 7: (left) Fully prepared meta-implant, (right) Experimental set-up including bottom plate, side panels, plexiglass plates, speckled foam blocks (section 2.3.2), thread rods and meta-implant.

2.3.2 DIGITAL IMAGE CORRELATION

Digital Image Correlation (DIC) is used to measure strain and displacement by comparing photographs of the specimen at different stages of deformation.[44] The technique has been proven effective in a number of fields, including aerospace, civil engineering and material science. In this project, it has been used to measure displacements within the specimens, as well as surface strains in the surrounding material.

For digital image correlation to work efficiently, the surface of the studied specimens should have sufficient image texture with a random and unique pixel pattern. Although a solid titanium specimen may have had this naturally, the highly porous specimens in this study needed some preparation.

In order to calibrate the DIC cameras, the front surface should stand out from the inner structure. For this to happen, the mechanical metamaterials were first colored with black spray paint. Subsequently, the front surface was stamped in white, after which an airbrush was used to add a black, random and unique speckle pattern (Figure 8). The Vic-3D 7 software (Correlated Solutions Inc., Irmo, USA) was used to verify the randomness of the speckle pattern, after which all specimens received the same treatment.

Four specimens of each hybrid mechanical metamaterial were prepared for an “open” examination of their deformation. Unfortunately, the aforementioned procedure appeared to be a bit more difficult to execute. Due to the smaller cell sizes the paint easily accumulated within the cells, closing off the pores. To prevent this from happening, an air compressor was used to blow out the excessive paint. Unfortunately, the compressor could not be used for the white paint, since the structures were too dense to be blown out from the back and blowing them from the front would result in the inner struts being colored. The front surface was therefore carefully painted using Tipp-Ex, and subsequently treated with the airbrush. The remaining hybrid specimens were prepared for a “closed” examination of the deformation (Figure 6b). A self-vulcanizing, highly stretchable tape was stretched around the structure to form a tight and continuous outer layer. This layer was later treated with the airbrush to add a white speckle pattern.

Unlike the previous tests, the meta-implants themselves were not prepared for DIC examination. Instead, the strain distributions in the surrounding “bone”, as a consequence of the meta-implant’s deformation, were of interest. The foam blocks were therefore sprayed in black and subsequently treated with an airbrush to add a white speckle pattern.

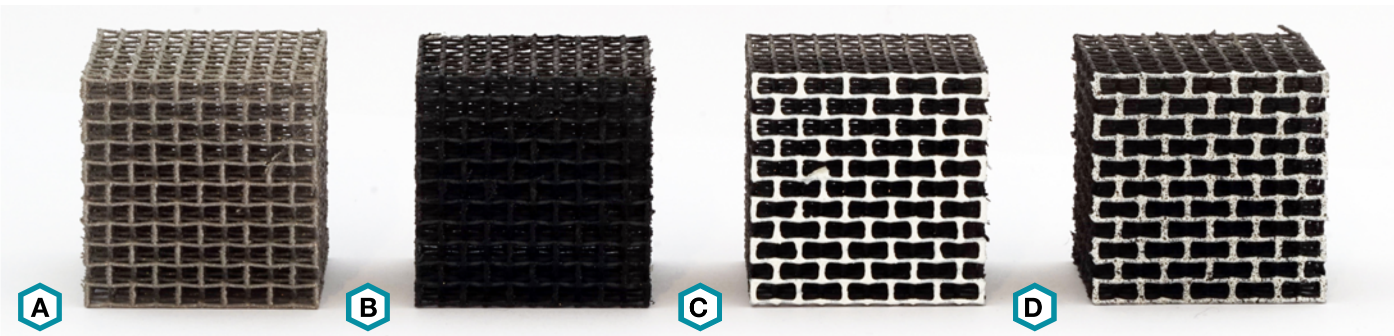

Figure 8: Mechanical metamaterials in each stage of the DIC preparation. (A) As manufactured, (B) Spray painted in black, (C) Front surface stamped in white, (D) Air-brushed with black.

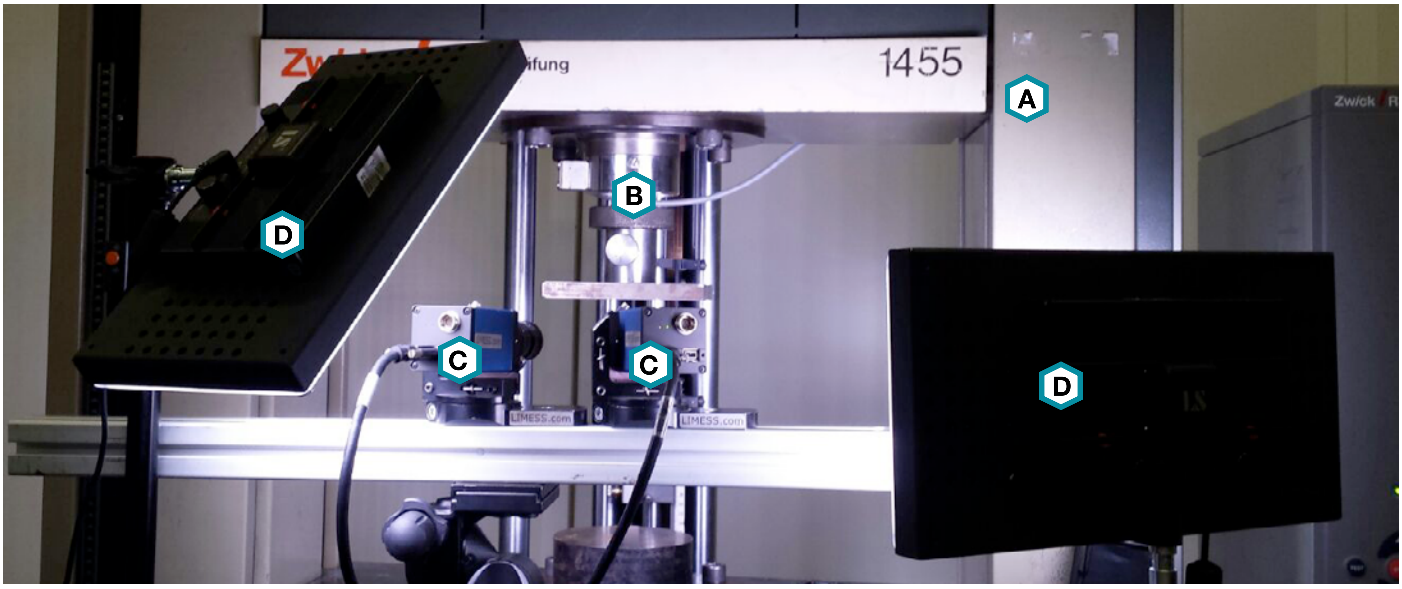

Figure 9: DIC set-up for compression testing of mechanical metamaterials and hybrid mechanical metamaterials. (A) Zwick/Roell static test machine, (B) 20 kN load cell, (C) Limess 4 Megapixel camera, (D) Lamp.

During mechanical testing, two 4 Megapixel digital cameras (Limess, Krefeld, Germany) were used to capture the sample surface with a frequency of 1 Hz (Figure 9c). Lights were used to enhance the contrast and clarify the images. Once the cameras were directed (about 30 degrees apart) to capture a sharp and complete surface, the DIC system was calibrated using the VicSnap software (Correlated Solutions Inc., Irmo, USA). Due to a difference in field of view, several calibration boards were used throughout the experiments. A 12 x 9-dots board, with a separation distance of 2 mm, was used to calibrate the system for the mechanical metamaterials. A 10 x 14-dots board (separation of 3 mm) was used for the hybrid mechanical metamaterials and a 10 x 14-dots board (separation of 5 mm) for the meta-implants.

An overview of the set-up has been presented in Figure 9. For the meta-implant experiments a different lamp was used, to prevent the plexiglass from reflecting the light. Pictures were taken using VicSnap, after which they were uploaded to the full-field, image analysis software Vic-3D 7 (Correlated Solutions Inc., Irmo, USA). Once the area of interest (Aoi) was defined, the software could calculate the displacements and strain fields.

2.3.3 IMAGE PROCESSING

To calculate the Poisson's ratio of the mechanical metamaterials, the DIC images needed to be processed. The vertices of eight centrally located unit cells were therefore marked with a red pixel using Adobe Photoshop CC (Figure 10a). The mechanical properties of each specimen were compared to the design group's mean, and the closest match was chosen as a representative. A selection of pictures was taken from those recorded during the elastic deformation. Subsequently, about 20 images (one image every five seconds) were marked with red pixels for each representative specimen.

The images of the hybrid mechanical metamaterials were processed in Vic-3D. The post-processing module included the possibility of assigning data points and retrieving one's deformation. Thirty points were manually plotted along the right and left borders of the specimens, as well as along the middle (Figure 10b). Points in the same column were plotted at approximately the same x-coordinate. The corresponding information could then be exported to an Excel file.

The images gathered during the "closed" examination of the hybrid mechanical metamaterials were only processed visually. The minimum and maximum horizontal strain (ε_{xx}) values were found for each specimen, after which each of them was plotted along the same limits. The same procedure was repeated for the images of the meta-implants. Additionally, the latter were plotted in two colors (Vic-3D's Tropical sea filter) to emphasize the difference between positive and negative strain values.

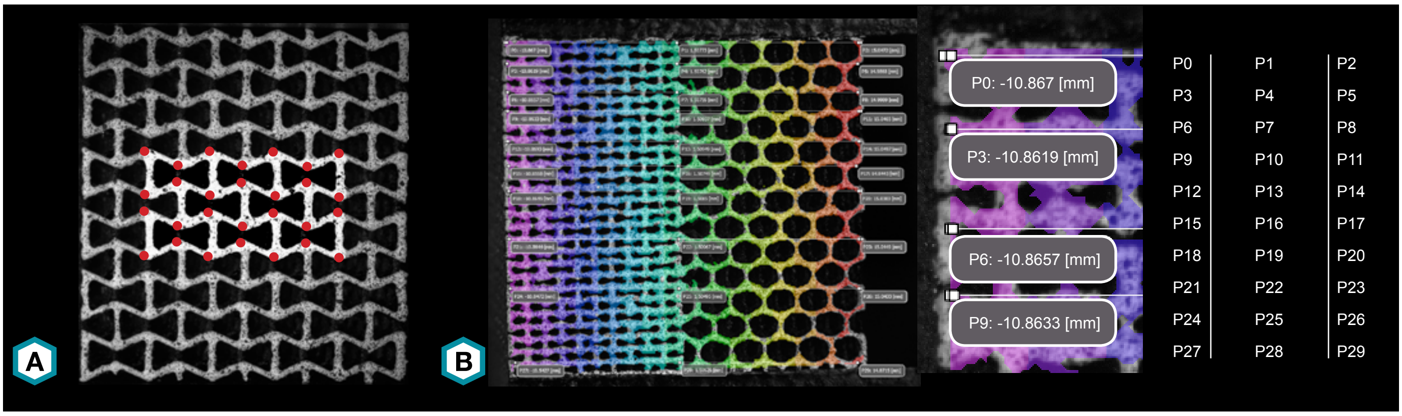

Figure 10: Image processing methods. (A) Selection of eight centrally located unit cells with red markers in an auxetic mechanical metamaterial. (B) Position of the plotted points on an image of a hybrid mechanical metamaterial, a magnified view and the order in which the data points have been allocated.

2.3.4 DATA ANALYSES

The mechanical metamaterials were axially compressed and with the load-displacement curves from the compression machine's testXpert II software (Zwick GmbH & Co. KG, Ulm, Germany) the stress-strain curves could be easily determined. Based on these curves and the corresponding data points, the Young's modulus, ultimate compressive strength and yield strain could be derived.

The stress could be obtained by dividing the applied load by the lattice structure's original area. The corresponding strain was calculated by dividing the displacement by the original height of the lattice structure. Matching pairs of stress and strain were plotted in Excel to obtain the stress-strain curve.

The Young's modulus for compression could be obtained using the slope of the stress- strain curve in the first linear elastic region. Data points 200 and 1100 were found to enclose a representative portion of the elastic region, and were therefore used to calculate the differences in stress and strain. Subsequently, the tangent was obtained by dividing the difference in stress by the difference in strain.

The first peak in the stress-strain graph was regarded as the ultimate compressive strength (UCS). Following the continuous increase of stress values, the first continuous drop would mark the value corresponding to the ultimate compressive strength. The corresponding strain value was regarded as the Yield strain.

A Matlab code was written to track the red dots plotted in the DIC images (Figure 10a). The coordinates of these dots were determined at different stages of deformation, after which ε_{xx}, ε_{yy} and the Poisson's ratio $v = - \varepsilon_{xx} / \varepsilon_{yy}$ could be calculated.

With the specimen volume, weight and density (0.00443 g/mm^3) of Ti-6Al-4V known, the relative density could be calculated by dividing the density of the specimen by the density of a solid titanium block with the same volume. The density of the specimen was calculated by dividing the weight by the volume.

The Excel file, exported from Vic-3D, included the initial coordinates of the hybrid mechanical metamaterial's data points as well as their deformation. The maximum expansion in the x-direction (negative for the auxetic side and positive for the conventional side) was plotted for each data point using Excel. The sum of the deformations (ux and uy) and the initial coordinates (x, y) resulted in the new positions of the data points in time. All data points within the same column were plotted in Matlab to form borderlines.

The strain distributions found on the "closed" hybrid specimens, as well as on the "bone" surrounding the meta-implants, were visually compared to one another.

2.4 FINITE ELEMENT MODELLING (FEM)

The computational power needed to run a three-dimensional (3D) simulation of the hybrid mechanical metamaterials appeared to be too extensive for the resources at hand. Instead, a two-dimensional (2D) model was created to quickly assess the differences between a hybrid mechanical metamaterial and the corresponding auxetic and conventional mechanical metamaterials in a bending situation.

A front slice was cut from the 3D designs in Solidworks, which were then saved as .DXF files. These sketches were imported into Abaqus/CAE (Dassault Systemes, Vélizy-Villacoublay, France) to form new 2D planar, deformable parts. These parts were meshed using a 0.25 seed (to make sure at least two elements are created across one strut) and CPE6H elements.

MATERIAL

Since the material properties of 3D-printed Ti-6Al-4V are different from solid casted Ti-6Al-4V, six 3D-printed titanium cylinders were compressed to obtain their compressive Young's moduli. These titanium cylinders measured 20 mm in length and were given a diameter of 10 mm (ratio of 2:1). The slope in the elastic region of their stress-strain curve was calculated, which resulted in an average Young's modulus of 11.49 GPa.

The Poisson's ratio of 0.33 was found in literature[45], and together with the Modulus they were filed as the elastic, isotropic properties of the material. The plastic properties were not provided, since these deformations should be prevented.

SECTION PROPERTIES

For each model a homogeneous solid section was created, linked to the above-mentioned material properties. A plane strain thickness of 25 mm was assigned, matching the depth of the real specimens. Once the section properties were appointed to the complete geometry, the model could be assembled and an analysis step could be created.

LOADS AND BOUNDARY CONDITIONS

To imitate the real-time off-axial compression tests, the specimens had to be clamped at the bottom (Figure 11c, which was tied to reference point 2), loaded at the upper left corner (Figure 11b, as a consequence of the clamp) and compressed in reference point 1. The total deformation of 2.5 mm matches the 2-mm compression in the real test, assuming the flange does not bend and the load is applied 10 mm from this reference point (Figure 11d).

A second situation was introduced without the load at c being present. This would more closely resemble the situation in which the hybrid mechanical metamaterial will be allowed to deform once it is implemented in the meta-implant.

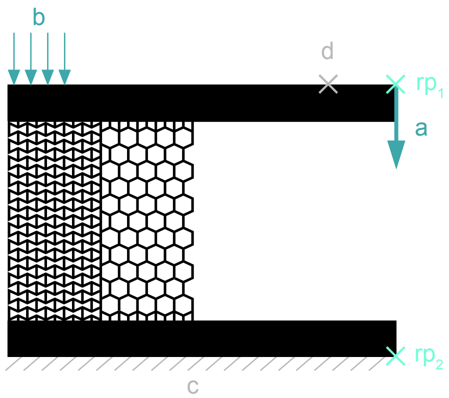

		a (mm)	b (N)	c (mm)
Situation 1	x	0	0	0
	y	-2.5	-140	0
	z	0	0	0
Situation 2	x	0	0	0
	y	-2.5	0	0
	z	0	0	0

Figure 11: Finite element model with boundary conditions and loads. Table shows the values applied in situation 1 and 2.

2.5 STATISTICAL ANALYSES

The data has been statistically analyzed using the commercially available SPSS Statistics software (IBM, Armonk, USA). The normality of the data was assessed using the normality plots and the numerical measures Skewness and Kurtosis.

In case the data was normally distributed, one-way independent ANOVA tests were performed to see whether there are significant differences between the design types. Once the assumption of homogeneity of variance was met (Levene's test), a Tukey post-hoc test was performed to show which specific groups differed. A Games-Howell post-hoc test was done in case the assumption was not met.

In case the data was non-normally distributed, the rank-based nonparametric Kruskal-Wallis test was performed. In this case, the homogeneity of variances' test was performed on the absolute difference between the individual ranks and the mean ranks of their group. If this assumption is not met, the Kruskal-Wallis test can only be used to compare mean ranks.[46,47]

The data has been presented as the mean and has been reported as recommended in Discovering Statistics using SPSS by Andy Field[46], considering a significant difference when $p<0.05$. Plots were made in Excel and were subsequently edited in Adobe Indesign CC.

3. RESULTS

3.1 MECHANICAL METAMATERIALS

The stress-strain curves of the compressive tests for the different mechanical metamaterials have been presented in Figure 12. All curves exhibit a periodic pattern, consistent with the failure of entire layers within the structure. The auxetic mechanical metamaterials show relatively small stress drops compared to those found for the conventional mechanical metamaterials. The latter dropping to near zero values, after which they increase to form a new peak. The highest pre-fracture peaks were found for the auxetic mechanical metamaterials.

Stress-strain curves for each individual specimen can be found in Appendix 8.1, together with the mechanical properties. The following mechanical properties have been visually presented in Figure 13.

Data on the compressive Young's moduli of the mechanical metamaterials were normally distributed with a Skewness of 0.73 (SE = 0.47) and Kurtosis of 0.28 (SE = 0.92). The assumption of homogeneity of variances was violated, $F(5,18) = 3.83$, $p<0.05$, which is why a One-way ANOVA was executed using a Games Howell post hoc test. The Type of design was found to significantly affect the Modulus of the structure, $F(5,18) = 53.57$, $p < 0.05$, $\omega = 0.96$. ω is a measure of effect size and in this case shows that the observed effect is large.

With a mean Modulus of 52.19 MPa, C2 was found to significantly differ from all other design types ($p < 0.05$). In contrast, A2 and C3 were found insignificantly different from all other design types ($p > 0.05$), except from C2. A1 was found to have the lowest Modulus, being significantly different from A3, C1 and C2. For the auxetic mechanical metamaterials the Modulus increased with re-entrant angle, whereas the Modulus of conventional mechanical metamaterials increased with internal angle.

The data on the ultimate compressive strength was normally distributed with a Skewness of 0.05 (SE = 0.47) and a Kurtosis of -0.93 (SE = 0.92). The variances were equal, $F(5,18) = 1.11$, $p > 0.05$, which is why a One-way ANOVA was executed using a Tukey post hoc test. The type of design was found to significantly affect the ultimate compressive strength, $F(5,18) = 35.34$, $p < 0.05$, $\omega = 0.93$. This shows that the variance in ultimate compressive strength is again largely accounted for by the design type.

The highest UCSs were found for the auxetic mechanical metamaterials, with A1 (M = 2.36) and A3 (M = 2.44) being significantly different from the other designs ($p < 0.05$). Again, the strength increased with re-entrant angle for the auxetic mechanical metamaterials. Among the conventional mechanical metamaterials C1 (M = 1.97) and C2 (M = 2.16) were found significantly different.

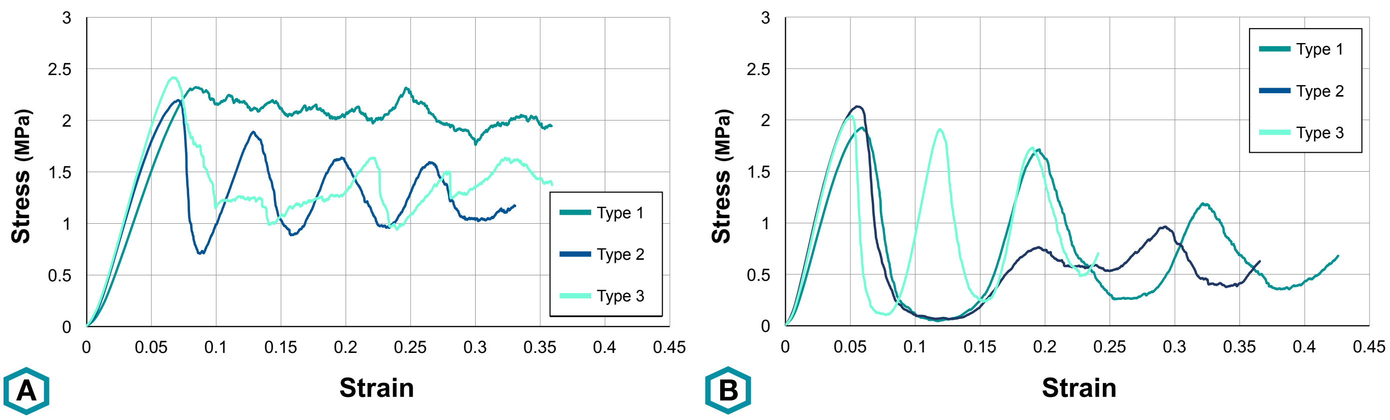

Figure 12: Mean stress-strain curves of (A) auxetic and (B) conventional mechanical metamaterials under compression.

The corresponding yield strain data was normally distributed with a Skewness of 0.76 (SE = 0.47) and a Kurtosis of 1.13 (SE = 0.92). The variances were equal, $F(5,18) = 1.97$, $p > 0.05$, which is why a One-way ANOVA was executed using a Tukey post hoc test. The type of design was found to significantly affect the yield strain value of the structure, $F(5,18) = 15.12$, $p < 0.05$, $\omega = 0.86$. There is again a large effect, which shows that the yield strain is also strongly affected by the design type.

With a yield strain of 8.29%, A1 was found to be significantly different from all other design types ($p < 0.05$). In contrast to the previous properties, not relation could be observed between the auxetic mechanical metamaterials. The yield strain of the conventional mechanical metamaterials does decrease with internal angle.

During compression, the auxetic mechanical metamaterials showed a lateral shrinkage (Figure 8a), thanks to their negative Poisson's ratio. The conventional designs, on the other hand, showed a lateral expansion.

The image processing appeared to be very time-consuming, which is why only the data of one representative specimen was used to obtain the Poisson's ratio of the design type. Since this led to a dataset with zero variance, SPSS was not able to correctly compare the means. Excel was therefore used to create random numbers for each design, with a normal distribution, a standard deviation of 0.05 and a group mean corresponding to the value found for the representative design, as presented in Figure 13 (v).

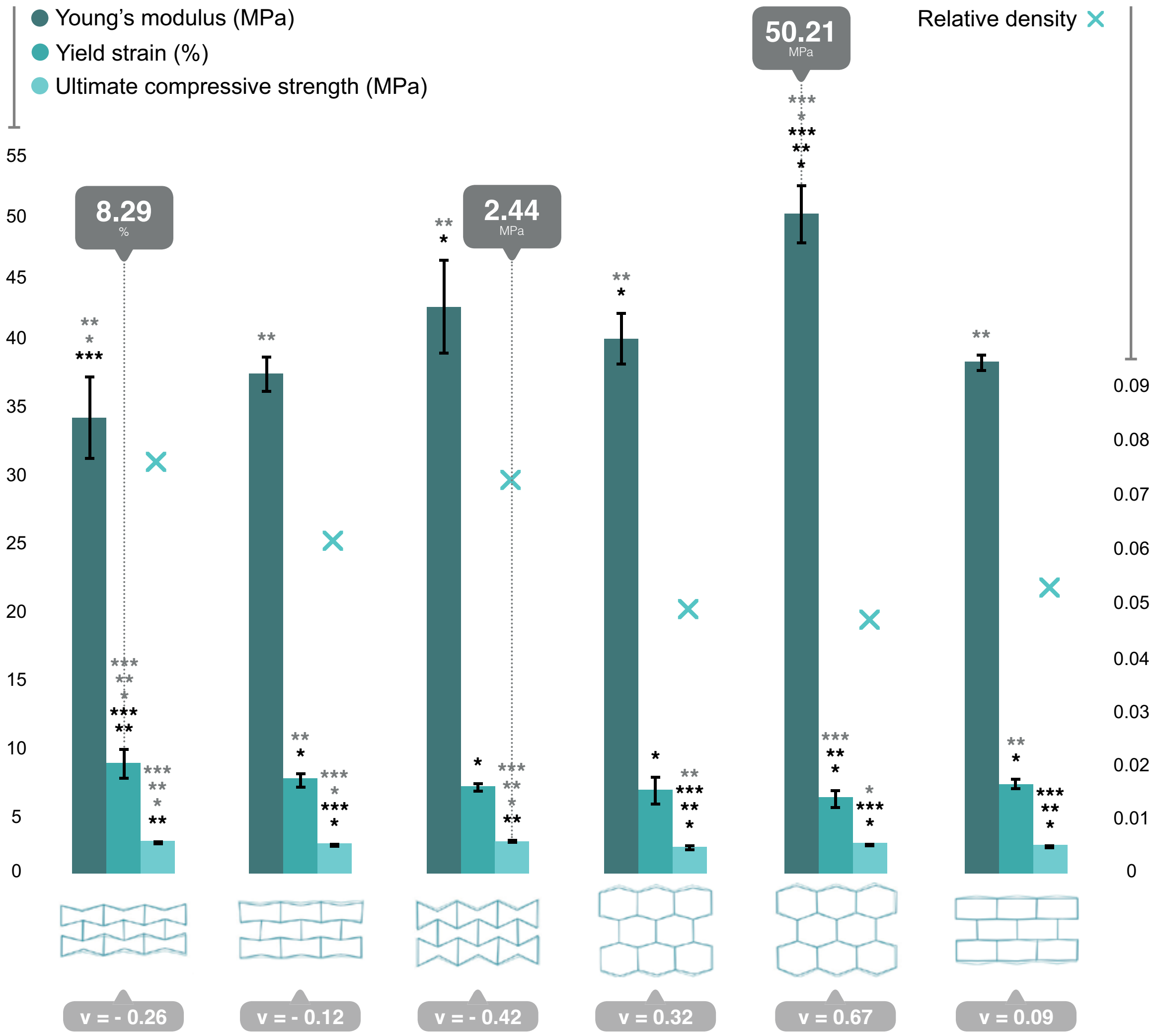

Figure 13: Mean compressive Young's modulus, yield strain, ultimate compressive strength, relative density and Poisson's ratio of (FLTR) Auxetic Type 1 (A1), " Type 2 (A2), " Type 3 (A3), Conventional Type 1 (C1), " Type 2 (C2), " Type 3 (C3). Data is expressed as mean and error bars indicate 95% confidence bounds. Significant differences are indicated by *p < 0.05 compared with A1, **p < 0.05 compared with A2, ***p < 0.05 compared with A3, *p < 0.05 compared with C1, **p < 0.05 compared with C2, ***p < 0.05 compared with C3 by One-way ANOVA.

The randomized dataset was indeed normally distributed with a Skewness of 0.365 (SE = 0.472) and a Kurtosis of -1.049 (SE = 0.918). The variances were equal, $F(5,18) = 0.556$, $p > 0.05$, which was expected with a constant standard deviation. The one-way ANOVA showed that the type of design significantly affects the Poisson's ratio, $F(5,18) = 339.12$, $p < 0.05$, $\omega = 0.99$. The observed effect is large, but this might be biased by the simulated nature of the data.

The NPR of the auxetic mechanical metamaterials increased with re-entrant angle, whereas the positive Poisson's ratio of conventional mechanical metamaterials increased with internal angle. All designs were found to be significantly different form one another ($p < 0.05$). The highest absolute Poisson's ratio (0.67) was found for the conventional mechanical metamaterial Type 2. The deformation of each representative sample has been processed into a short movie, which can be found in the .PDF version of Appendix 8.1

The mean relative density has been plotted in Figure 13.

3.2 HYBRID MECHANICAL METAMATERIALS

The behavior of the hybrid mechanical metamaterials, subjected to off-axial compression was evaluated. The expansion was quantified using an "open" specimen, whereas the resulting strains in a surrounding material were evaluated using a "closed" specimen. A 2D finite element model was made of the hybrid showing the most effective expansion, to be compared with the corresponding mechanical metamaterials.

3.2.1 EXPANSION

The coordinates and deformations of thirty data points were exported from Vic-3D and manually processed in Excel. The mean maximum expansion was calculated for each hybrid, and plotted in the bar graph of Figure 14. The maximum expansion on the auxetic side was located at the bottom of the specimens, whereas the biggest expansion of the conventional side was found at the top. The expansion for each individual specimen has been plotted in Appendix 8.2. The auxetic side will now be referred to as the lateral side, while the conventional side will be referred to as the medial side of the specimens.

For hybrid Types 1, 2, 4 and 5 the maximum expansion on the medial side was more than five time as large as the maximum expansion on the lateral side. For hybrid Type 3 this was only four times, whereas the maximum expansion on the medial side of hybrid Type 6 was only 1.5 times bigger than the one observed on the lateral side. The expansion on the lateral side happened along the complete height of the specimens, whereas the bottom of the medial side did not expand at all.

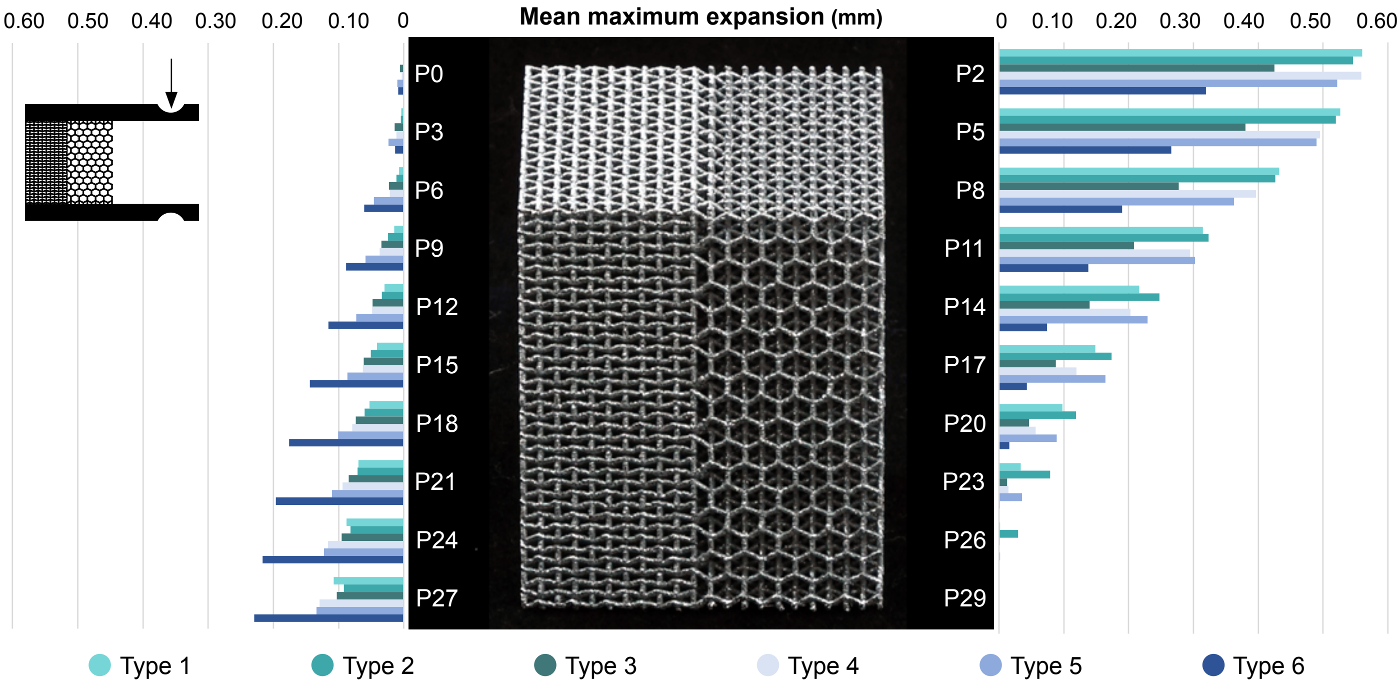

Figure 14: Mean maximum expansion of hybrid mechanical metamaterials during off-axial compression.

The expansion on the lateral side increased with design type, except for data points 24 and 27, and the absence of a transitional region seems to enhance this effect. In contrast, the expansion on the medial side decreased with design type for the top three data points. Thereafter, hybrids Type 2 and 4 (85-degree re-entrant cells) showed a bigger expansion than their 75-degree counterparts, Types 1 and 3 respectively. Here, the presence of a transitional region enhanced the expansion.

Most of the data was non-normally distributed and violated the assumption of homogeneous variances. Their mean ranks were therefore analyzed using the nonparametric Kruskal-Wallis test. A One-way ANOVA and an appropriate post-hoc test were carried out for the normally distributed data. The type of design was shown to significantly ($p < 0.05$) affect the expansion in data points P2 ($H(5) = 17.09$), P5 ($H(5) = 15.53$), P6 ($H(5) = 11.81$), P8 ($H(5) = 18.22$), P11 ($F(5,18) = 5.55$), P14 ($F(5,18) = 6.70$), P17 ($F(5,18) = 5.07$), P20 ($F(5,18) = 3.35$), P23 ($H(5) = 13.68$) and P26 ($H(5) = 14.36$). The differences primarily lie between hybrid Type 6 and the other design types, which can also be observed in Figure 14.

The initial coordinates and deformations were used to obtain the coordinates of the data points in time. Those located in the same column were plotted in Matlab to form borderlines (Figure 15). The expansion along the lateral side was found to travel from top to bottom with increasing compression, but once it had reached its maximum value, it started to retract (move into the positive x-direction). The expansions along the medial side were found to increase with the degree of compression, except for P29 (and P26 in some cases). The latter were shown to retract (move in negative x-direction) from t = 0 onwards.

The mean coordinates were plotted for each design type, every 15 seconds from t = 15 till t = 120 s. The resulting sequence of images was made into a short movie, which can be found in the .PDF version of Appendix 8.2.

3.2.2 FULL-FIELD STRAIN DISTRIBUTION

Just like the “open” hybrid mechanical metamaterials, the “closed” specimens were subjected to off-axial compression. For each design, the most representative results have been plotted in Figure 16. The results of each individual specimen can be found in Appendix 8.3.

Each hybrid design type showed an obvious compression on the medial side of the structure, especially hybrid Types 2 and 5. The lateral sides of hybrid Types 1, 2, 4, and 5 were almost entirely covered in negative strains. In contrast, the negative strains found in Hybrid Types 3 and 6 were almost completely limited to the central area. The biggest lateral regions with positive strain were found in hybrid Types 3 and 6, with an almost continuous profile along the border of hybrid Type 6.

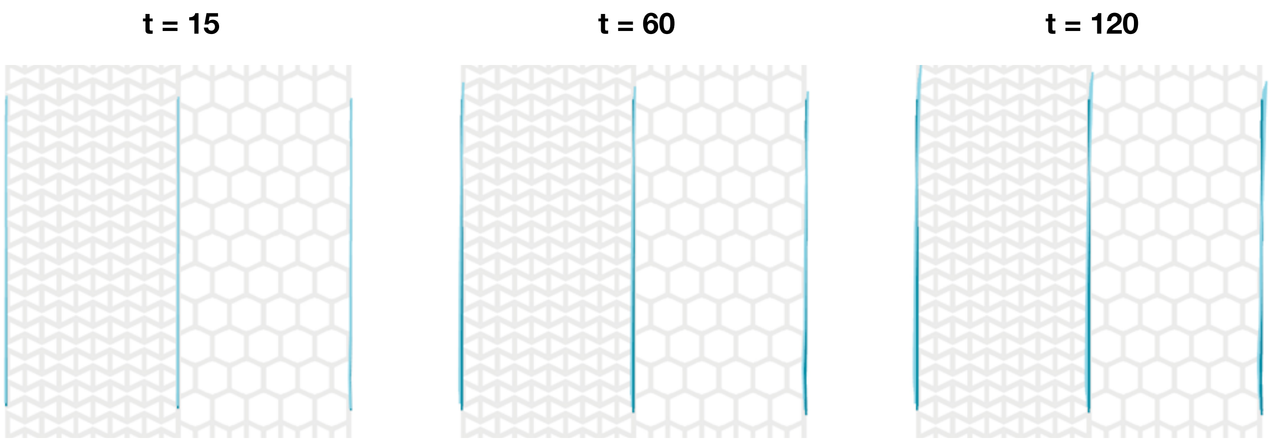

Figure 15: Mean deformation of hybrid mechanical metamaterial Type 6 at t = 15 s, t = 60 s and t = 120 s. The dark line resembles the initial position of the borderlines, whereas the current position has been depicted in light blue/green.

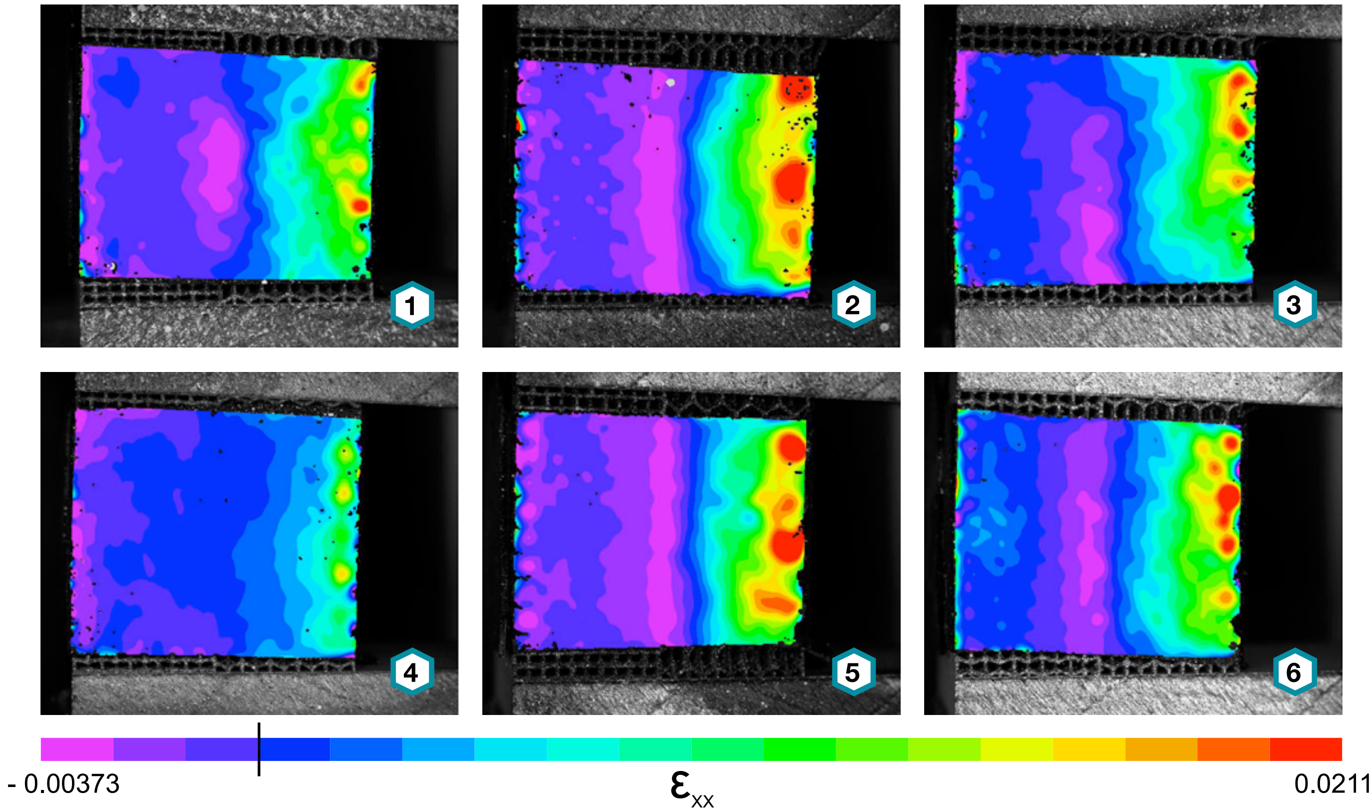

Figure 16: Horizontal strains in the self vulcanizing tape surrounding (1) Hybrid Type 1, (2) Hybrid Type 2, (3) Hybrid Type 3, (4) Hyrid Type 4, (5) Hybrid Type 5 and (6) Hybrid Type 6.

3.2.3 FINITE ELEMENT MODELLING

The results of the finite element modelling have been presented in Figure 17, for loading situation 1 and 2. All structures showed a medial expansion in both situations, but to a different extent. The absence of the load in situation 2 enhanced the effects seen in B1 and C1. However, the medial shrinkage observed at the bottom of the auxetic mechanical metamaterial in A1, was less apparent in A2. The auxetic effect on the lateral side, however, was more apparent in A2 compared to A1. Here, the bottom showed a small expansion, and the retraction progresses more gradually towards the top.

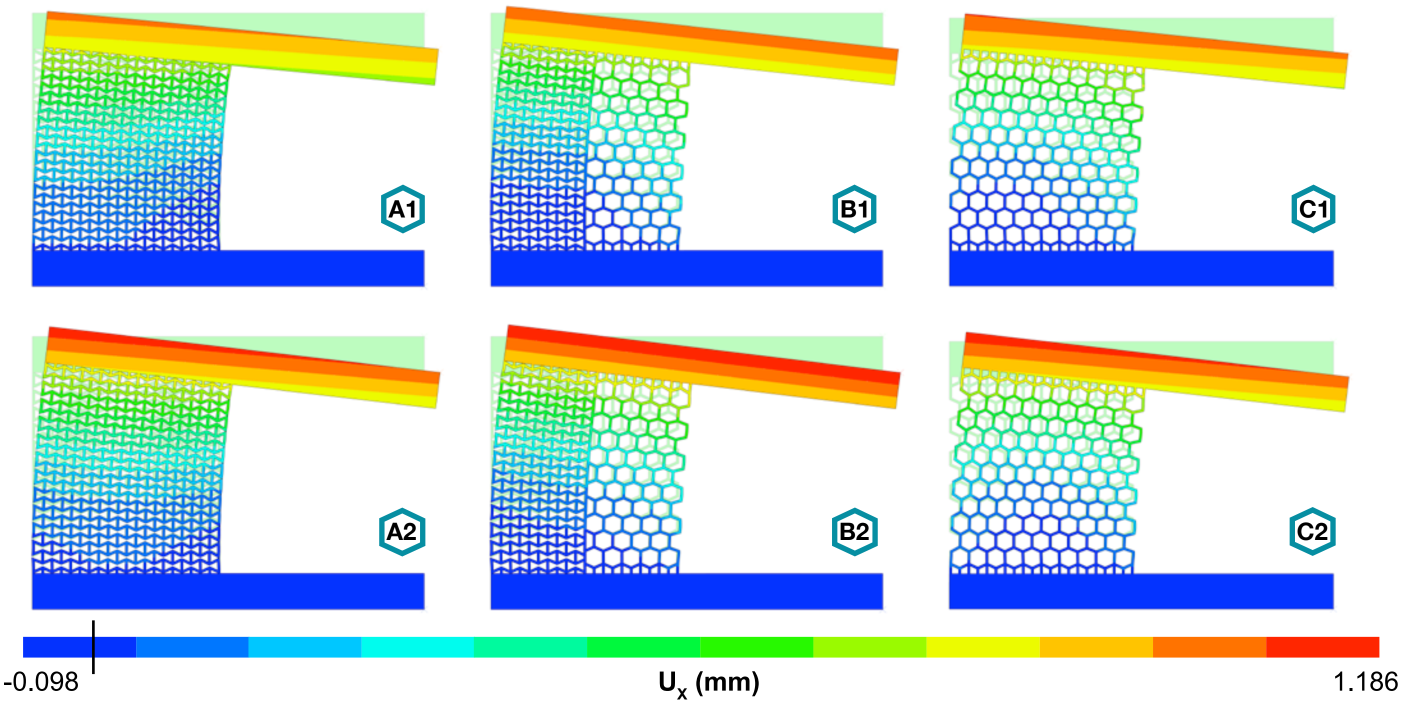

Figure 17: Simulated horizontal displacements of an (A) Auxetic mechanical metamaterial, (B) Hybrid mechanical metamaterial Type 6 and a (C) Conventional mechanical metamaterial in (top) situation 1 and (bottom) situation 2. Visualized with a deformation scale factor of 2.

The conventional mechanical metamaterial showed a medial expansion in both situations. The lateral side primarily retracted. The hybrid mechanical metamaterial Type 6 showed a bilateral expansion in both situations. Removal of the load decreased medial expansion, whereas the lateral expansion increased.

3.3 META-IMPLANTS

Clamped in between two bone-like foam blocks, a load was applied at the femoral head of the meta-implants. For each design one representative specimen was chosen to visualize the effects. The resulting horizontal strains have been presented in Figure 18. The results of each individual design can be found in Appendix 8.4.

3.3.1 STRAIN DISTRIBUTION

The horizontal strains, or compression as a result of the implant's deformation, were visualized using Vic-3D's Tropical sea filter. A two-color scheme was chosen to show a clear contrast between positive and negative strain values. The individual specimen's limits were determined and the overall average was finally implemented in the plots of Figure 18. Although the zero-strain value is not marked by the border between the two colors, this division did show the most distinct effects. It now represents a horizontal strain value of 0.00125, which means all areas depicted in light blue experience an unmistakable compressive strain.

All meta-implants initiated compressive strains on the medial side, but the biggest differences were found on the lateral side of the meta-implants. Compared to the controls, the hybrid meta-implants initiated more compression on the lateral side. Hybrid meta-implant Type 2 even shows a continuous compression along the lateral border, while the other hybrid designs showed a more dispersed compression profile.

For each representative specimen, a short movie has been made, showing the changes in strain distribution over time. They can be found in the .PDF version of Appendix 8.4.

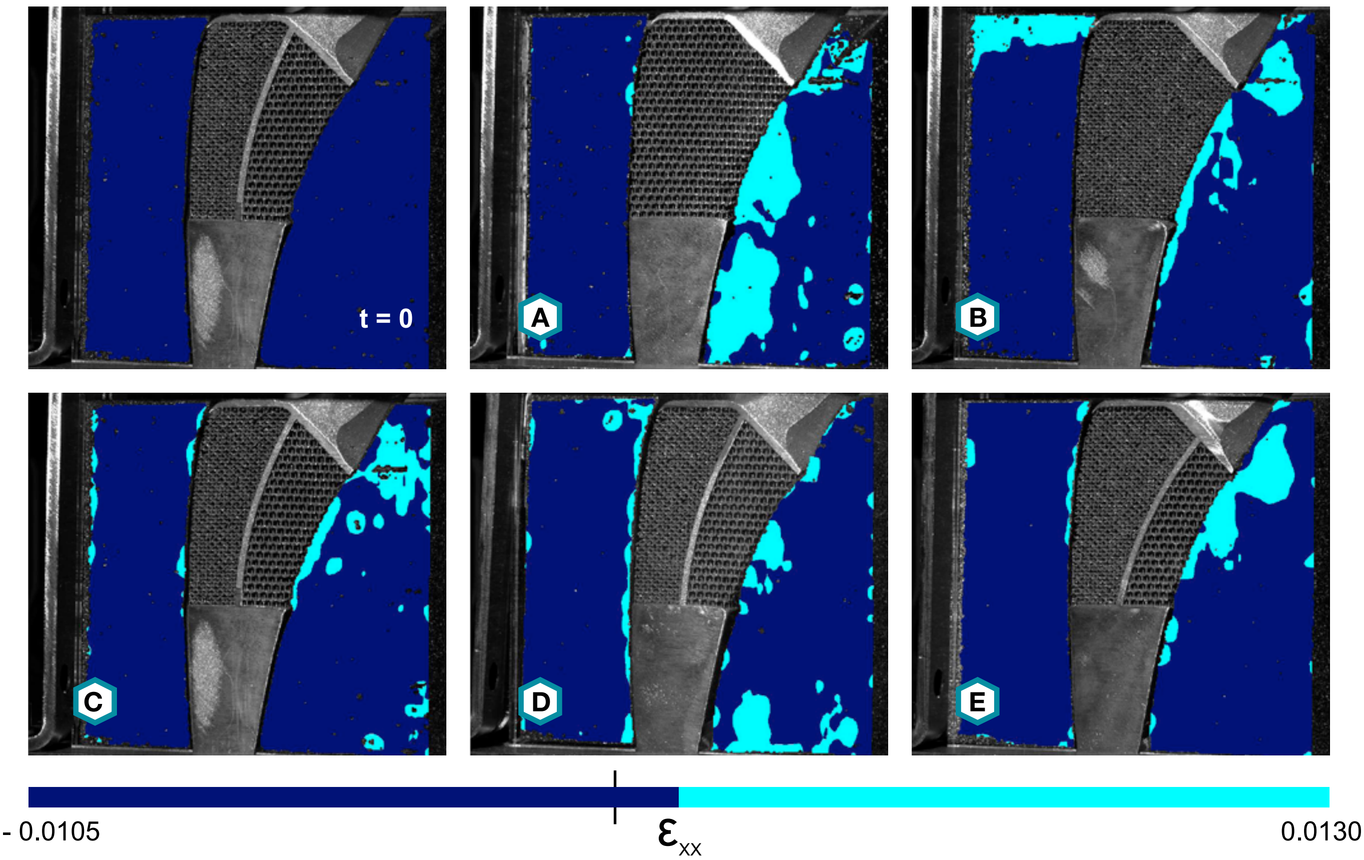

Figure 18: Horizontal strains in the "bone" surrounding the meta-implants at t = 0 s in the upper left corner and at t = 180 s for (A) Control Type 1, (B) Control Type 2, (C) Hybrid Type 1, (D) Hybrid Type 2 and (E) Hybrid Type 3.

4. DISCUSSION

The aim of this study was to design and assess the mechanical properties of auxetic and conventional mechanical metamaterials, analyze the behavior of hybrid mechanical metamaterials in bending situations and examine their effectiveness in an orthopedic meta-implant. Designs were made for each of these subprojects, and subsequently produced using SLM. All of the specimens were manually cleaned and prepared for DIC examination. While the mechanical metamaterials were axially compressed, the hybrid mechanical metamaterials were off-axially loaded to mimic their potential application in femoral stems. Finally, they were implemented in the design of an orthopedic meta-implant. An experimental set-up was designed to simulate the implanted configuration of the meta-implants, in which the structure is automatically loaded off-axially as a result of the contact between the femoral head and the acetabular cup. The following paragraphs will thoroughly discuss the results of the subprojects, the challenges and limitations that had to be overcome, the potential applications of the studied metamaterials and the future work needed to verify the presented concepts.

4.1 MECHANICAL METAMATERIALS

The stress-strain curves of the mechanical metamaterials show a periodic pattern, and this can be explained by the collapse of entire layers within the structure. The stereotypic regimes observed in the stress-strain curve of regular cellular solids contain an elastic stage, followed by a plateau stage and a final densification stage.[48] The stress-strain curves of these materials are therefore not typical, but Yang *et al.* (2012) explain that 3D periodic structures like these initially deform elastically, but start to fail when the yield strength of the critical strut is reached. Once this happens, the stress will be redistributed among the remaining struts in the same layer. This will result in the failure of the next critical struts, followed by the collapse of the entire layer.[49]

The structure most resistant to compression appeared to be C2, with a significantly higher Modulus than all other design types. Followed by A3, C1, C3 and A2 respectively, which are all insignificantly different from one another. A1 was found to be the least stiff, but not significantly weaker than A2 and C3. At first glance, one may argue that the overall differences in stiffness between the auxetic and conventional mechanical metamaterials are insignificant. However, the conventional mechanical metamaterials have a higher stiffness to weight ratio. This explains the use of honeycomb structures in applications requiring high stiffness at minimal weight. Furthermore, the stiffness of the conventional mechanical metamaterials was shown to increase with internal angle, which is probably a direct consequence of the orientation of the struts relative to the direction of the load. Since conventional honeycombs initially deform through bending[48], an increase in internal angle will reduce the moment arm and thus the bending moment around the diagonal struts. A particular deformation will therefore require a bigger load, directly increasing the slope of the stress-strain curve. According to literature, the stiffness of 3D re-entrant structures increases once the re-entrant angle increases.[23,37,49] This statement applies to A3, but the results found for A2 and A1, although not significantly different, do not seem to agree. The high variability among the specimens of A1 may be the reason of this discrepancy, affecting the reliability of the mean. Further research should confirm whether this variability has been caused by confounding variables, such as the production process.

The UCSs were obtained from the stress-strain curves, matching the stress value at which the first layer within the structures failed. This time, the UCSs of the auxetic mechanical metamaterials showed significantly higher values compared to the conventional mechanical metamaterials, with the exception of A2 compared to C2. Furthermore, the positive relation between the strength and the re-entrant angle was confirmed in this study.[49] The UCS results of the conventional mechanical metamaterials more closely resemble a negative relation between the strength and the internal angle. The strengths found for C1 and C3 seem to compromise this idea, although their difference is highly insignificant ($p=0.445$). This again suggests that the ranking order may have been interchanged due to the relatively high variability among the specimens of C1.

No design-based relation could be observed in the data on the yield strain. However, the ranking order, from high to low, did match the reversed version of the order found for the Moduli. This directly relates to the slope of the stress-strain curve, which increases in magnitude when strain values are low.

The Poisson's ratios found for the auxetic mechanical metamaterials exactly match the values found in literature.[37] In these structures (*a*/*b*=1.0-1.5) the maximum Poisson's ratio should be reached with a re-entrant angle of about 30 degrees. The Poisson's ratio did show to increase with re-entrant angle, although the 30-degree mark was not reached. These results show that an NPR can definitely co-exist with a high stiffness, as mentioned in other studies on auxetic three-dimensional structures.[49-51] The Poisson's ratio of the conventional mechanical metamaterials was shown to increase with the internal angle. This is a direct consequence of the length of the diagonal struts, which were designed to increase with the internal angle. Bending of the diagonal struts will push aside the vertical struts, resulting in a bilateral expansion. The ratio of transverse strain to that of axial strain, better known as the Poisson's ratio, will therefore become positive. The randomized nature of the dataset, and especially the very small standard deviation, resulted in a very large F-score. Such high F-scores usually do not occur in experimental datasets, as they indicate an extraordinary large significance. This would normally ask for a reevaluation, but since this dataset was simply made to obtain a general understanding of the differences, the magnitude of the F-score is not of interest.

Based on the abovementioned results, combinations of auxetic and conventional mechanical metamaterials can be made to obtain a material with a uniform stiffness, a consistent UCS, a matching yield strain and maybe even a bilateral expansion upon bending. The following table will present promising combinations of auxetic and conventional mechanical metamaterials, based on one chosen requirement.

Table 3: Potential combinations of auxetic and conventional mechanical metamaterials for specific requirements

Requirement					**Requirement**				
		C1	**C2**	**C3**			**C1**	**C2**	**C3**
Uniform stiffness	**A1**			✓	Matching Yield strain	**A1**			
	A2	✓		✓		**A2**	✓		✓
	A3	✓		✓		**A3**	✓	✓	✓
Consistent UCS	**A1**				Poisson's ratio (approximate opposites)	**A1**	✓		
	A2		✓			**A2**			✓
	A3					**A3**			

Unfortunately, none of the combinations seems to be valid for all of the requirements. The combination R2/C3 is valid for three of the requirements, which is not surprising given that their geometries are only 10 degrees apart. They were obtained using a standard deviation of five degrees from a 90-degree angle, and this is reflected in their relatively low absolute Poisson's ratio.

4.2 HYBRID MECHANICAL METAMATERIALS

Three different combinations of mechanical metamaterials were made, and for each combination two designs were generated to examine the influence of a transitional region when subjected to bending. An assessment was made of the specimens' expansion, and the strain distribution in the surrounding material as a result of this deformation.

Each of the hybrid design types showed a bilateral expansion, but all to a different extent. Despite being largely insignificant, the differences will be discussed in the following paragraphs. The biggest lateral expansion was expected in hybrid Types 3 and 6, for their high NPR, with respect to their equivalents. Hybrid Type 3 was indeed showing a bigger expansion than Types 1 and 2, and hybrid Type 6 showed a bigger expansion than Types 4 and 5. Despite their lower NPR, hybrid Types 4 and 5 showed a slightly bigger lateral expansion than hybrid Type 3. The transitional region thereby shows to have an effect on the deformation of the structure as a whole. This can also be observed on the medial side of the structures, where hybrid Types

1, 2 and 3 exhibit as much as a 100% higher expansion compared to their counterparts, Types 4, 5 and 6, respectively. The transitional cells seem to give the structure more freedom to translate, which corresponds to a reduction in bending stiffness. Whereas this might be in favor of the medial expansion, the deformation on the lateral side seems to be guided by this translation, rather than by axial tension. Therefore, the presented values are the result of the actual expansion, minus the imposed translation. This effect is also apparent in Figure 15, showing the borderlines of the structure through time. Due to this translation, the lateral expansion cannot be maintained along the complete border. The mean maximum expansion therefore travels along the lateral border, from top to bottom, with increasing off-axial compression.

The absence of the transitional region and the addition of continuous vertical ribs, resulted in a more evenly distributed bilateral expansion. The vertical ribs enhanced the structures' bending stiffness, increasing the opportunity for the re-entrant cells to deform under axial tension. Hybrid Type 6 exhibited the most evenly distributed bilateral expansion, with significant differences in many of the data points, which is not surprising given the Poisson's ratios of the mechanical metamaterials used.

More surprising is the larger lateral expansion found for hybrid Types 2 and 5, compared to hybrid Types 1 and 4. In addition, hybrid Types 1 and 4 showed a bigger on the medial side of these structures, compared to hybrid Types 2 and 5. These results contradict the expectations, considering the positive relation between the absolute Poisson's ratio and the re-entrant and internal angles. It may suggest that the relatively high Modulus on the medial side of hybrid Types 2 and 5, limits the translation once again, and enhances the lateral deformation due to axial tension. However, since the differences are insignificant and the expansions exhibited at the bottom of the structure do match the expectations, the mean expansions of the deviant data points may again have been affected by a confounding variable.

The strain distributions on the "closed" hybrid mechanical metamaterials match the aforementioned predictions. Positive strains are created in places where the material is stretched, as a result of specimen expansion, and negative strains, on the other hand, arise in places where the specimen moves away from this surrounding layer. The results in Figure 16 show that the lateral side of hybrid Types 2 and 5, which are filled with 85-degree re-entrant hexagonal unit cells, show the least expansion. Their medial side, however, shows the most positive strains, caused by the expansion of 130-degree conventional hexagonal unit cells. Hybrid Type 6 is the only design showing an obvious bilateral expansion, extending along the complete lateral and medial border. Most of the negative strains are centrally located, and indicate material shrinkage (relaxation). This suggests that the transitional region is horizontally compressed as a result of the bilateral expansion of both mechanical metamaterials. The pre-stressed tape could therefore locally relax.

The simulation results confirm the potential of a hybrid structure in bending situations where a bilateral expansion is desired. Both sides clearly expand, although the effects are partially undone due to the translation imposed by the off-axial loading. The auxetic mechanical metamaterial shows a clear expansion on the lateral side, whereas the conventional mechanical metamaterial primarily expands on the medial side. The simulations also confirmed the lacking expansion found in the experiments at the medial bottom of the hybrid, corresponding to P26 and P29. The load applied by the clamp limited the ability of the lateral cells to deform, and will therefore have affected the experimentally obtained expansions. Fortunately, the relative differences between the specimens were not influenced since the clamping force was consistently applied throughout the experiments. Three-dimensions models will be needed to accurate predict the deformation profile of the hybrid mechanical metamaterials.

4.3 META-IMPLANTS

Based on the bilateral expansion found in Hybrid Type 6 (Section 4.2), this structure was chosen to be implemented in the hybrid meta-implant. The constituents of this hybrid, an auxetic and a conventional mechanical metamaterial, were used to build the two control meta-implants. A small sub-study was created with the introduction of Hybrid meta-implant Type 2 and Type 3. The effects of a solid core and a 70/30 ratio (re-entrant vs. conventional cells) could therefore be evaluated.

The results on the meta-implants clearly show a difference between the controls and the hybrids. All meta-implants exhibited an expansion on the medial side, as expected, except for Control meta-implant Type 2. The medial side of Control meta-implant Type 2 should exhibit a shrinkage in response to the load. The medial compressive strains suggest that Control meta-implant Type 2 is too weak to resist the translating forces imposed by the off-axial. In other words, the structure's bending stiffness (K) did not prevent it from bending over. Hence, the structure did not get the chance to exhibit its negative Poisson's ratio behavior. The 2D simulations show a comparable deformation profile for the auxetic mechanical metamaterial. Although highly inimitable, this does increase the reliability of the observed deformation. Control meta-implant Type 1 did show the predicted deformation profile. The medial expansion and lateral retraction were both confirmed in the 2D simulations. However, there is no guarantee this structure did have sufficient bending stiffness to resist the imposed deformation. The significantly higher Modulus, compared to Control meta-implant Type 2 (section on mechanical metamaterials), does increase the likelihood of the bending stiffness (=K(E)) being sufficiently large for the results to reflect the effective deformation of the structure. The unique spots of positive strain that did show up along the lateral border of the controls, are probably the result of a slight misalignment between the foam and the meta-implants. This is not surprising, as the foam blocks were manually filed to size.

All hybrid meta-implants showed a bilateral expansion, with comparable strain distributions on the medial side. The positive strains along the lateral border of the meta-implants represent the typical negative Poisson's ratio behavior found in re-entrant hexagonal structures in tension. This suggests that the solid wall, in between the two subvolumes, gives the meta-implant enough stiffness to effectively deform. A bigger volume of re-entrant cells (Hybrid meta-implant Type 3) was not found to significantly increase the expansion. More advanced research will be needed to elucidate the effects of this parameter. Both hybrid Types 1 and 3 show a dispersed compression profile, whereas Hybrid meta-implant Type 2 shows to expand along the entire lateral border. This can probably be explained by the curved solid core, which will push the lateral unit cells out upon loading, thereby amplifying the expansion created by the auxetics themselves. A downside of this design is the increased implant stiffness, compared to the other meta-implants, which can cause stress shielding when surpassing the stiffness of bone.[14] A possible solution would be to replace this solid core by a dense porous structure, which can be tuned to exhibit an acceptable stiffness.[16] The enhanced compressive strain profile of Hybrid meta-implant Type 2, compared to the current generation of femoral stems (Control meta-implant Type 1), will potentially improve osseointegration[33] and hence limit aseptic loosening.[11,12]

The rigid foam blocks were found to exhibit a 95% closed cellular structure as compared to the open structure of cancellous bone.[52] This composition may suggest that the observed compressive strain values have been impaired, by an increased stiffness of the foam. However, the stiffness of the foam does approach the mean value found in OA cancellous bone, which verifies the relevance of the set-up.[53]

4.4 CHALLENGES AND LIMITATIONS

Due to the explorative nature of this study, there were a lot of challenges to overcome as well as limitations to take into account. The novelty of the work resulted in a rather limited number of research papers to fall back on, which resulted in a bottom-up design approach. The recent literary work done on the topology-property relationship in auxetic mechanical metamaterials was therefore of great help.[23] Recent advances in AM techniques have enabled the fabrication of highly complex nano/micro-architectures, which may exhibit unusual mechanical properties not usually found in nature. Formerly known as mechanical metamaterials, they have been exploited in the design of a meta-implant's porous region to exhibit a bilateral expansion when subjected to bending.

Porous microstructures have been increasingly utilized in orthopedic implants, for their reduced stiffness and hence limited mechanical mismatch between implant and bone.[14,16] However, flexible implants are not necessarily a favorable alternative as they have shown to induce high interfacial stresses.[21,38] A recent study therefore presents a fully porous femoral stem, designed to match the stiffness of the surrounding native bone. This implant was shown to substantially reduce the bone resorption secondary to stress shielding.[16] Tetrahedron based unit cells were used to obtain sufficient strength, despite its porous architecture. The unit cells used in the hybrid mechanical metamaterials mainly deform through bending and buckling of the cell ribs. Their deformation is therefore hindered by an increase in rib thickness[23], which means a compromise will need to be made between their strength and the ease to deform.

Bone tissue regeneration in/onto an implanted structure is a highly complex phenomenon. It encompasses a cascade of cellular and extracellular events, affected by mechanical loading, the material microarchitecture/ geometry and the substrate stiffness.[54,55] A successful implantation depends upon the careful selection of certain morphological parameters, including pore size, pore shape (curvature) and porosity. Currently, there are no criteria specifying the requirements for porosity and pore size for optimal bone ingrowth. Satisfying results have been obtained with porosities above 50% and pore sizes ranging between 50 and 800 μm.[54,56] Whereas the porosity of the hybrid mechanical metamaterials in this study complies with these values, the unit pore size is much bigger. Strut thickness is another one of these morphological parameters affecting the osseointegration of the implant.[33,54] Regarding pore shape, re-entrant and conventional hexagonal unit cells have been effectively applied in scaffolds to stimulate bone cell cultivation.[57,58] Current AM techniques are still bound by certain tolerances, which limits the design space of porous structures. Meeting one of the requirements will therefore often lead to a violation of another to ensure manufacturability. Additionally, the intrinsic interconnection between the abovementioned mechanisms makes it very hard to predict the magnitude of bone tissue regeneration as a result of the obtained compressive strain profiles.

Micro motions, defined by Goodman et al. (1994) as the “small movements between a prosthesis and the surrounding bone, that are not detectable with conventional radiographic methods”[59], have been found to contribute to aseptic loosening.[11] The deformations found in this study should therefore not be mistaken with deliberately induced micro motions. Instead, the hybrid meta-implant will actively respond to a decrease in bone-implant contact due to the Poisson’s effect. The living bone tissue, which is sensitive to mechanotransduction, will subsequently react by the formation of new bone.[19,20] Osseointegration will subsequently improve the mechanical properties of the bone-implant interface.[33] Little data is available on the exact consequences of this process in terms of interface stiffness. It is thus unclear whether the stiffness of these osseointegrated regions will ever surpass the stiffness of the surrounding bone.

4.3 POTENTIAL APPLICATIONS AND FUTURE WORK

This study resulted in a first proof of concept of hybrid mechanical metamaterials in femoral stems. Their graded Poisson’s ratio created a bilateral expansion upon loading at the femoral head, which resulted in a positive strain distribution in the “bone” surrounding the meta-implant. This would theoretically stimulate bone apposition and hence ensure osseointegration. Optimization of the structure will be necessary to verify its effectiveness in tackling the multitude of factors affecting the implant’s success. Future work would include the design of a representative 3D FEM model, to quickly assess the feasibility of the design choices. Just like Arabnejad et al. (2016), CT images can help in the design of a functionally graded structure that matches the stiffness of the surrounding native bone.[16] Subsequently, the stress profile of the hip stem can give insight in the distribution (ratio) of unit cells necessary to obtain a specific expansion profile. Further research will be necessary to see whether the expansion should extend along the complete circumference of the stem for optimal osseointegration. For optimal bone in- and ongrowth, morphological parameters such as the average pore size, pore shape and porosity, should also be taken into account.[54,55] Once all of these aspects have been addressed, the only thing left to discover is the resulting biological response of the living bone tissue. All things considered, there is a long way to go before actual clinical approval, but this study can be considered a first step towards personalized, life-lasting femoral stems.

Besides a bilateral expansion in bending situations, these hybrids can exhibit a unilateral deformation in response to uniaxial loading. These mechanical characteristics are potentially useful in expandable implants/ scaffolds, which can be used to fill irregular bone defects. The tunability of mechanical metamaterials, in terms of mechanical and physical properties, makes them potentially useful in dozens of industries.

5. CONCLUSION

In this study, several mechanical metamaterials were designed and subsequently fabricated using SLM. The lateral shrinkage observed during the axial compression of the auxetic mechanical metamaterials confirmed their NPR, which was shown to increase with re-entrant angle. The conventional mechanical metamaterials exhibited a lateral expansion, due to their positive Poisson's ratio, which was found to increase with internal angle. Their stiffness to weight ratios exceeded those found in the auxetic mechanical metamaterials, whereas the latter were found to exhibit a higher UCS. The continuous vertical ribs in the hybrid mechanical metamaterials were shown to increase the bending stiffness and hence the lateral expansion of the re-entrant cells upon off-axial compression. This resulted in a more evenly distributed bilateral expansion, especially in Hybrid Type 6. The proximal volume of the meta-implants was therefore filled with the constituents of this hybrid, after which they were synthesized by SLM. Hybrid meta-implant Type 2, with a 50/50 ratio and a solid core, initiated a continuous compression profile along both of its borders. This was found to significantly differ from the compression initiated by Control meta-implant type 1, which represented the current generation of femoral stems. Hybrid mechanical metamaterials have therefore been proven effective in off-axially loaded meta-implants, to initiate bilateral strains and potentially stimulate osseointegration at the bone-implant interface.

6. ABBREVIATIONS

DIC	Digital Image Correlation
DMP	Direct Metal Printing
EDM	Electrical Discharge Machining
ELI	Extra Low Interstitials
FLTR	From Left to Right
NPR	Negative Poisson's Ratio
OA	Osteoarthritis
SLM	Selective Laser Melting
STL	STereoLithography (file format)
THR	Total Hip Replacement
UCS	Ultimate Compressive Strength

7. REFERENCES

1. Economic, U.N.D.o., S. Affairs, and P. Division, World Population Prospects: The 2015 Revision, Key Findings and Advance Tables. *Working Paper, No. ESA/P/WP. 241.,* 2015.

2. Kurtz, S., et al., Projections of primary and revision hip and knee arthroplasty in the United States from 2005 to 2030. *J Bone Joint Surg Am*, 2007. *89*(4): p. 780-785.

3. Kremers, H.M., et al., Prevalence of total hip and knee replacement in the United States. *J Bone Joint Surg Am,* 2015*. 97*(17): p. 1386-1397.

4. Caton, J. and J.L. Prudhon, Over 25 years survival after Charnley's total hip arthroplasty. *International orthopaedics,* 2011*. 35*(2): p. 185-188.

5. Ateschrang, A., et al., Long-term results using the straight tapered femoral cementless hip stem in total hip arthroplasty: a minimum of twenty-year follow-up. *The Journal of arthroplasty*, 2014. *29*(8): p. 1559-1565.

6. Corbett, K.L., et al., Population-based rates of revision of primary total hip arthroplasty: a systematic review. *PLoS One*, 2010. *5*(10): p. e13520.

7. Mäkelä, K.T., et al., Failure rate of cemented and uncemented total hip replacements: register study of combined Nordic database of four nations. *Bmj*, 2014. *348*: p. f7592.

8. MacInnes, S.J., A. Gordon, and J.M. Wilkinson, Risk factors for aseptic loosening following total hip arthroplasty. *Pain*, 2012. *2*: p. 29.

9. Prudhon, J.-L., et al., Causes for revision of dual-mobility and standard primary total hip arthroplasty. *International orthopaedics*, 2015: p. 1-5.

10. Bozic, K.J., et al., The epidemiology of revision total hip arthroplasty in the United States. *J Bone Joint Surg Am*, 2009. *91*(1): p. 128-133.

11. Sundfeldt, M., et al., Aseptic loosening, not only a question of wear: a review of different theories. *Acta orthopaedica*, 2006. *77*(2): p. 177-197.

12. Abu-Amer, Y., I. Darwech, and J.C. Clohisy, Aseptic loosening of total joint replacements: mechanisms underlying osteolysis and potential therapies. *Arthritis research & therapy*, 2007. *9*(1): p. S6.

13. Sumner, D., et al., Functional adaptation and ingrowth of bone vary as a function of hip implant stiffness. *Journal of biomechanics*, 1998. *31*(10): p. 909-917.

14. Sumner, D., Long-term implant fixation and stress-shielding in total hip replacement. *Journal of biomechanics*, 2015. *48*(5): p. 797-800.

15. Bobyn, J.D., et al., Producing and Avoiding Stress Shielding: Laboratory and Clinical Observations of Noncemented Total Hip Arthroplasty. *Clinical orthopaedics and related research*, 1992. 274: p. 79-96.

16. Arabnejad, S., et al., Fully porous 3D printed titanium femoral stem to reduce stress-shielding following total hip arthroplasty. *Journal of Orthopaedic Research*, 2016.

17. Heinl, P., et al., Cellular Ti–6Al–4V structures with interconnected macro porosity for bone implants fabricated by selective electron beam melting. *Acta biomaterialia*, 2008. *4*(5): p. 1536-1544.

18. Poisson, S. *Note sur l'extension des fils et des plaques élastiques*. in Annales de Chimie et de Physique. 1827.

19. Chamay, A. and P. Tschantz, Mechanical influences in bone remodeling. Experimental research on Wolff's law. *Journal of biomechanics*, 1972. *5*(2): p. 173-180.

20. Christen, P., et al., Bone remodelling in humans is load-driven but not lazy. *Nature communications*, 2014. *5*.

21. Weinans, H., R. Huiskes, and H.J. Grootenboer, Effects of material properties of femoral hip components on bone remodeling. *Journal of Orthopaedic Research*, 1992. *10*(6): p. 845-853.

22. Zadpoor, A.A., Mechanical meta-materials. *Materials Horizons*, 2016.

23. Kolken, H. and A. Zadpoor, Auxetic mechanical metamaterials. *RSC Advances*, 2017. *7*(9): p. 5111-5129.

24. Cai, W., et al., Optical cloaking with metamaterials. *Nature photonics*, 2007. *1*(4): p. 224-227.

25. Shalaev, V.M., Optical negative-index metamaterials. *Nature photonics*, 2007. *1*(1): p. 41-48.

26. Smith, D.R., J.B. Pendry, and M.C. Wiltshire, Metamaterials and negative refractive index. *Science*, 2004. *305*(5685): p. 788-792.

27. Mark, A.G., et al. *Auxetic metamaterial simplifies soft robot design*. in Robotics and Automation (ICRA), 2016 IEEE International Conference on. 2016. IEEE.

28. Zhu, R., et al., Bifunctional acoustic metamaterial lens designed with coordinate transformation. *Applied Physics Letters*, 2017. *110*(11): p. 113503.

29. Bobbert, F., et al., Additively manufactured metallic porous biomaterials based on minimal surfaces: A unique combination of topological, mechanical, and mass transport properties. *Acta Biomaterialia*, 2017. *53*: p. 572-584.

30. Gómez, S., et al., Design and properties of 3D scaffolds for bone tissue engineering. *Acta biomaterialia*, 2016. *42*: p. 341-350.

31. Kim, H.N., et al., Nanotopography-guided tissue engineering and regenerative medicine. *Advanced drug delivery reviews*, 2013. *65*(4): p. 536-558.

32. Amin Yavari, S., et al., Antibacterial behavior of additively manufactured porous titanium with nanotubular surfaces releasing silver ions. *ACS applied materials & interfaces*, 2016. *8*(27): p. 17080-17089.

33. Ramazanoglu, M. and Y. Oshida, *Osseointegration and bioscience of implant surfaces-current concepts at bone-implant interface*. 2011: INTECH Open Access Publisher.

34. Love, A.E.H., *A treatise on the mathematical theory of elasticity*. Vol. 1. 2013: Cambridge University Press.

35. Hou, Y., et al., Graded conventional-auxetic Kirigami sandwich structures: Flatwise compression and edgewise loading. *Composites Part B: Engineering*, 2014. *59*: p. 33-42.

36. Abdelaal, O. and S. Darwish, Analysis, fabrication and a biomedical application of auxetic cellular structures. *Int J Eng Innov Technol*, 2012. *2*(3): p. 218-23.

37. Yang, D., S. Lee, and F. Huang, Geometric effects on micropolar elastic honeycomb structure with negative Poisson's ratio using the finite element method. *Finite elements in analysis and design*, 2003. *39*(3): p. 187-205.

38. Huiskes, R., H. Weinans, and B. Van Rietbergen, The relationship between stress shielding and bone resorption around total hip stems and the effects of flexible materials. *Clinical orthopaedics and related research*, 1992. *274*: p. 124-134.

39. Zimmer. Fitmore hip stem. 2009 [accessed 24 Feb, 2017]; Available from: http://www.zimmer.com/content/dam/zimmer-web/documents/en-US/pdf/medical-professionals/hip/Fitmore-Hip-Stem-Brochure-97-0551-001-00-04-2010-US-MARKETS-ONLY.pdf.

40. Guo, N. and M.C. Leu, Additive manufacturing: technology, applications and research needs. *Frontiers of Mechanical Engineering*, 2013. *8*(3): p. 215-243.

41. Yap, C., et al., Review of selective laser melting: Materials and applications. *Applied Physics Reviews*, 2015. *2*(4): p. 041101.

42. Dynamet Holdings, I. Titanium Alloy Ti 6Al-4V ELI. 2017; Available from: http://cartech.ides.com/datasheet.aspx?i=101&E=268.

43. Sawbones. FINAL_Biomechanical_Catalog.pdf. 2017; Available from: http://live.sawbones.com/wp/wp-content/uploads/2017/04/FINAL_Biomechanical_Catalog.pdf.

44. McCormick, N. and J. Lord, Digital image correlation. *Materials today,* 2010. *13*(12): p. 52-54.

45. Oldani, C., A. Dominguez, and T. Eli, *Titanium as a Biomaterial for Implants*. 2012: Citeseer.

46. Field, A., *Discovering statistics using IBM SPSS statistics*. 2013: Sage.

47. Laerd Statistics. Kruskal-Wallis H Test in SPSS Statistics | Procedure, output and interpretation of the output using a relevant example. 2017; Available from: https://statistics.laerd.com/spss-tutorials/kruskal-wallis-h-test-using-spss-statistics.php.

48. Gibson, L.J. and M.F. Ashby, *Cellular solids: structure and properties*. 1999: Cambridge university press.

49. Yang, L., et al., Compressive properties of Ti–6Al–4V auxetic mesh structures made by electron beam melting. *Acta Materialia*, 2012. *60*(8): p. 3370-3379.

50. Wang, K., et al., Designable dual-material auxetic metamaterials using three-dimensional printing. *Materials & Design*, 2015. *67*: p. 159-164.

51. Li, D., L. Dong, and R.S. Lakes, A unit cell structure with tunable Poisson's ratio from positive to negative. *Materials Letters*, 2016. *164*: p. 456-459.

52. Matweb. Sawbones Cellular Rigid Polyurethane Foam 7.5 pcf Density. 2017; Available from: http://www.matweb.com/search/datasheettext.aspx?matguid=e51e97578f334c3e913308b7f654e1cf.

53. Li, B. and R.M. Aspden, Composition and mechanical properties of cancellous bone from the femoral head of patients with osteoporosis or osteoarthritis. *Journal of Bone and Mineral Research*, 1997. *12*(4): p. 641-651.

54. Arabnejad, S., et al., High-strength porous biomaterials for bone replacement: A strategy to assess the interplay between cell morphology, mechanical properties, bone ingrowth and manufacturing constraints. *Acta biomaterialia*, 2016. *30*: p. 345-356.

55. Zadpoor, A.A., Bone tissue regeneration: the role of scaffold geometry. *Biomaterials science*, 2015. *3*(2): p. 231-245.

56. Bragdon, C.R., et al., Biologic fixation of total hip implants. *J Bone Joint Surg Am*, 2004. *86* (suppl 2): p. 105-117.

57. Choi, H.J., et al., MG-63 osteoblast-like cell proliferation on auxetic PLGA scaffold with mechanical stimulation for bone tissue regeneration. *Biomaterials Research*, 2016. *20*(1): p. 33.

58. Zhao, H. and W. Liang, A novel comby scaffold with improved mechanical strength for bone tissue engineering. *Materials Letters*, 2017. *194*: p. 220-223.

59. Goodman, S.B., The effects of micromotion and particulate materials on tissue differentiation: bone chamber studies in rabbits. *Acta Orthopaedica Scandinavica*, 1994. *65*(sup258): p. 1-43.

8. APPENDICES

8.1 DIC RESULTS - MECHANICAL METAMATERIALS

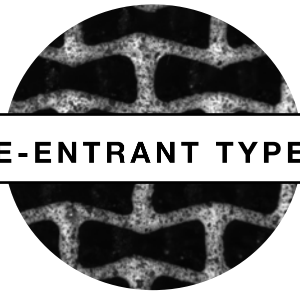

RE-ENTRANT TYPE 1

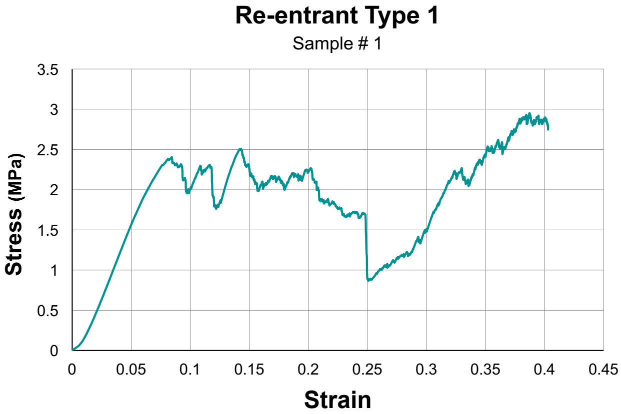

	H	W	D
DIMENSIONS (mm)	24.82	25.70	25.65
E-MODULUS	35.79 MPa		
U. COMPRESSIVE STRENGTH	2.39 MPa		
YIELD STRAIN	0.0813		
RELATIVE DENSITY	-		

	H	W	D
DIMENSIONS (mm)	24.82	25.80	25.50
E-MODULUS	34.26 MPa		
U. COMPRESSIVE STRENGTH	2.53 MPa		
YIELD STRAIN	0.0931		
RELATIVE DENSITY	0.0760		

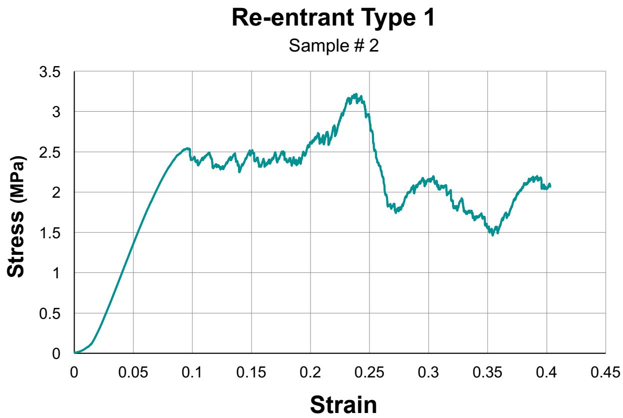

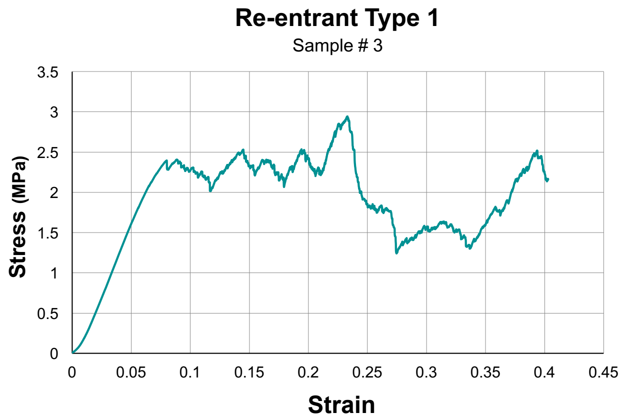

	H	W	D
DIMENSIONS (mm)	24.82	25.70	25.70
E-MODULUS	35.85 MPa		
U. COMPRESSIVE STRENGTH	2.39 MPa		
YIELD STRAIN	0.0793		
RELATIVE DENSITY	0.0771		

	H	W	D
DIMENSIONS (mm)	24.82	26.10	25.70
E-MODULUS	35.32 MPa		
U. COMPRESSIVE STRENGTH	2.32 MPa		
YIELD STRAIN	0.0779		
RELATIVE DENSITY	-		

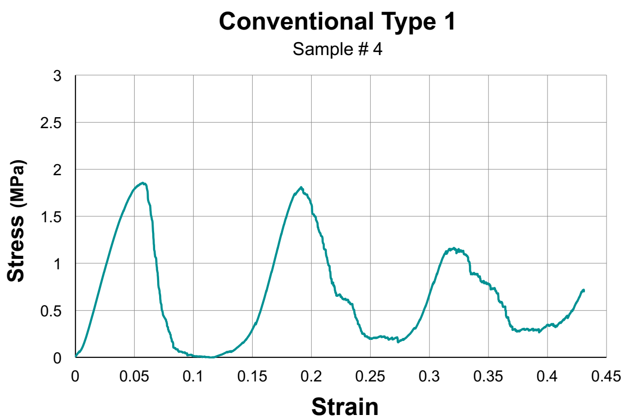

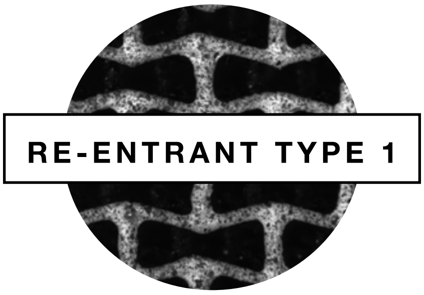

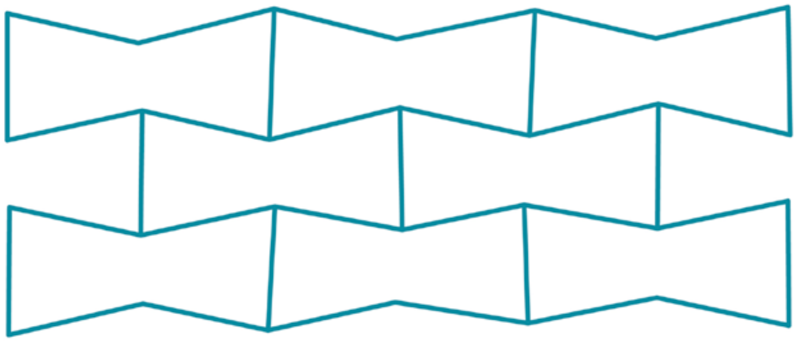

RE-ENTRANT TYPE 1
MASTER THESIS ELINE KOLKEN

Video A1: Deformation of Re-entrant Type 1 through time - Press to play -

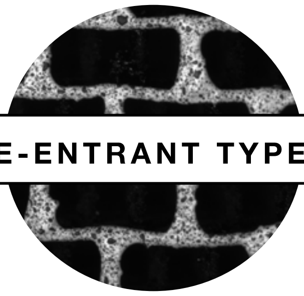

RE-ENTRANT TYPE 2

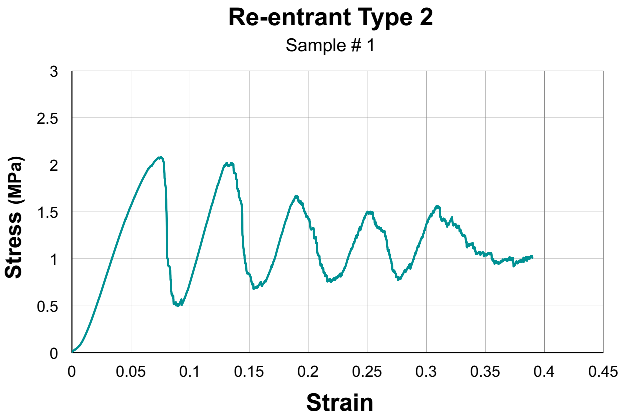

	H	W	D
DIMENSIONS (mm)	25.65	26.20	25.50
E-MODULUS	35.48 MPa		
U. COMPRESSIVE STRENGTH	2.05 MPa		
YIELD STRAIN	0.0708		
RELATIVE DENSITY	0.0606		

	H	W	D
DIMENSIONS (mm)	25.65	26.00	25.55
E-MODULUS	38.40 MPa		
U. COMPRESSIVE STRENGTH	2.12 MPa		
YIELD STRAIN	0.0680		
RELATIVE DENSITY	0.0623		

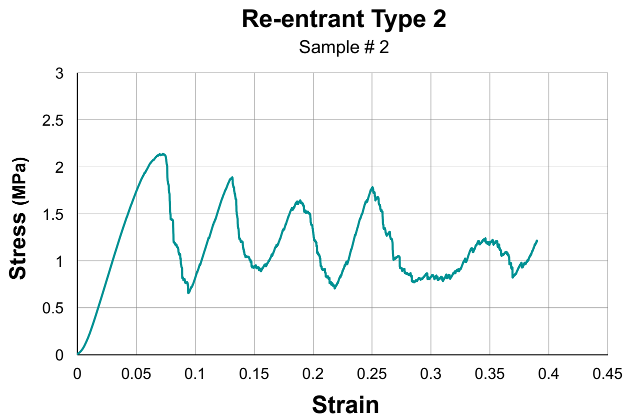

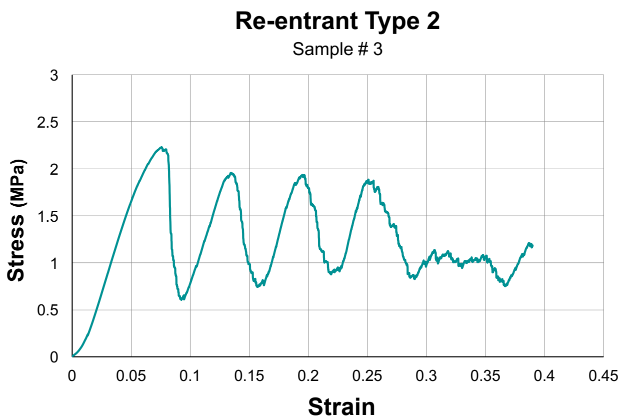

	H	W	D
DIMENSIONS (mm)	25.65	25.00	25.60
E-MODULUS	37.97 MPa		
U. COMPRESSIVE STRENGTH	2.23 MPa		
YIELD STRAIN	0.0755		
RELATIVE DENSITY	0.0633		

	H	W	D
DIMENSIONS (mm)	25.65	26.00	25.50
E-MODULUS	38.85 MPa		
U. COMPRESSIVE STRENGTH	2.27 MPa		
YIELD STRAIN	0.0717		
RELATIVE DENSITY	0.0597		

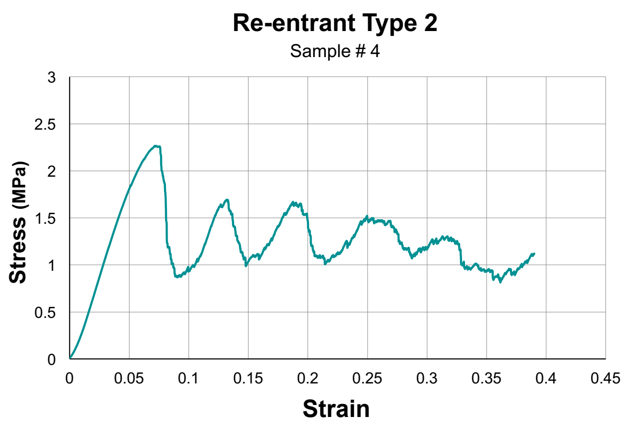

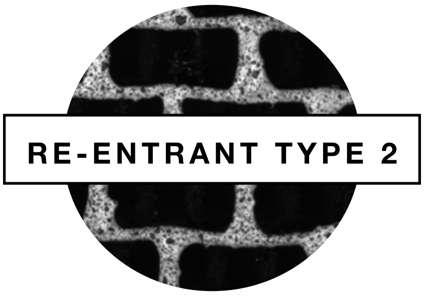

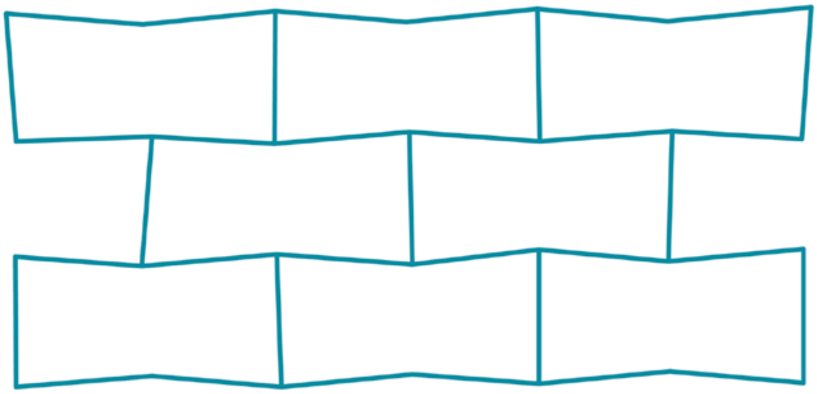

RE-ENTRANT TYPE 2
MASTER THESIS ELINE KOLKEN

Video A2: Deformation of Re-entrant Type 2 through time - Press to play -

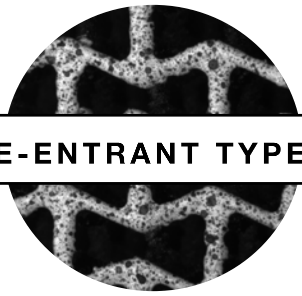

RE-ENTRANT TYPE 3

	H	W	D
DIMENSIONS (mm)	27.21	26.20	26.00
E-MODULUS	41.65 MPa		
U. COMPRESSIVE STRENGTH	2.37 MPa		
YIELD STRAIN	0.0642		
RELATIVE DENSITY	0.0719		

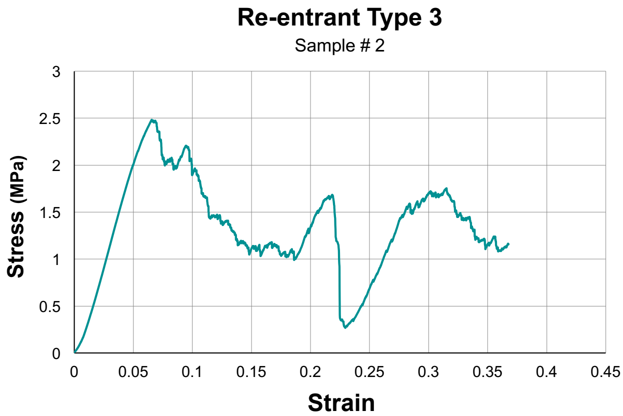

	H	W	D
DIMENSIONS (mm)	27.21	26.10	25.70
E-MODULUS	44.56 MPa		
U. COMPRESSIVE STRENGTH	2.48 MPa		
YIELD STRAIN	0.0654		
RELATIVE DENSITY	0.0742		

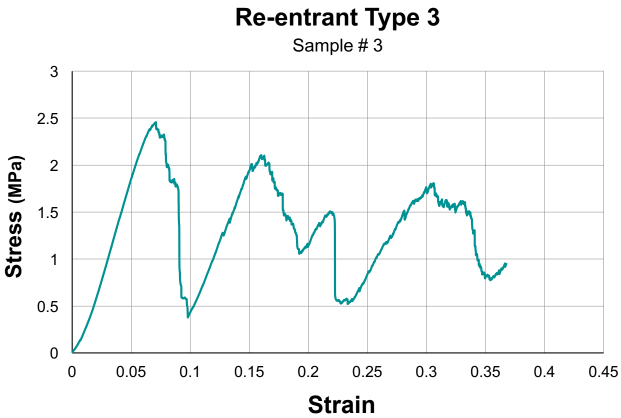

	H	W	D
DIMENSIONS (mm)	27.21	25.95	25.95
E-MODULUS	40.96 MPa		
U. COMPRESSIVE STRENGTH	2.42 MPa		
YIELD STRAIN	0.0677		
RELATIVE DENSITY	0.0727		

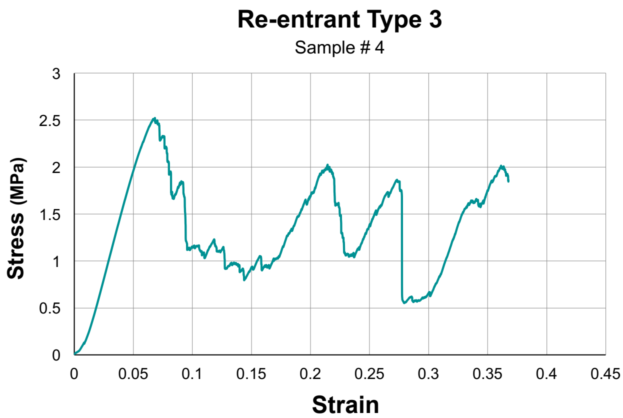

	H	W	D
DIMENSIONS (mm)	27.21	26.00	25.60
E-MODULUS	45.51 MPa		
U. COMPRESSIVE STRENGTH	2.48 MPa		
YIELD STRAIN	0.0652		
RELATIVE DENSITY	0.0735		

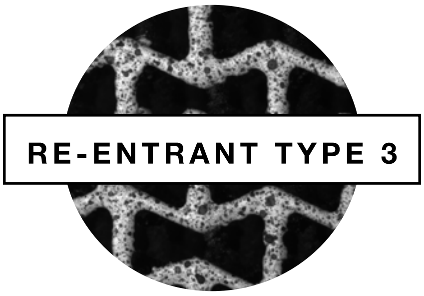

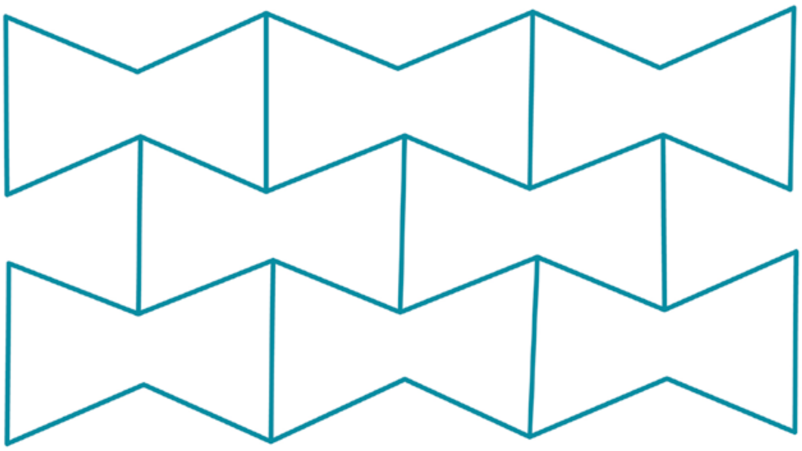

RE-ENTRANT TYPE 3
MASTER THESIS ELINE KOLKEN

Video A3: Deformation of Re-entrant Type 3 through time - Press to play -

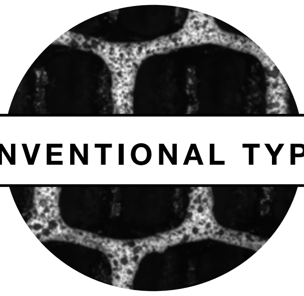

CONVENTIONAL TYPE 1

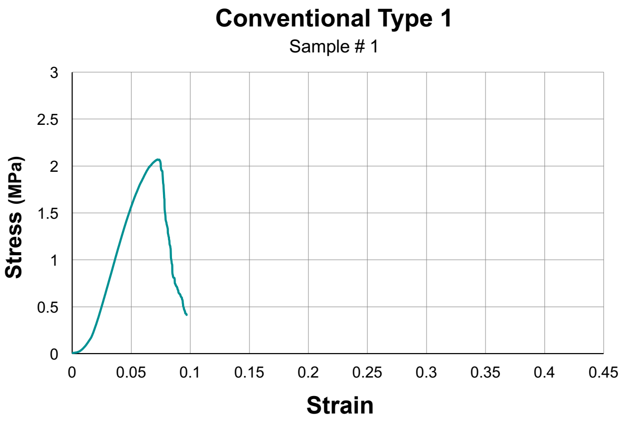

	H	W	D
DIMENSIONS (mm)	23.21	25.75	25.65
E-MODULUS	39.61 MPa		
U. COMPRESSIVE STRENGTH	2.07 MPa		
YIELD STRAIN	0.0723		
RELATIVE DENSITY	0.0486		

	H	W	D
DIMENSIONS (mm)	23.21	26.00	25.90
E-MODULUS	41.62 MPa		
U. COMPRESSIVE STRENGTH	1.98 MPa		
YIELD STRAIN	0.0595		
RELATIVE DENSITY	0.0477		

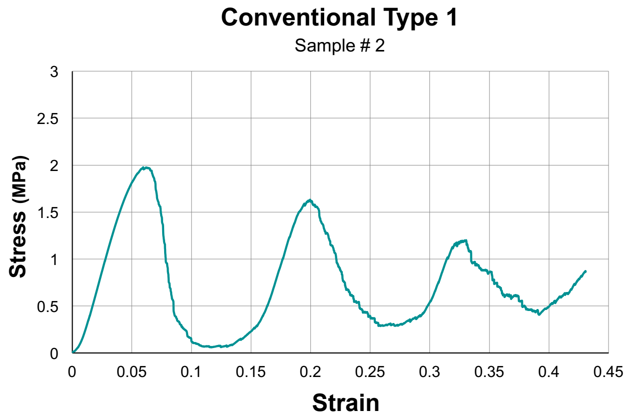

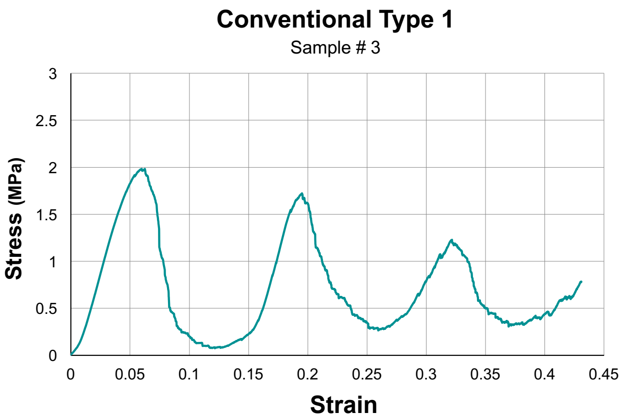

	H	W	D
DIMENSIONS (mm)	23.21	26.10	25.80
E-MODULUS	41.88 MPa		
U. COMPRESSIVE STRENGTH	1.98 MPa		
YIELD STRAIN	0.0598		
RELATIVE DENSITY	0.0477		

	H	W	D
DIMENSIONS (mm)	23.21	26.10	25.80
E-MODULUS	39.79 MPa		
U. COMPRESSIVE STRENGTH	1.85 MPa		
YIELD STRAIN	0.0590		
RELATIVE DENSITY	0.0491		

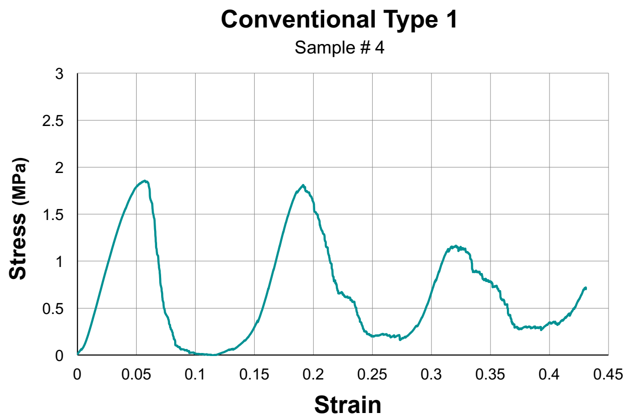

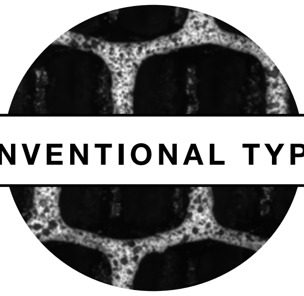

CONVENTIONAL TYPE 1

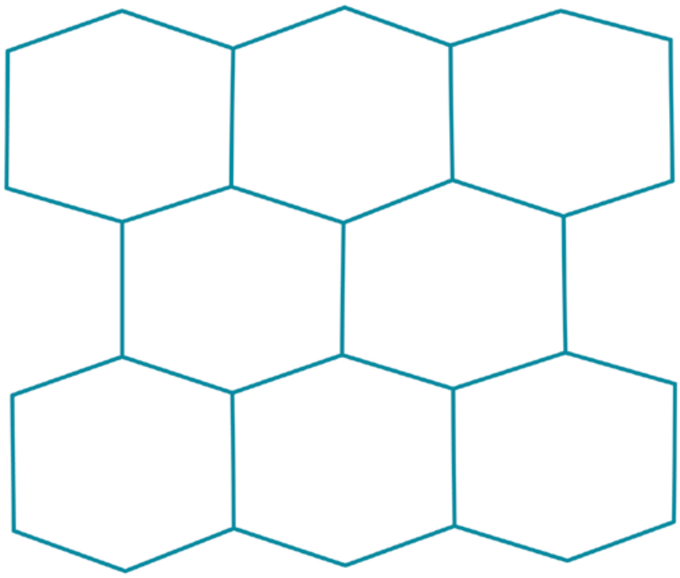

CONVENTIONAL TYPE 1
MASTER THESIS ELINE KOLKEN

Video A4: Deformation of Conventional Type 1 through time - Press to play -

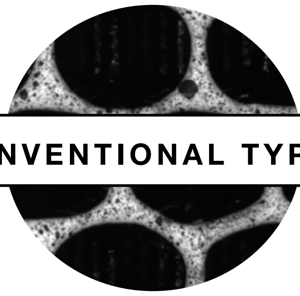

CONVENTIONAL TYPE 2

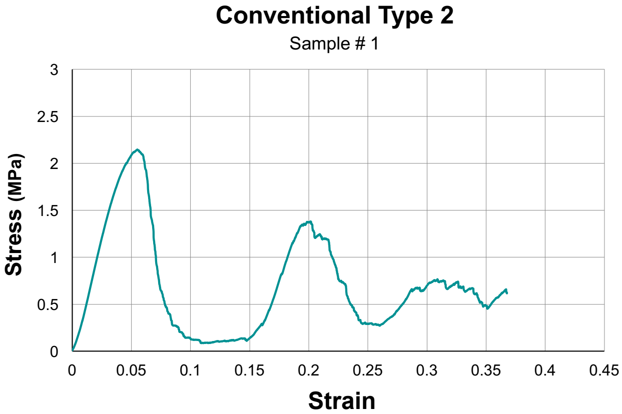

	H	W	D
DIMENSIONS (mm)	27.20	26.10	25.70
E-MODULUS	49.11 MPa		
U. COMPRESSIVE STRENGTH	2.15 MPa		
YIELD STRAIN	0.0550		
RELATIVE DENSITY	0.0458		

	H	W	D
DIMENSIONS (mm)	27.20	25.75	25.60
E-MODULUS	52.19 MPa		
U. COMPRESSIVE STRENGTH	2.23 MPa		
YIELD STRAIN	0.0584		
RELATIVE DENSITY	0.0466		

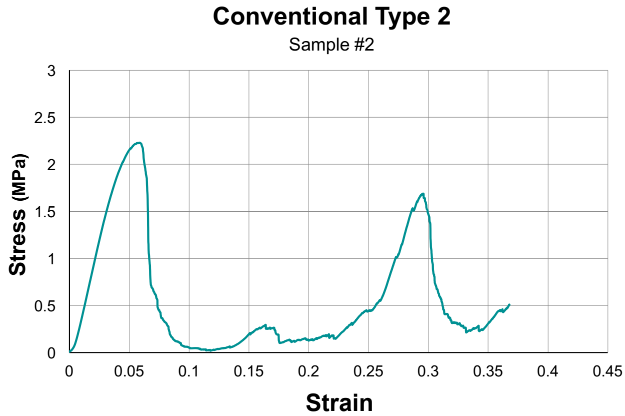

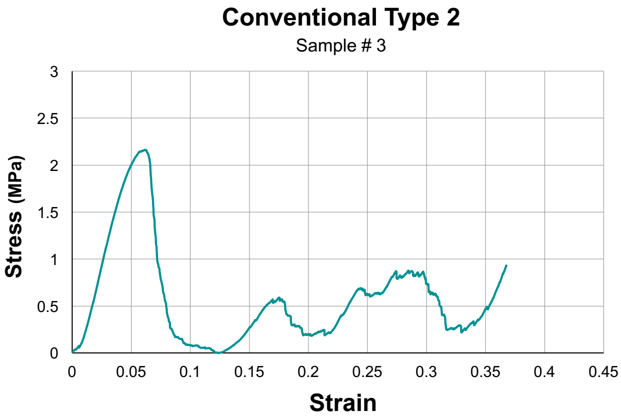

	H	W	D
DIMENSIONS (mm)	27.20	25.90	25.90
E-MODULUS	49.68 MPa		
U. COMPRESSIVE STRENGTH	2.16 MPa		
YIELD STRAIN	0.0617		
RELATIVE DENSITY	0.0458		

	H	W	D
DIMENSIONS (mm)	27.20	25.90	25.80
E-MODULUS	49.87 MPa		
U. COMPRESSIVE STRENGTH	2.09 MPa		
YIELD STRAIN	0.0525		
RELATIVE DENSITY	0.0472		

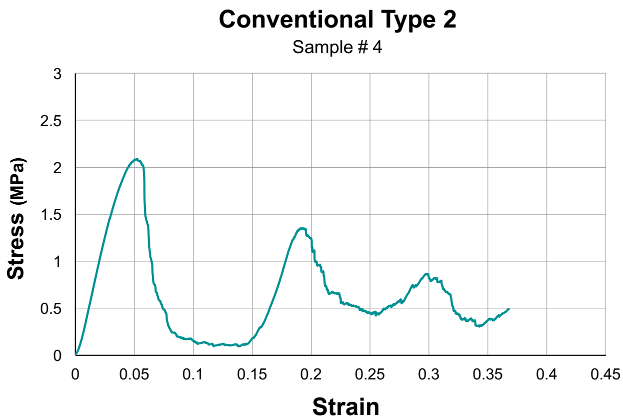

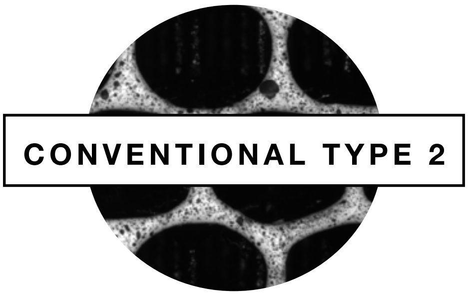

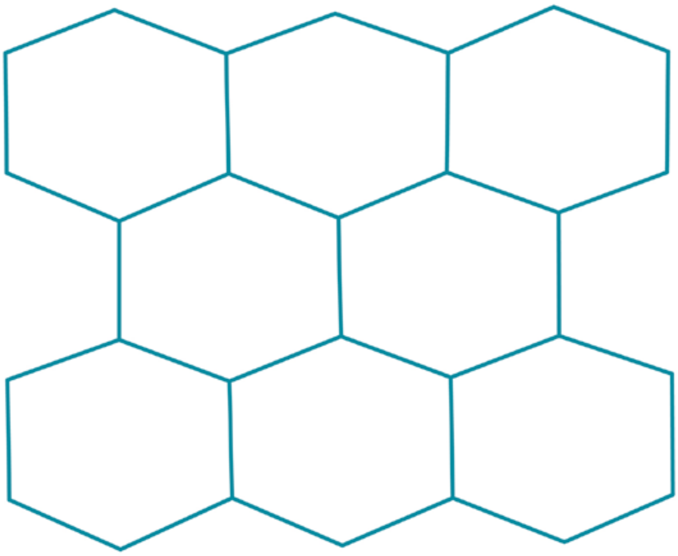

CONVENTIONAL TYPE 2
MASTER THESIS ELINE KOLKEN

Video A5: Deformation of Conventional Type 2 through time - Press to play -

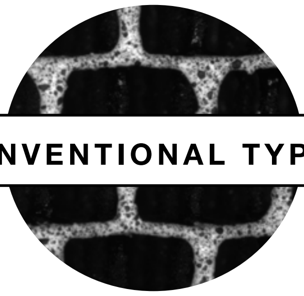

CONVENTIONAL TYPE 3

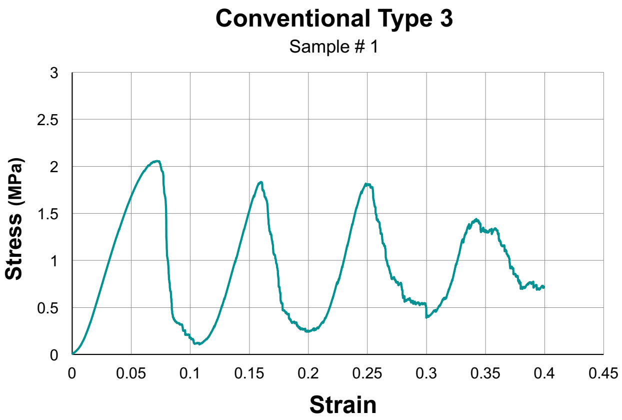

	H	W	D
DIMENSIONS (mm)	25.03	26.00	25.80
E-MODULUS	38.32 MPa		
U. COMPRESSIVE STRENGTH	2.06 MPa		
YIELD STRAIN	0.0716		
RELATIVE DENSITY	0.0524		

	H	W	D
DIMENSIONS (mm)	25.03	26.20	25.70
E-MODULUS	39.00 MPa		
U. COMPRESSIVE STRENGTH	2.03 MPa		
YIELD STRAIN	0.0678		
RELATIVE DENSITY	0.0522		

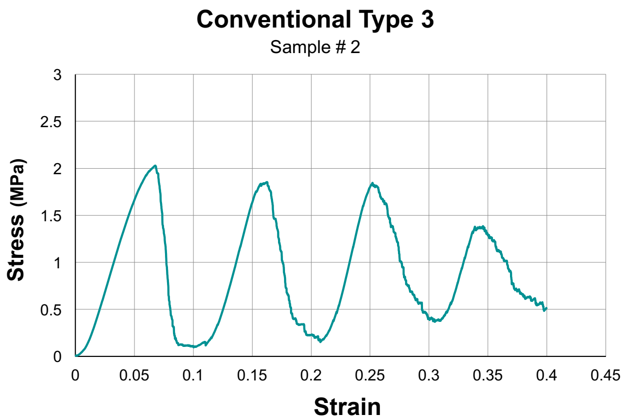

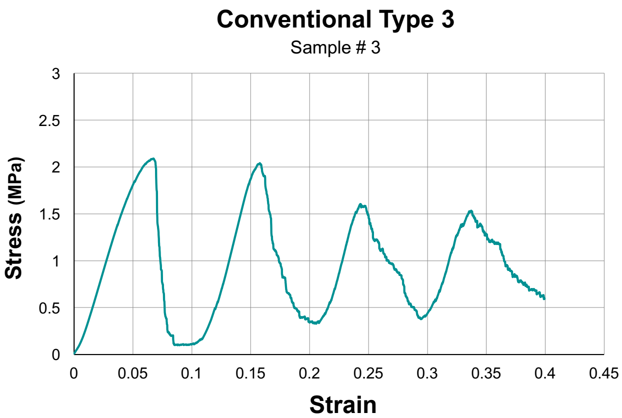

	H	W	D
DIMENSIONS (mm)	25.03	26.00	25.80
E-MODULUS	38.93 MPa		
U. COMPRESSIVE STRENGTH	2.09 MPa		
YIELD STRAIN	0.0674		
RELATIVE DENSITY	0.0524		

	H	W	D
DIMENSIONS (mm)	25.03	26.10	25.60
E-MODULUS	39.19 MPa		
U. COMPRESSIVE STRENGTH	2.02 MPa		
YIELD STRAIN	0.0657		
RELATIVE DENSITY	0.0513		

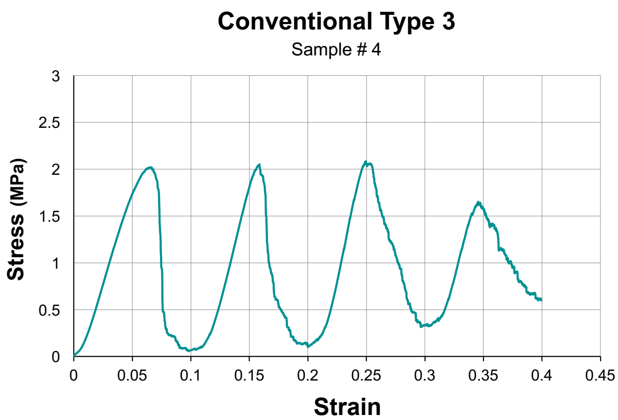

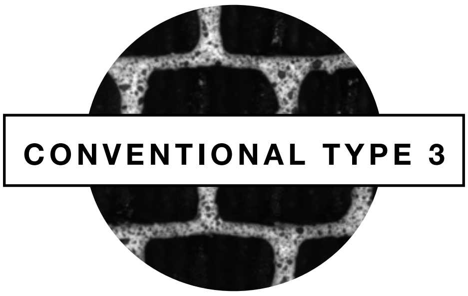

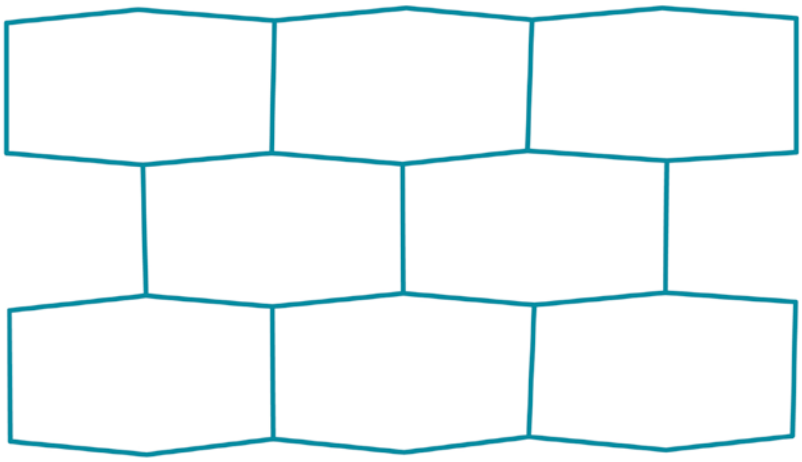

CONVENTIONAL TYPE 3
MASTER THESIS ELINE KOLKEN

Video A6: Deformation of Conventional Type 3 through time - Press to play -

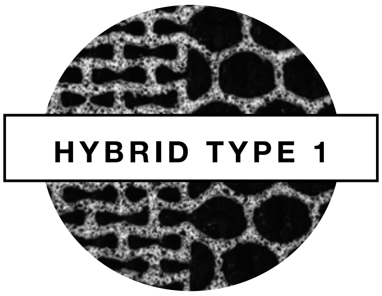

HYBRID TYPE 1

HYBRID TYPE 1 - SAMPLE #1

Mean maximum expansion (mm)

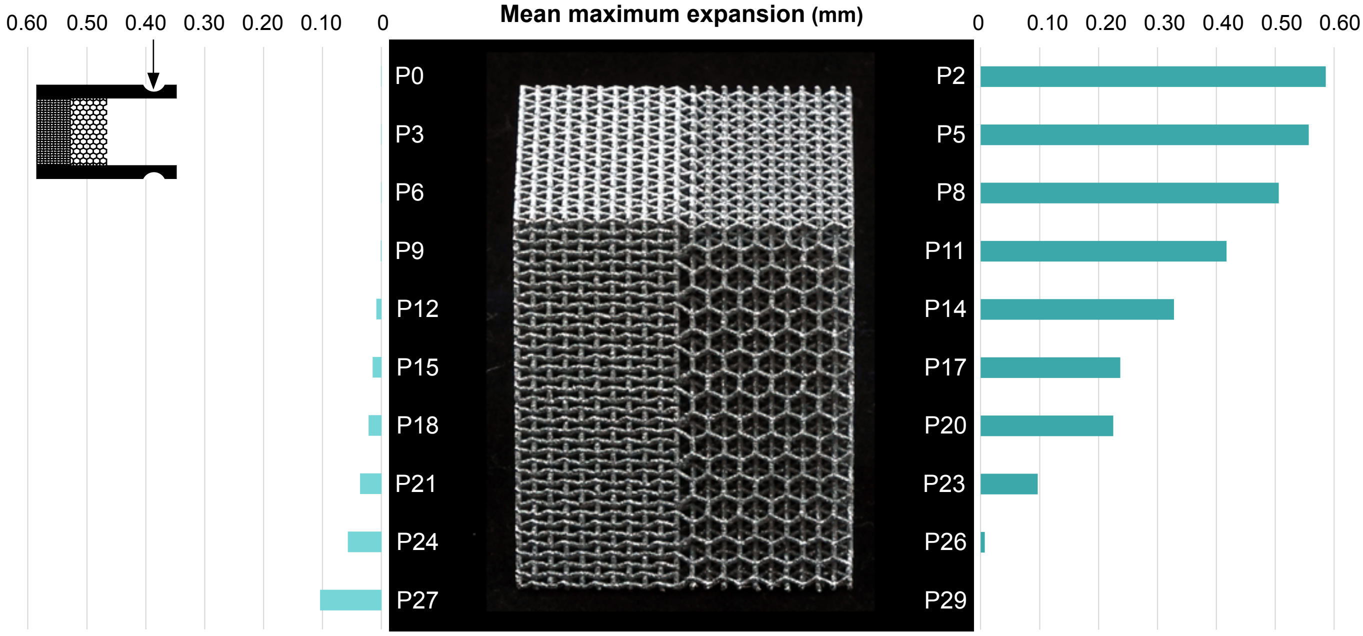

HYBRID TYPE 1 - SAMPLE #2

Mean maximum expansion (mm)

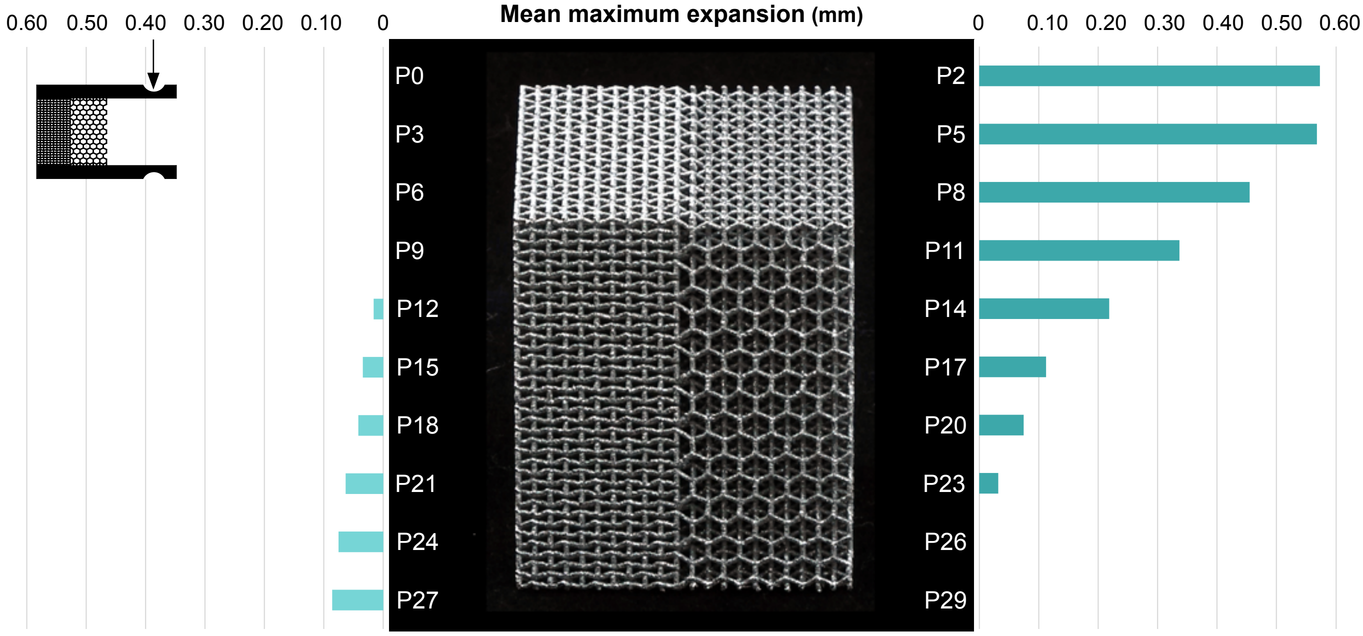

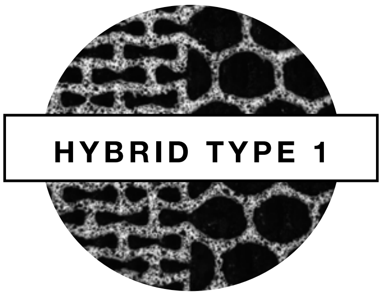

HYBRID TYPE 1 - SAMPLE #3

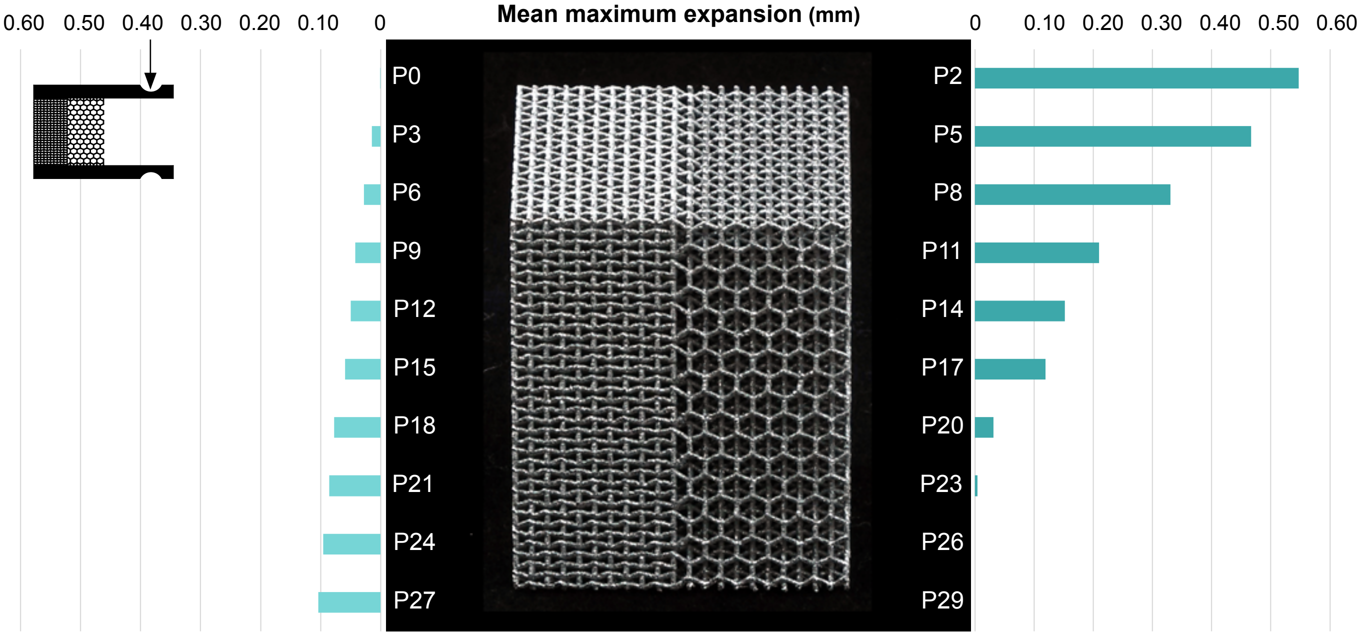

HYBRID TYPE 1 - SAMPLE #4

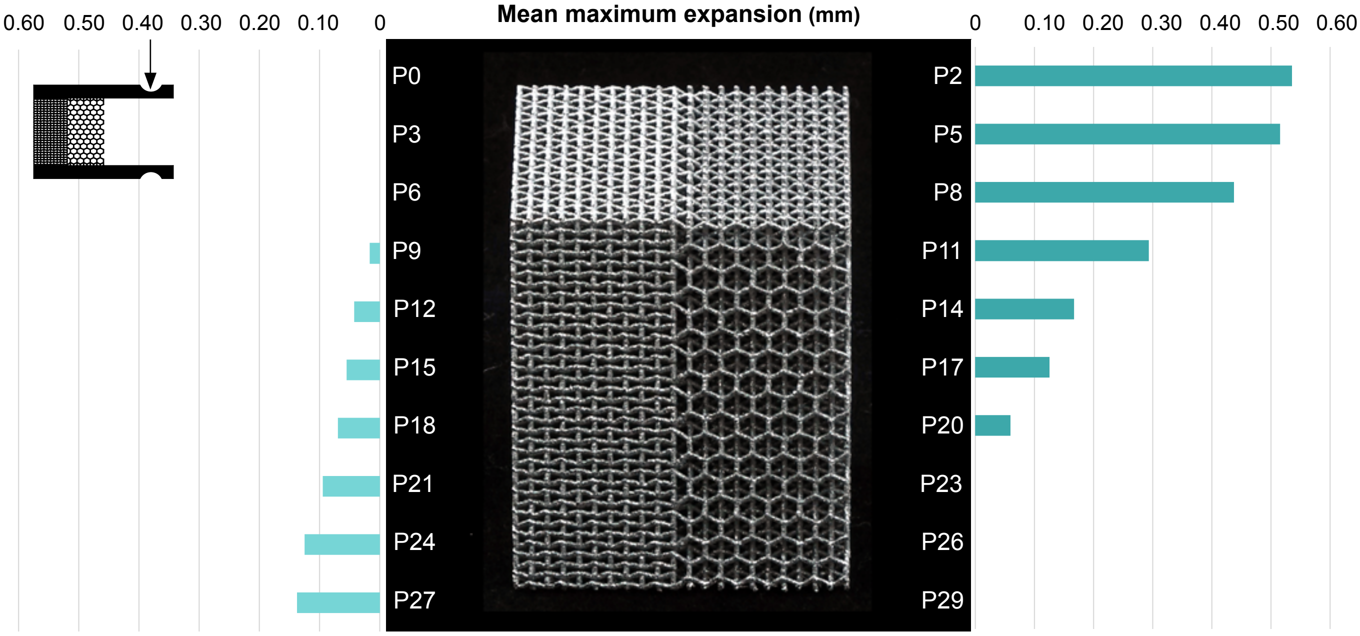

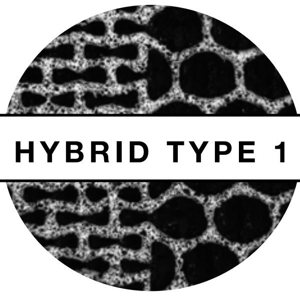

HYBRID TYPE 1

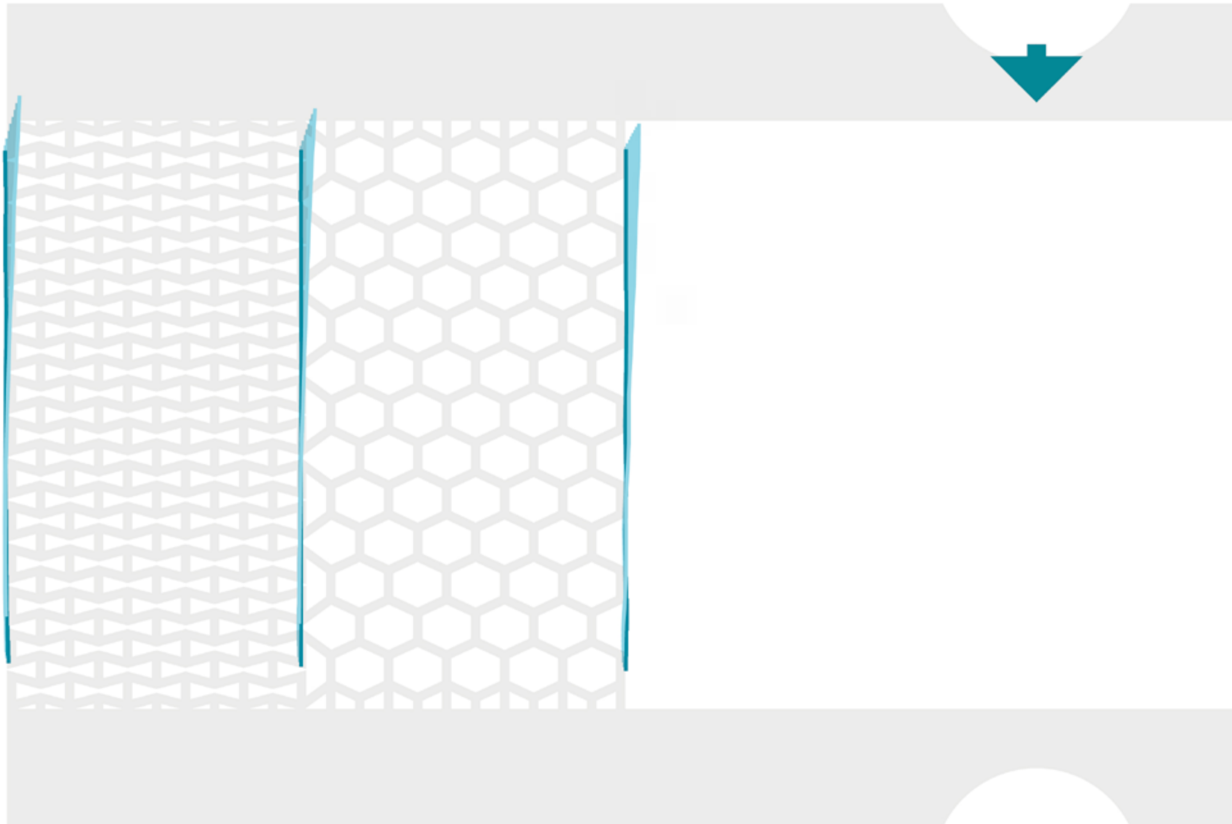

HYBRID TYPE 1
MASTER THESIS ELINE KOLKEN

Video A7: Deformation of the borders of Hybrid Type 1 through time - Press to play -

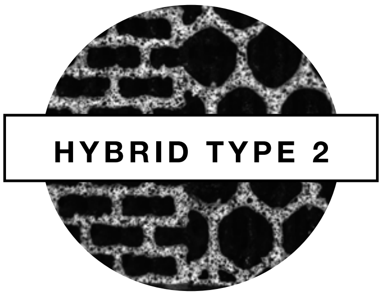
HYBRID TYPE 2

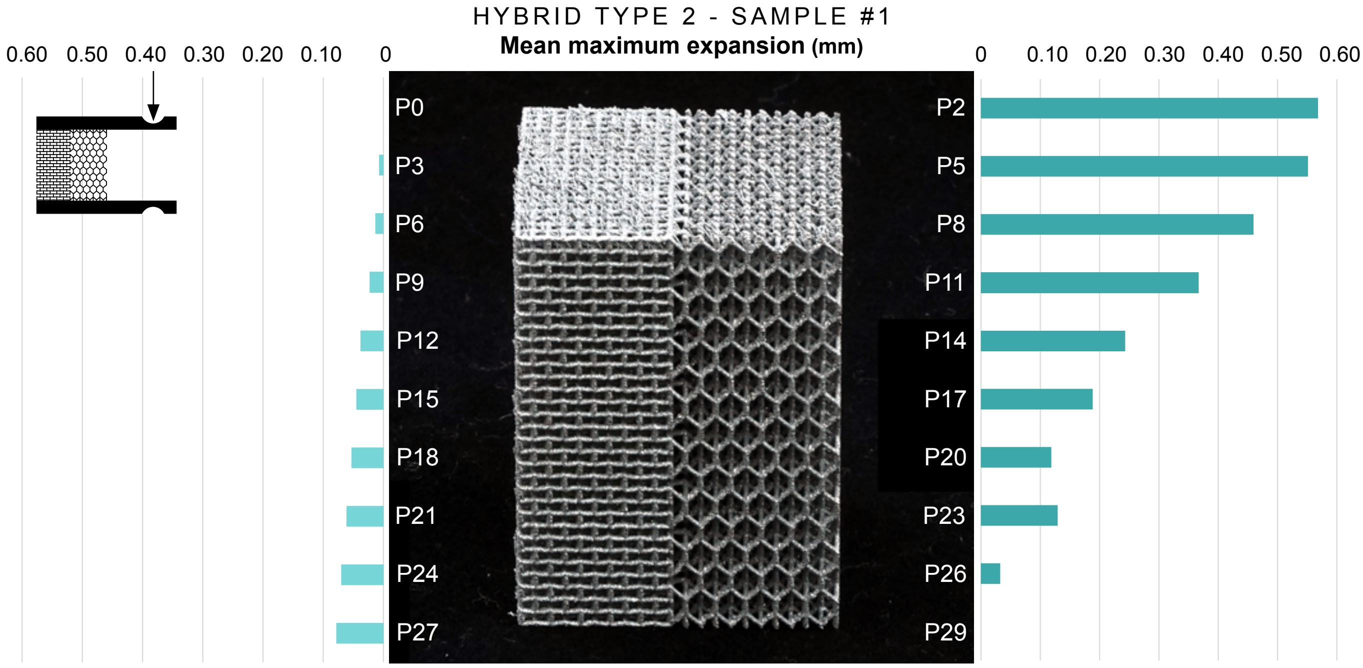
HYBRID TYPE 2 - SAMPLE #1
Mean maximum expansion (mm)
0.60 0.50 0.40 0.30 0.20 0.10 0
0 0.10 0.20 0.30 0.40 0.50 0.60
P0
P3
P6
P9
P12
P15
P18
P21
P24
P27
P2
P5
P8
P11
P14
P17
P20
P23
P26
P29

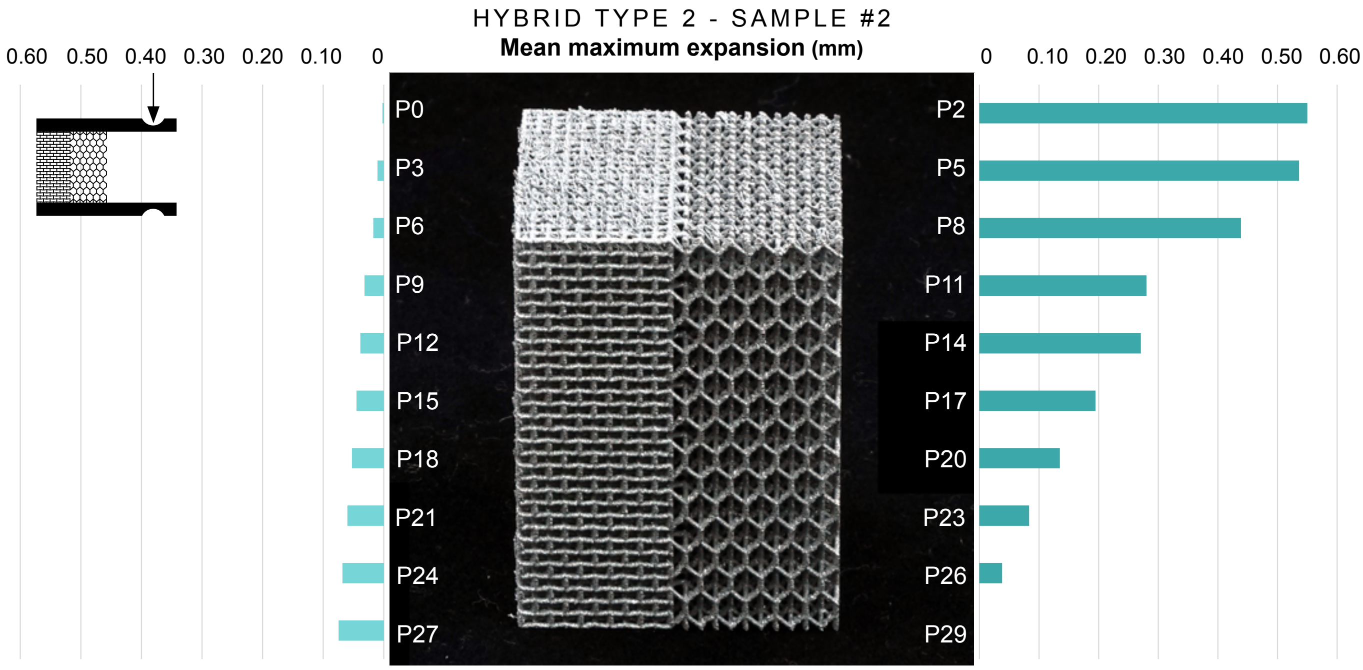
HYBRID TYPE 2 - SAMPLE #2
Mean maximum expansion (mm)
0.60 0.50 0.40 0.30 0.20 0.10 0
0 0.10 0.20 0.30 0.40 0.50 0.60
P0
P3
P6
P9
P12
P15
P18
P21
P24
P27
P2
P5
P8
P11
P14
P17
P20
P23
P26
P29

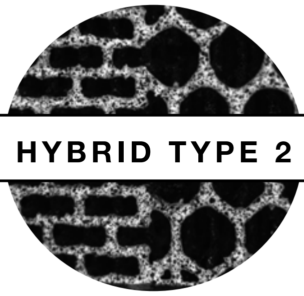

HYBRID TYPE 2

HYBRID TYPE 2 - SAMPLE #3

Mean maximum expansion (mm)

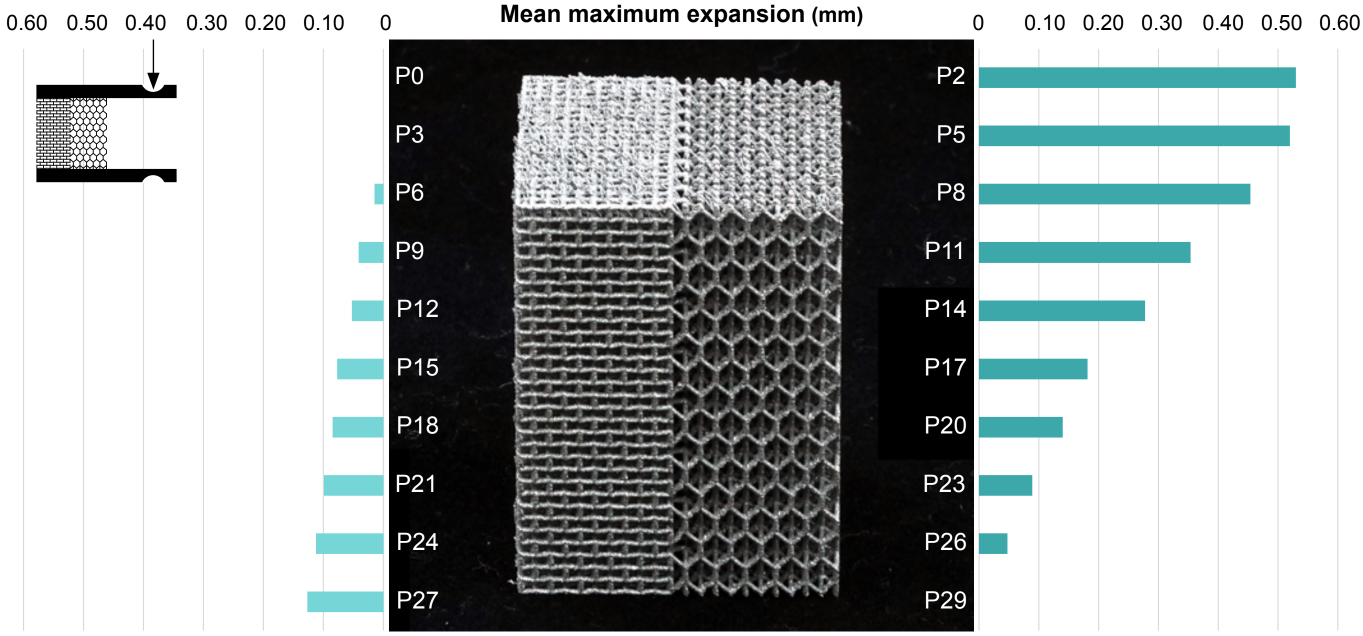

HYBRID TYPE 2 - SAMPLE #4

Mean maximum expansion (mm)

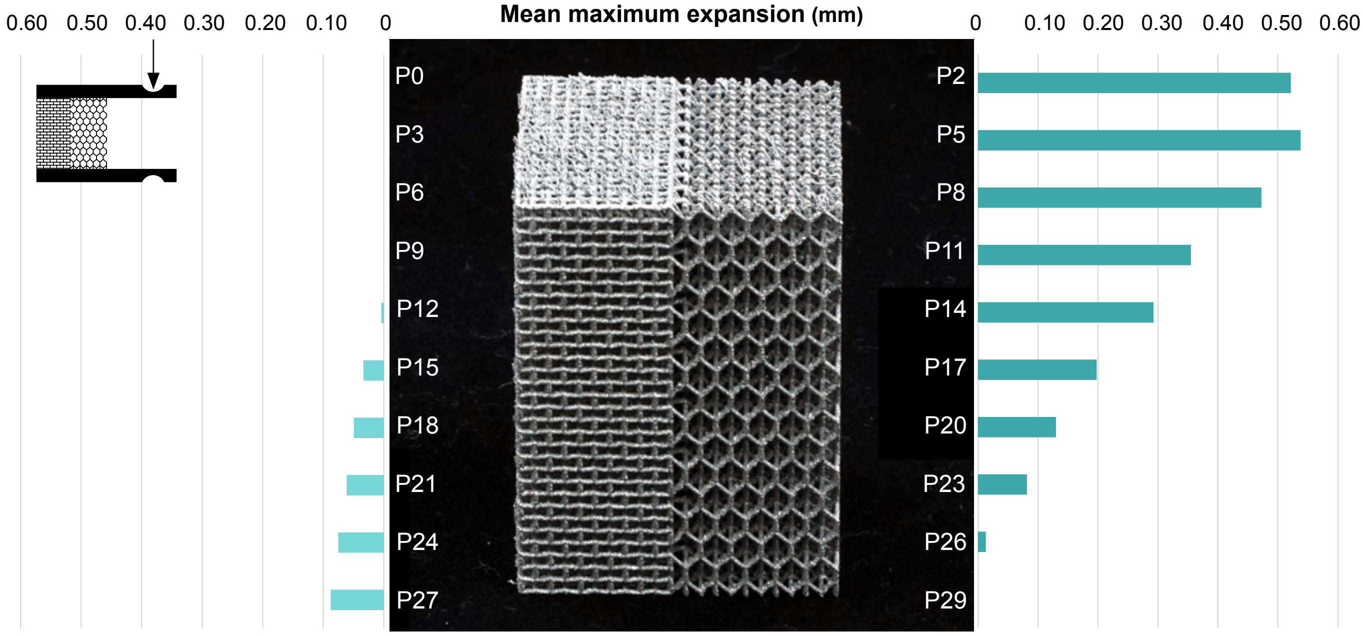

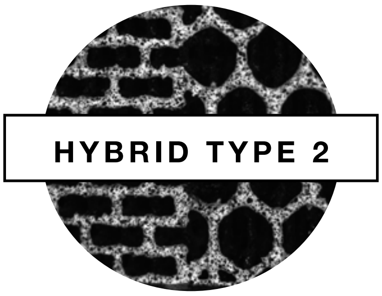

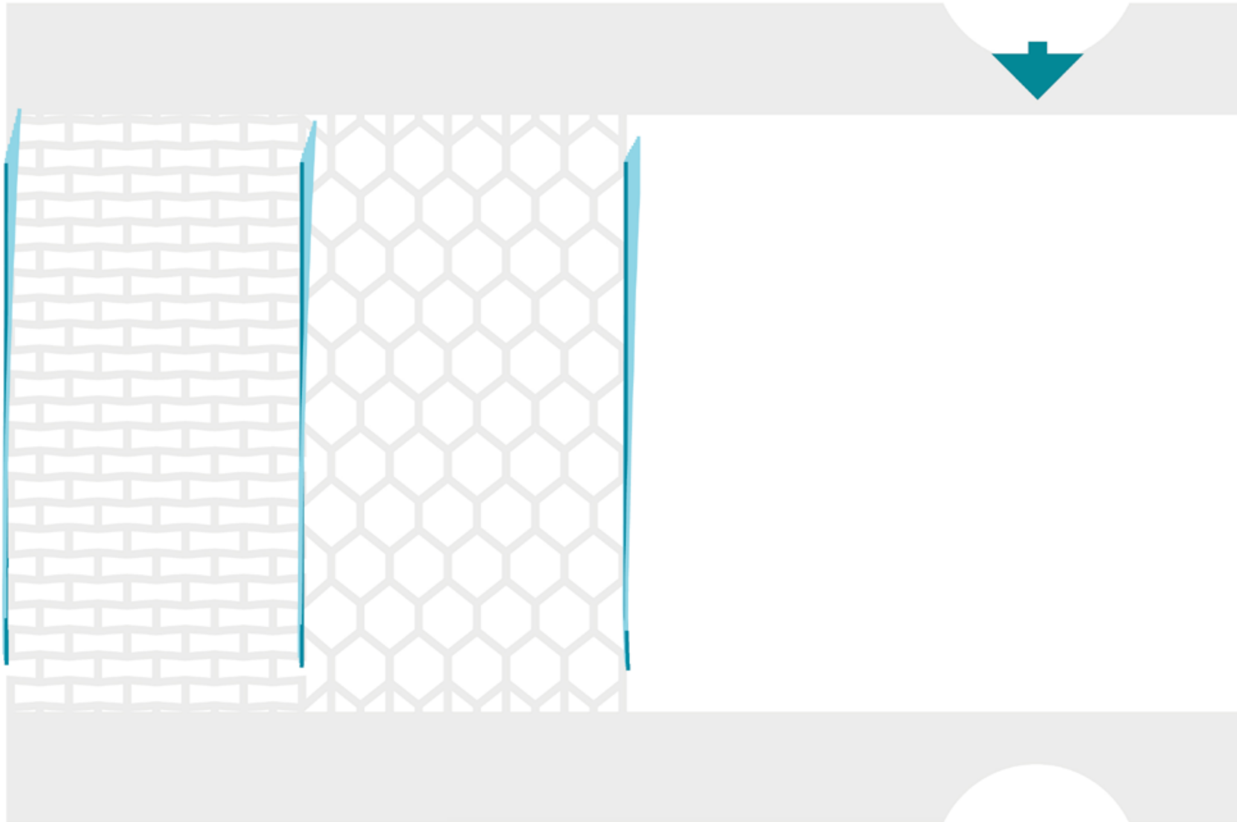

HYBRID TYPE 2
MASTER THESIS ELINE KOLKEN

Video A8: Deformation of the borders of Hybrid Type 2 through time - Press to play -

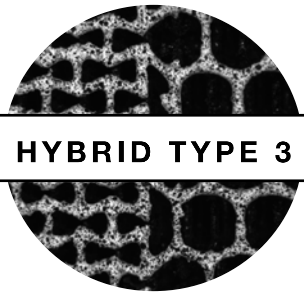

HYBRID TYPE 3

HYBRID TYPE 3 - SAMPLE #1

Mean maximum expansion (mm)

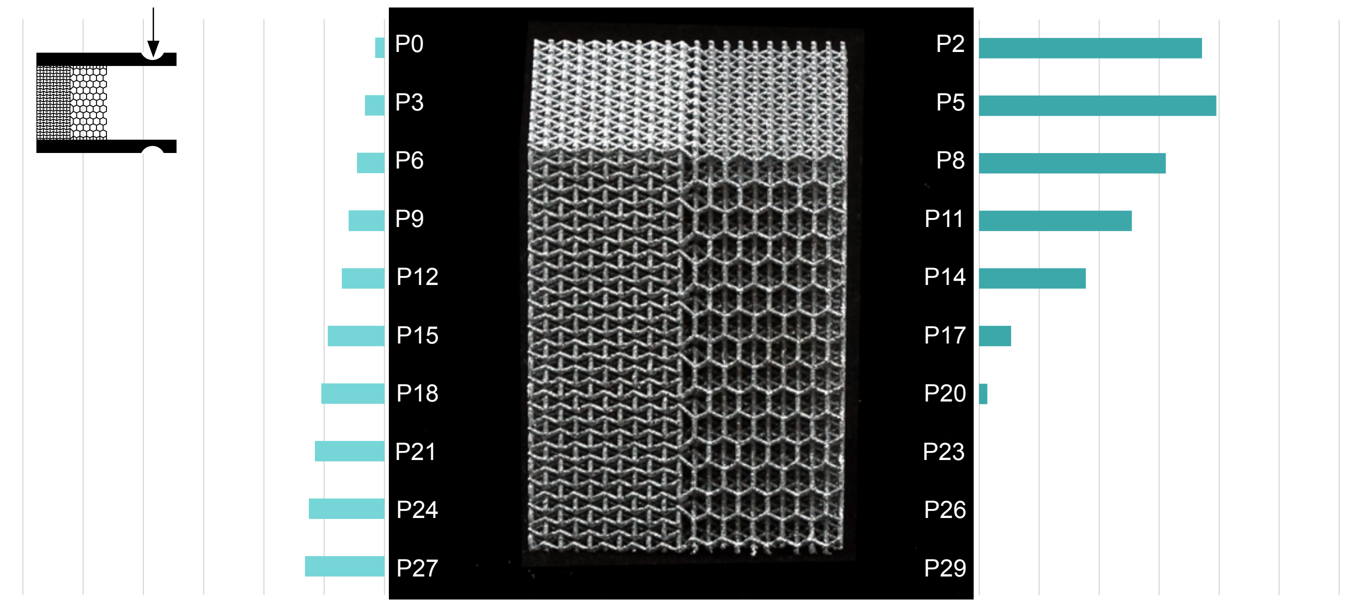

HYBRID TYPE 3 - SAMPLE #2

Mean maximum expansion (mm)

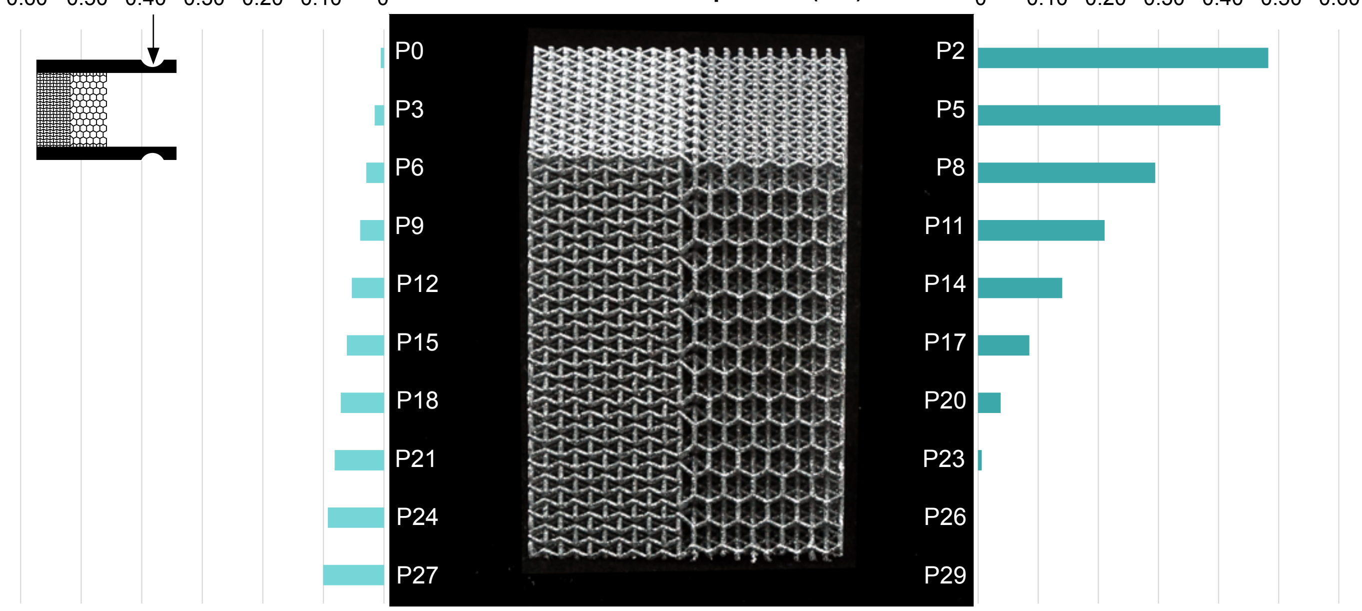

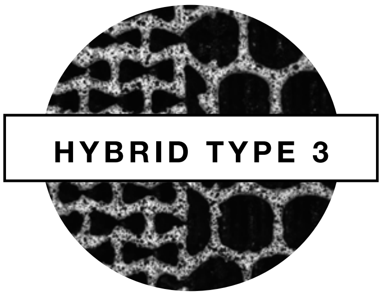

HYBRID TYPE 3 - SAMPLE #3

Mean maximum expansion (mm)

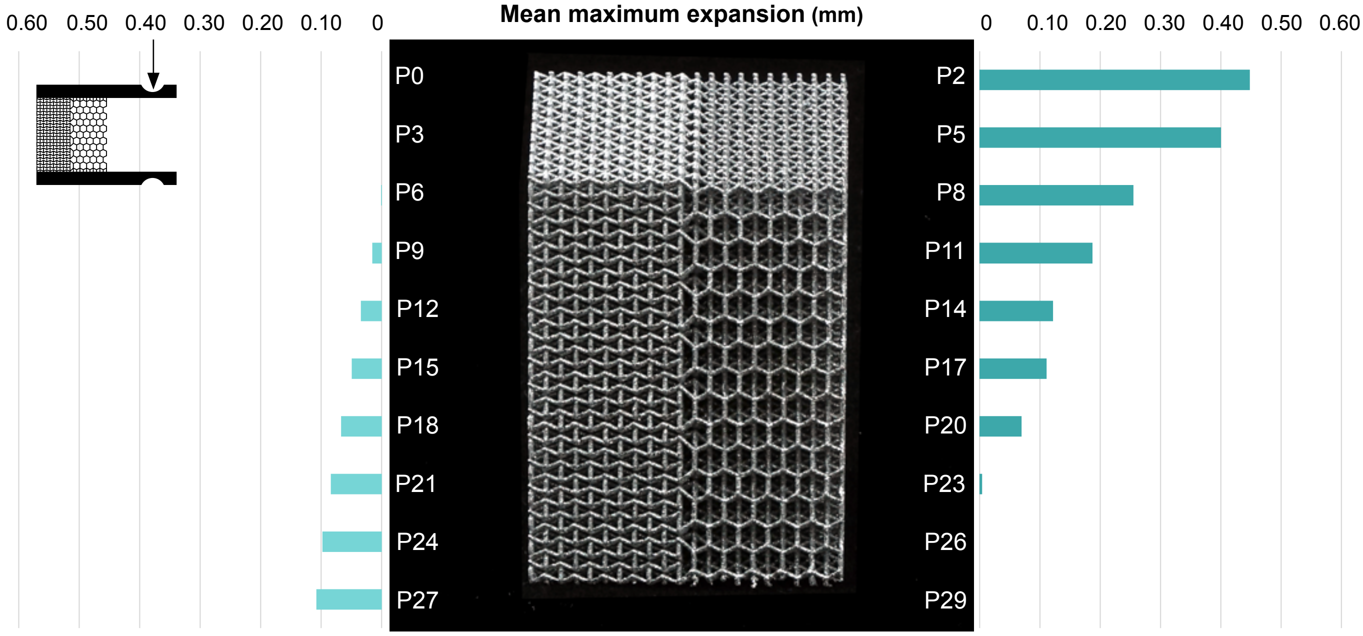

HYBRID TYPE 3 - SAMPLE #4

Mean maximum expansion (mm)

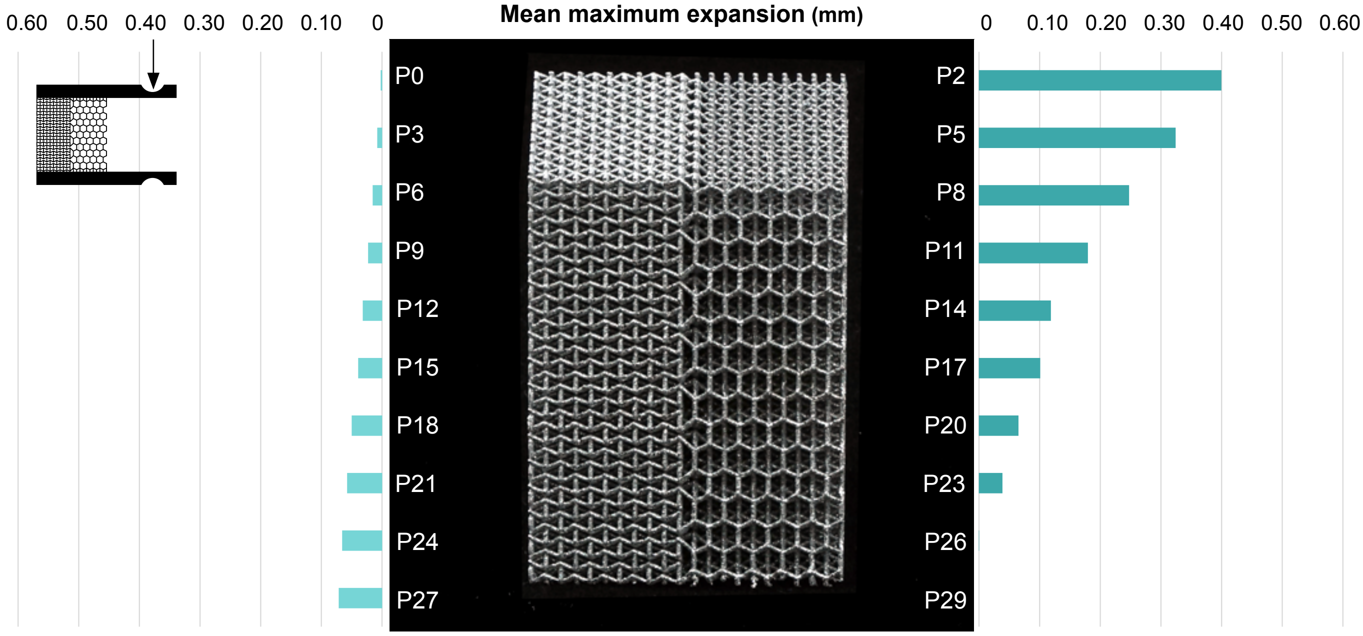

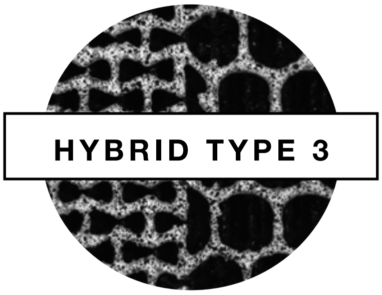

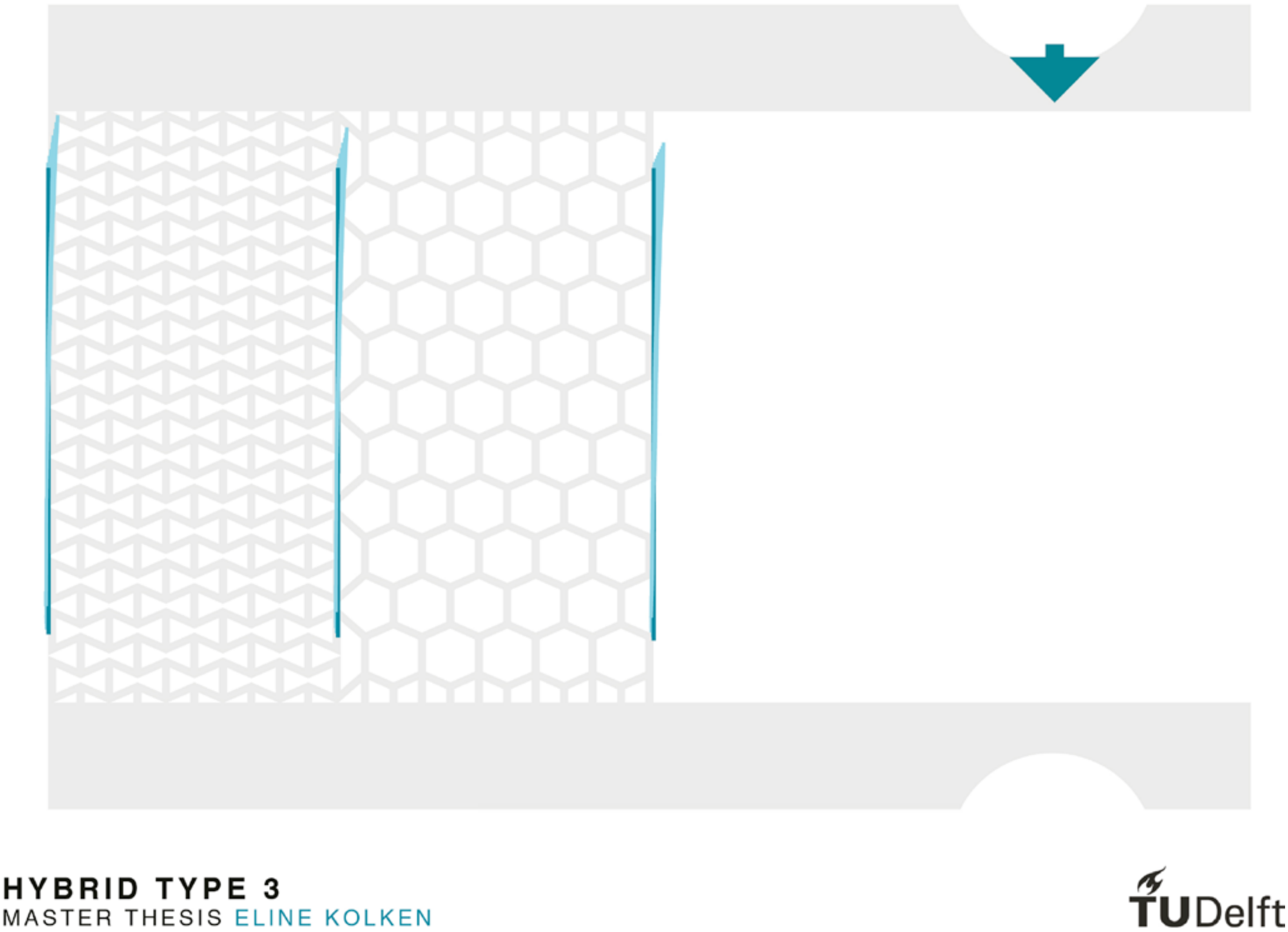

Video A9: Deformation of the borders of Hybrid Type 3 through time - Press to play -

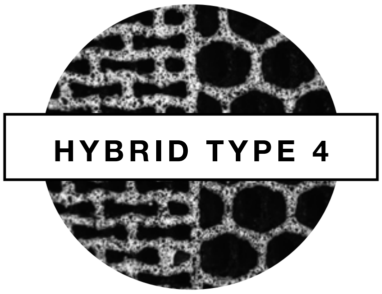
HYBRID TYPE 4

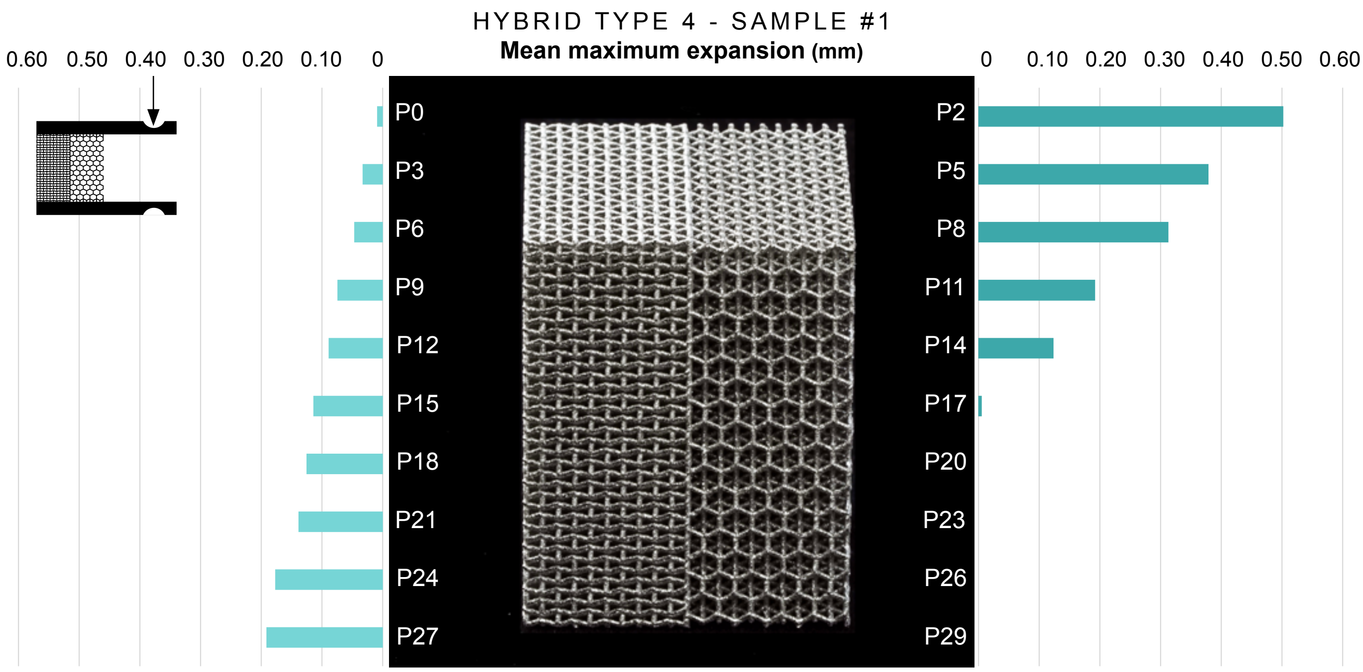
HYBRID TYPE 4 - SAMPLE #1
Mean maximum expansion (mm)
0.60 0.50 0.40 0.30 0.20 0.10 0
0 0.10 0.20 0.30 0.40 0.50 0.60
P0
P3
P6
P9
P12
P15
P18
P21
P24
P27
P2
P5
P8
P11
P14
P17
P20
P23
P26
P29

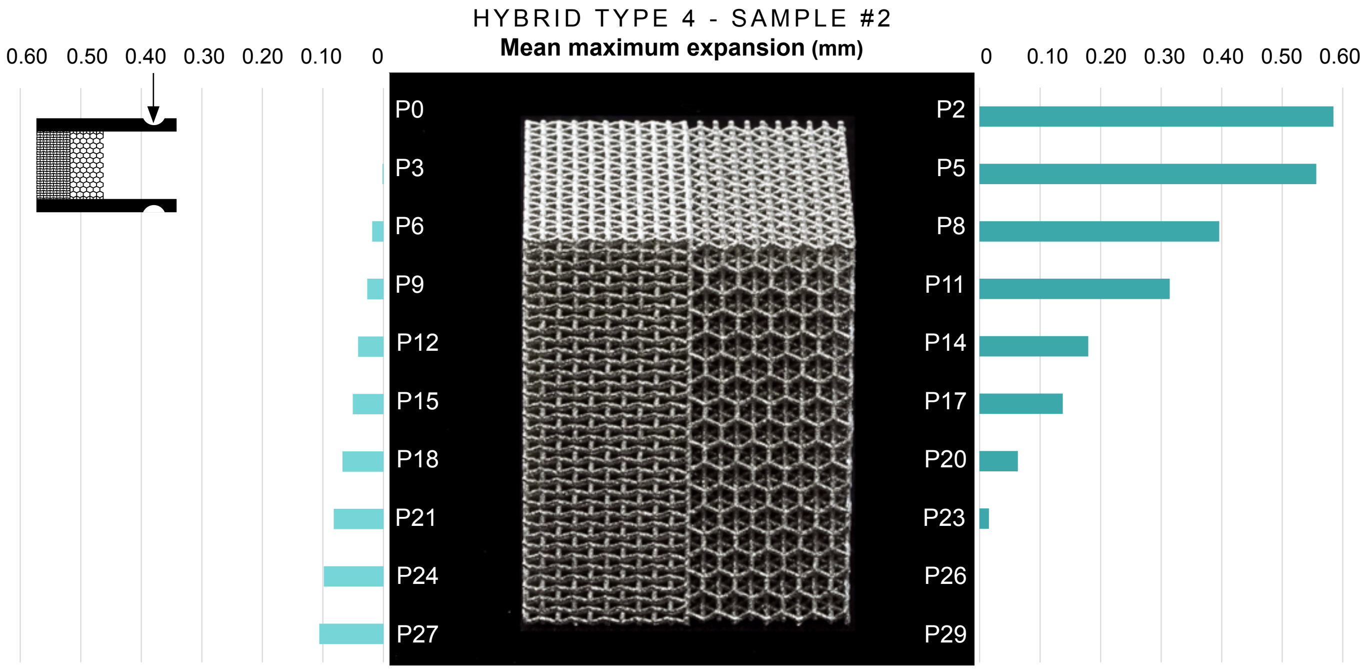
HYBRID TYPE 4 - SAMPLE #2
Mean maximum expansion (mm)
0.60 0.50 0.40 0.30 0.20 0.10 0
0 0.10 0.20 0.30 0.40 0.50 0.60
P0
P3
P6
P9
P12
P15
P18
P21
P24
P27
P2
P5
P8
P11
P14
P17
P20
P23
P26
P29

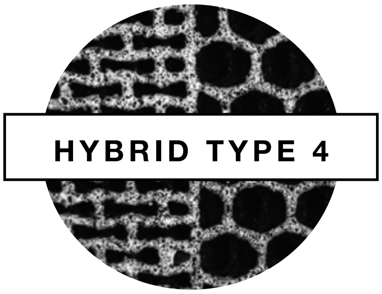

HYBRID TYPE 4

HYBRID TYPE 4 - SAMPLE #3

Mean maximum expansion (mm)

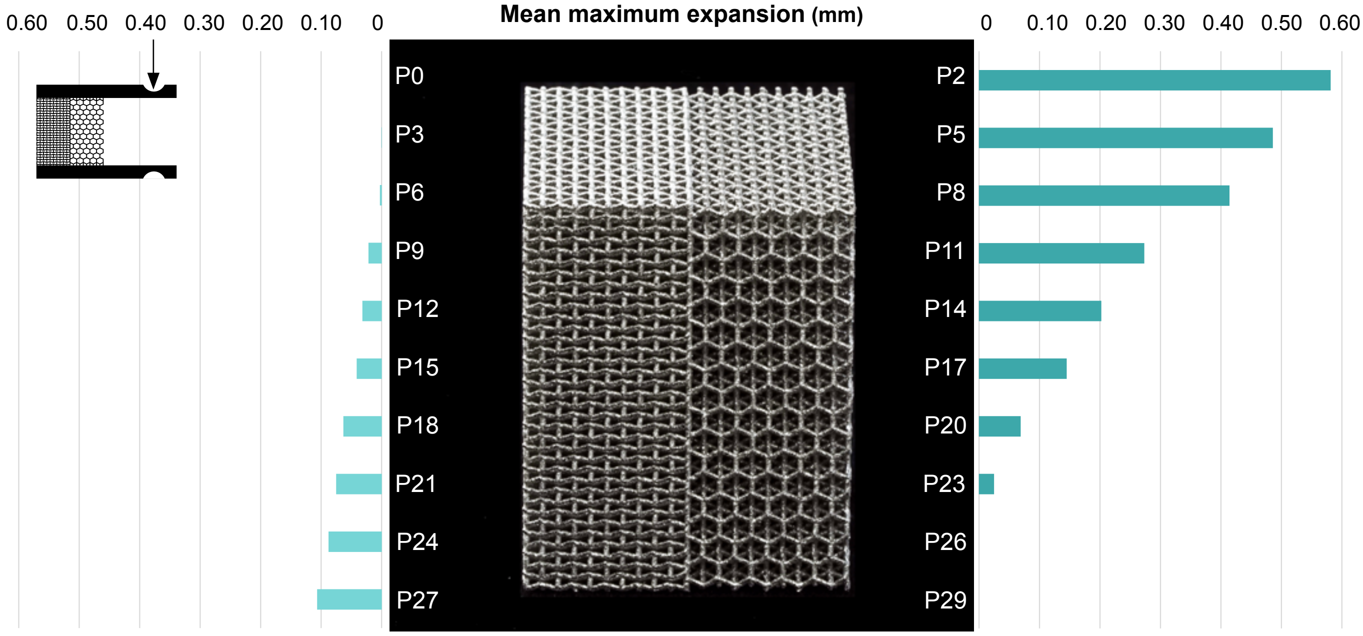

HYBRID TYPE 4 - SAMPLE #4

Mean maximum expansion (mm)

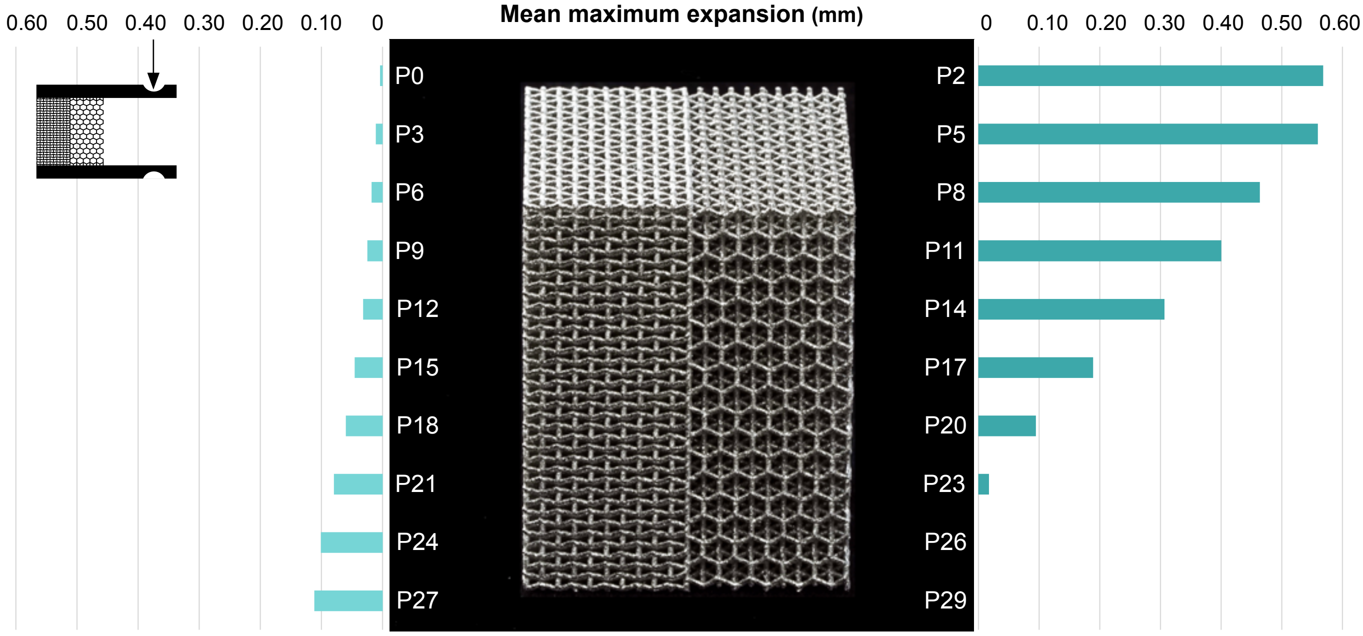

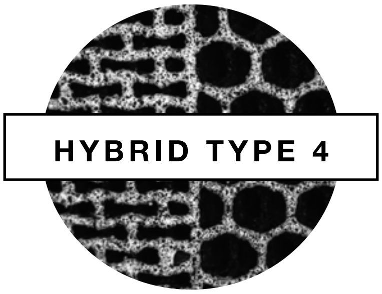

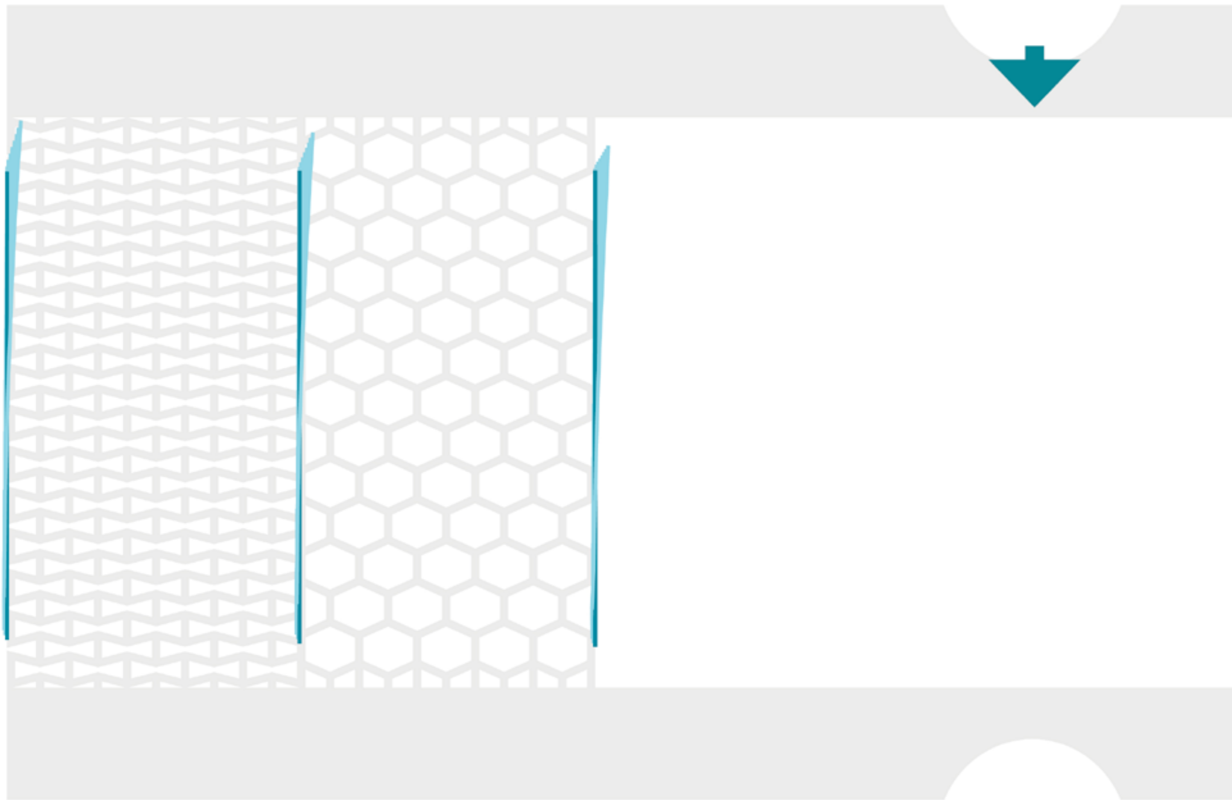

HYBRID TYPE 4
MASTER THESIS ELINE KOLKEN

Video A10: Deformation of the borders of Hybrid Type 4 through time - Press to play -

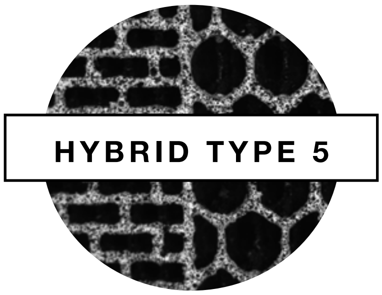

HYBRID TYPE 5 - SAMPLE #1
Mean maximum expansion (mm)

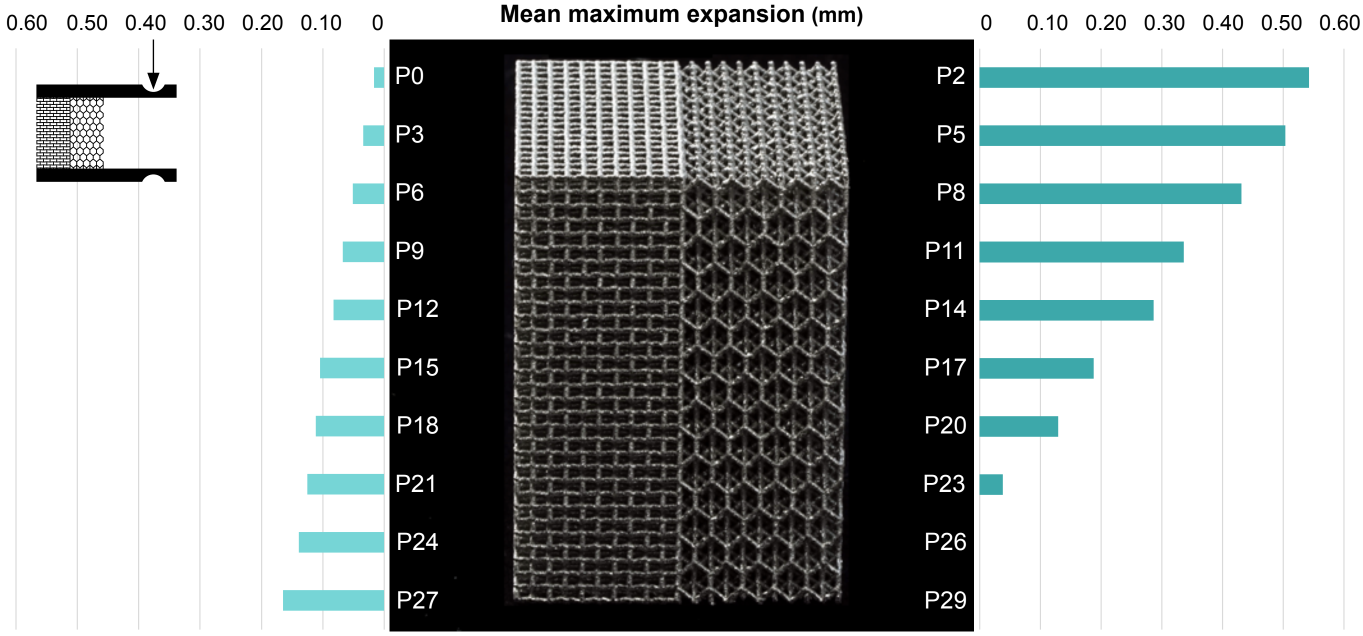

HYBRID TYPE 5 - SAMPLE #2
Mean maximum expansion (mm)

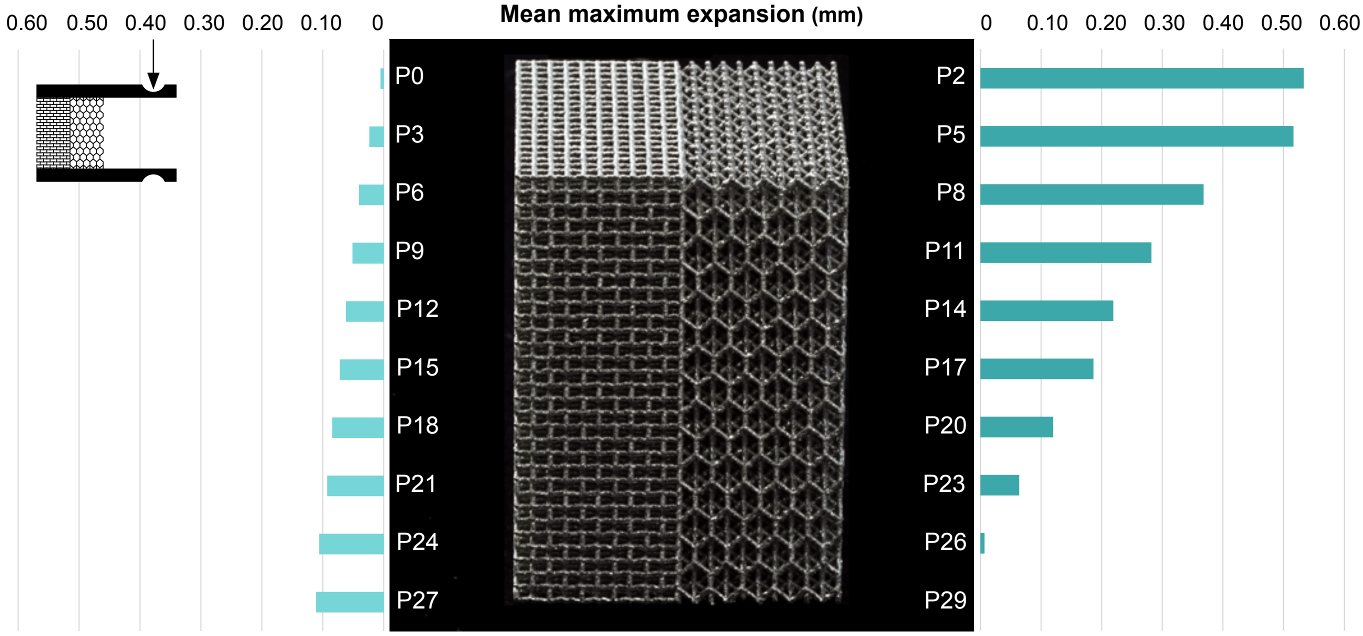

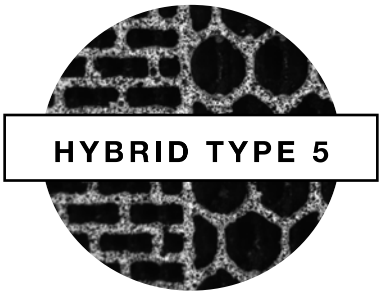
HYBRID TYPE 5

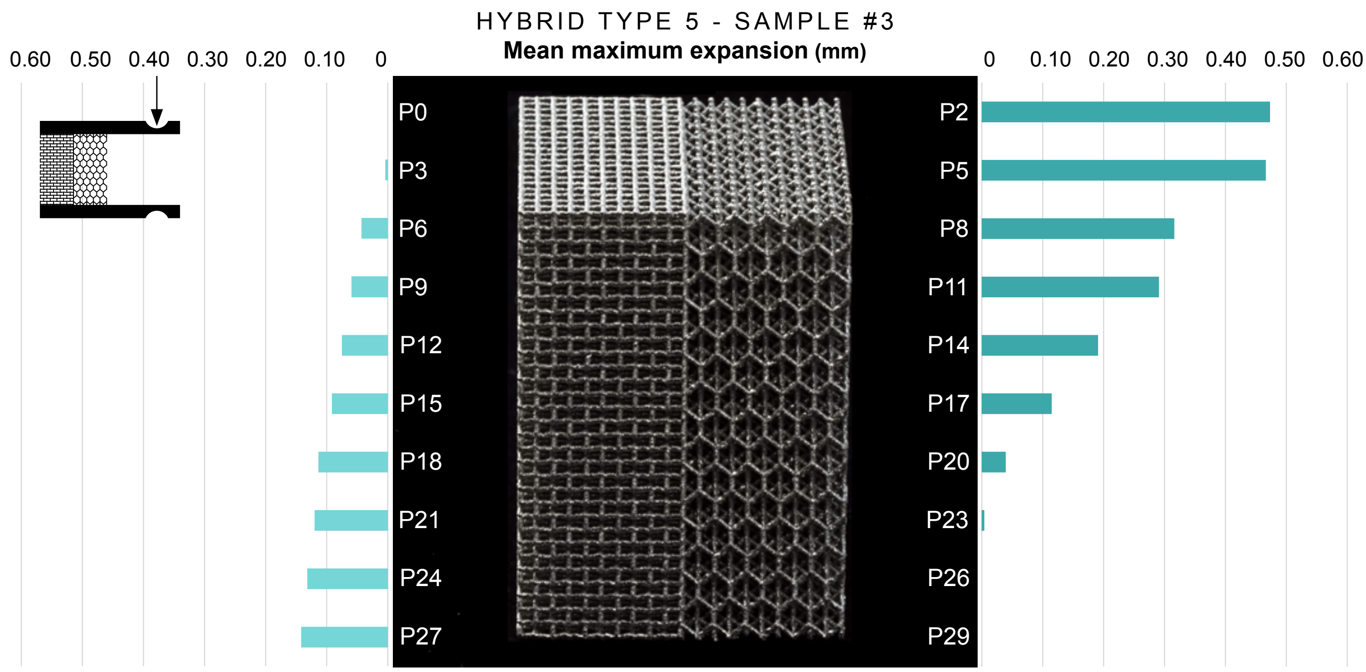
HYBRID TYPE 5 - SAMPLE #3
Mean maximum expansion (mm)
0.60 0.50 0.40 0.30 0.20 0.10 0
0 0.10 0.20 0.30 0.40 0.50 0.60
P0
P3
P6
P9
P12
P15
P18
P21
P24
P27
P2
P5
P8
P11
P14
P17
P20
P23
P26
P29

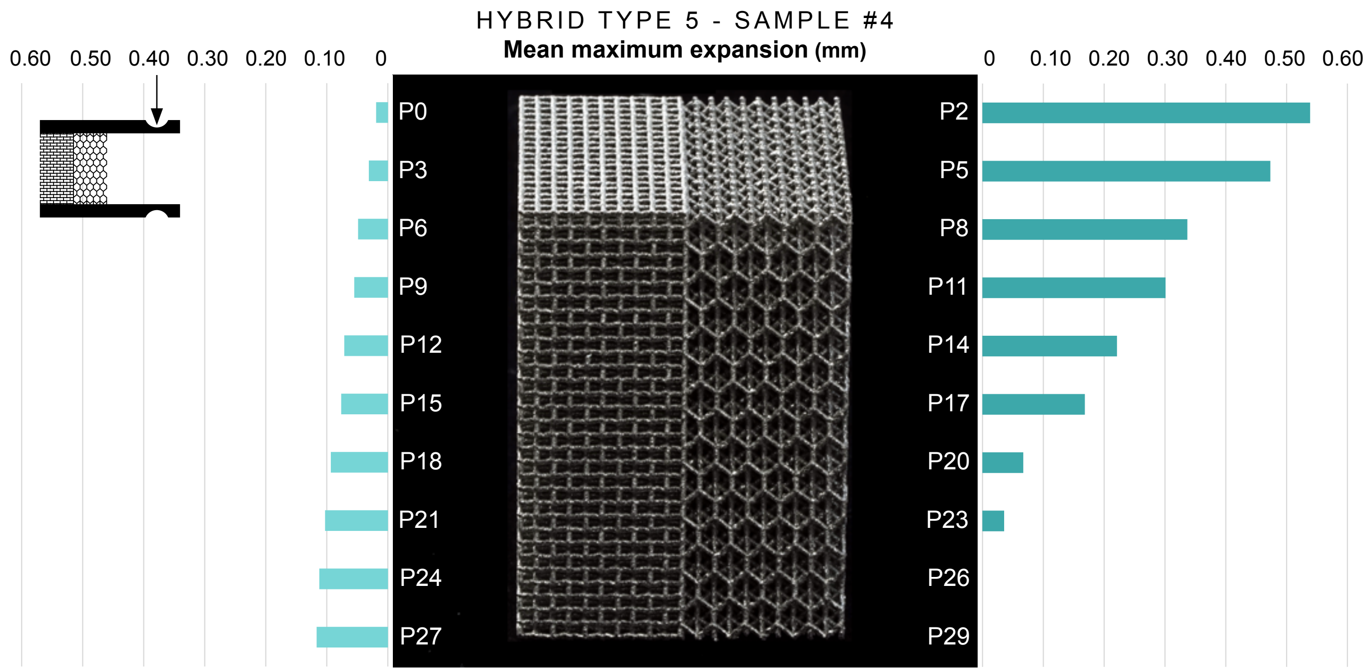
HYBRID TYPE 5 - SAMPLE #4
Mean maximum expansion (mm)
0.60 0.50 0.40 0.30 0.20 0.10 0
0 0.10 0.20 0.30 0.40 0.50 0.60
P0
P3
P6
P9
P12
P15
P18
P21
P24
P27
P2
P5
P8
P11
P14
P17
P20
P23
P26
P29

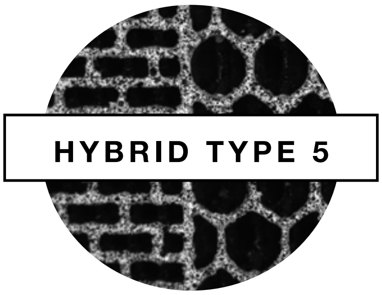

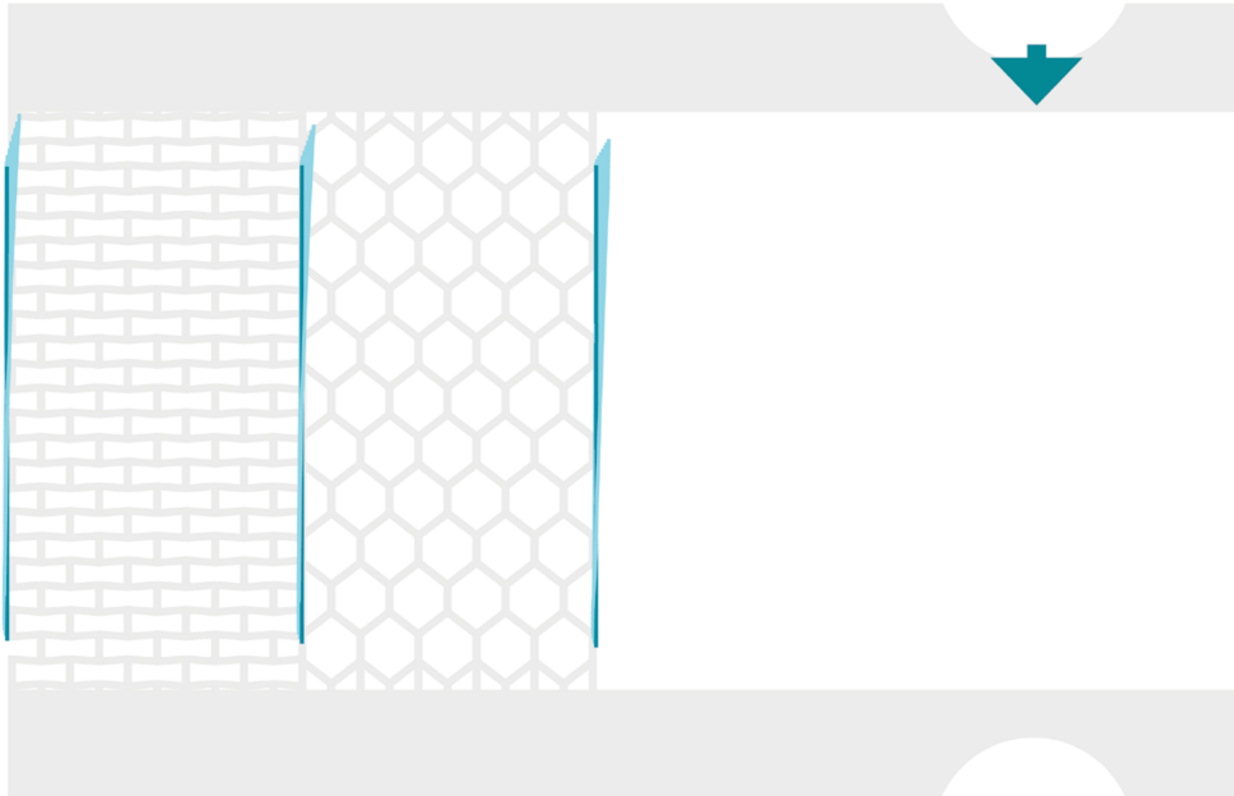

Video A11: Deformation of the borders of Hybrid Type 5 through time - Press to play -

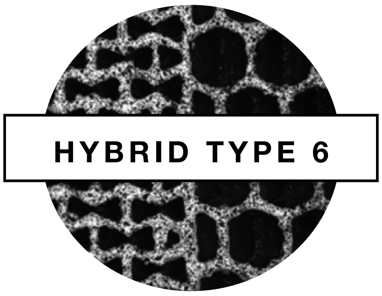
HYBRID TYPE 6

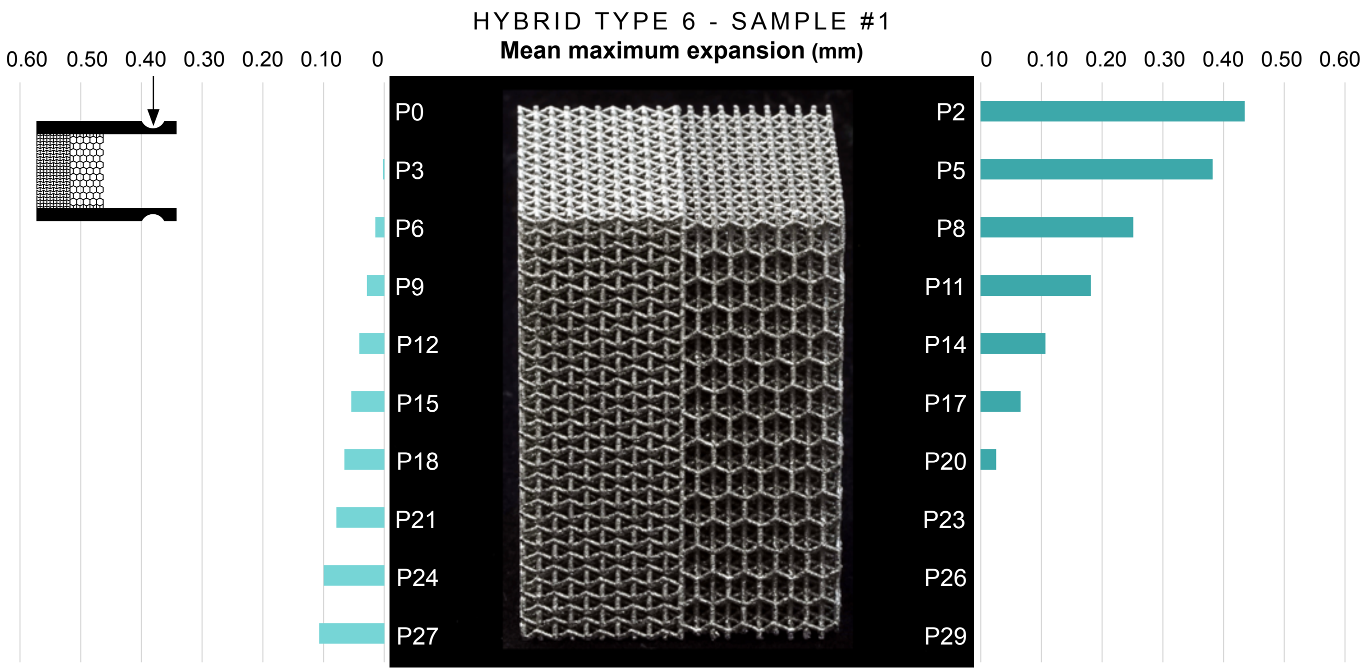
HYBRID TYPE 6 - SAMPLE #1
Mean maximum expansion (mm)
0.60 0.50 0.40 0.30 0.20 0.10 0
0 0.10 0.20 0.30 0.40 0.50 0.60
P0
P3
P6
P9
P12
P15
P18
P21
P24
P27
P2
P5
P8
P11
P14
P17
P20
P23
P26
P29

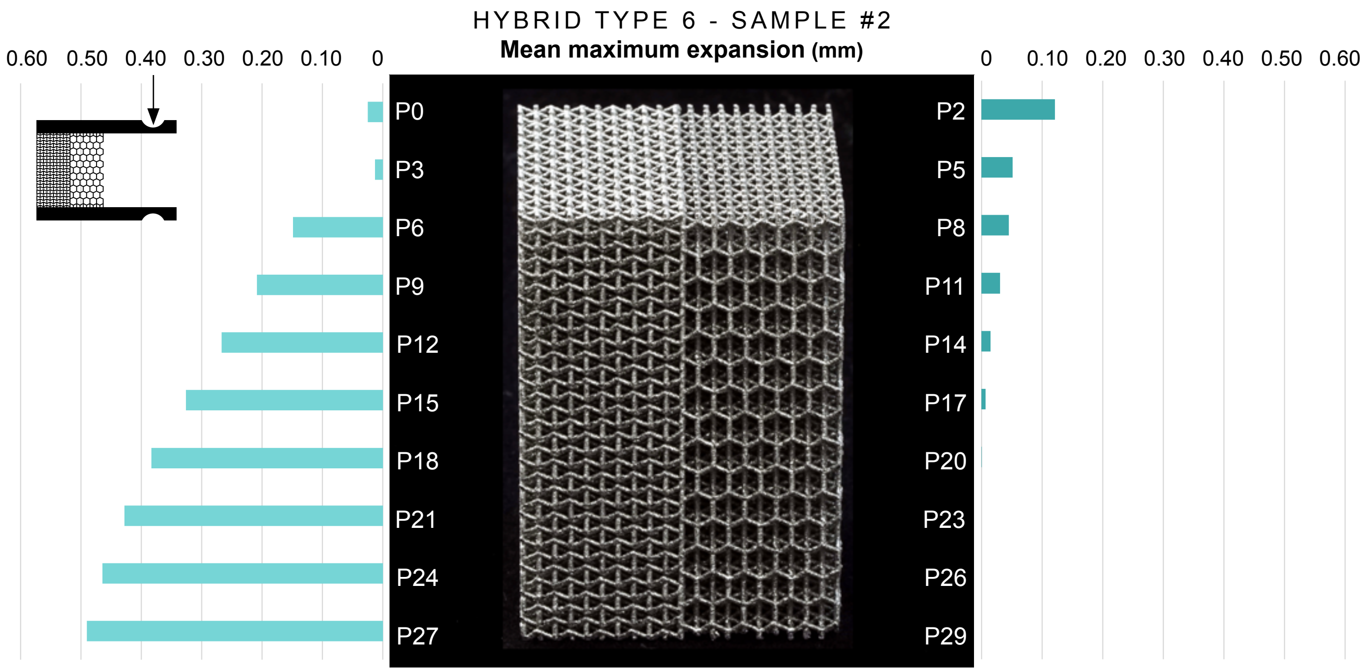
HYBRID TYPE 6 - SAMPLE #2
Mean maximum expansion (mm)
0.60 0.50 0.40 0.30 0.20 0.10 0
0 0.10 0.20 0.30 0.40 0.50 0.60
P0
P3
P6
P9
P12
P15
P18
P21
P24
P27
P2
P5
P8
P11
P14
P17
P20
P23
P26
P29

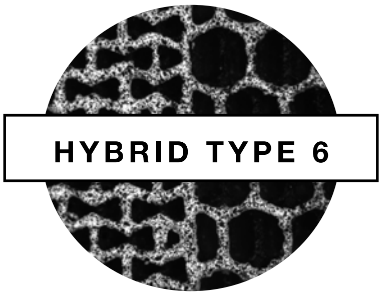

HYBRID TYPE 6

HYBRID TYPE 6 - SAMPLE #3

Mean maximum expansion (mm)

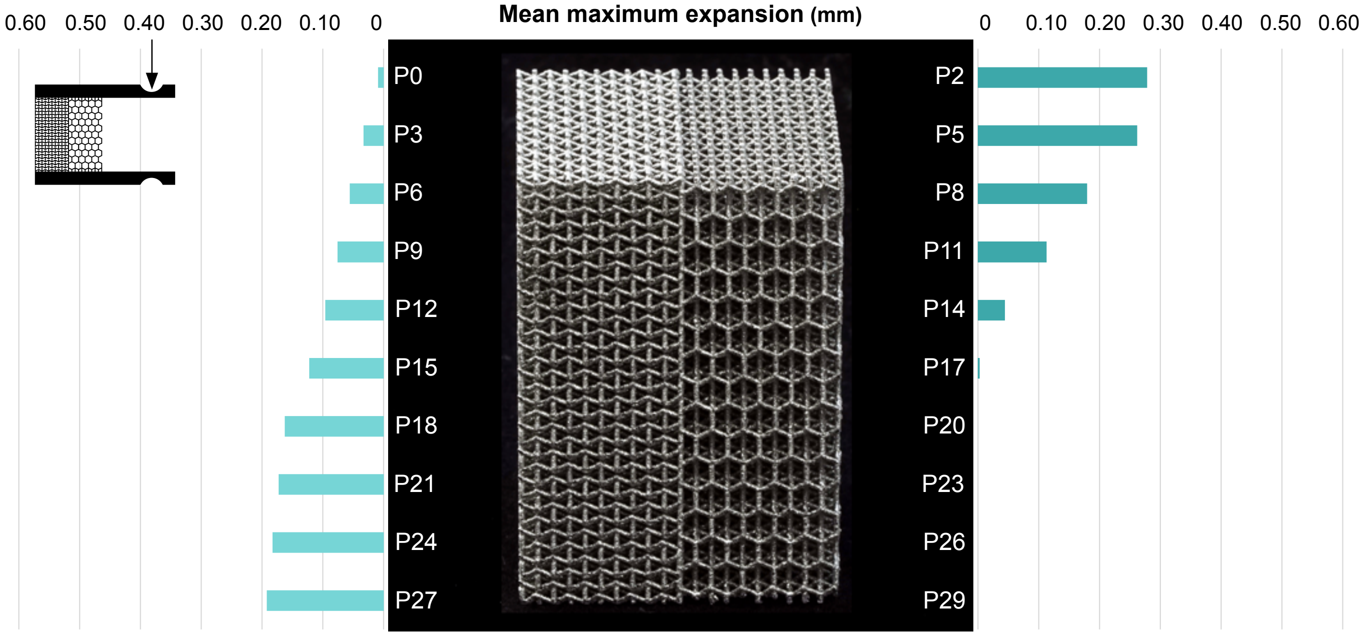

HYBRID TYPE 6 - SAMPLE #4

Mean maximum expansion (mm)

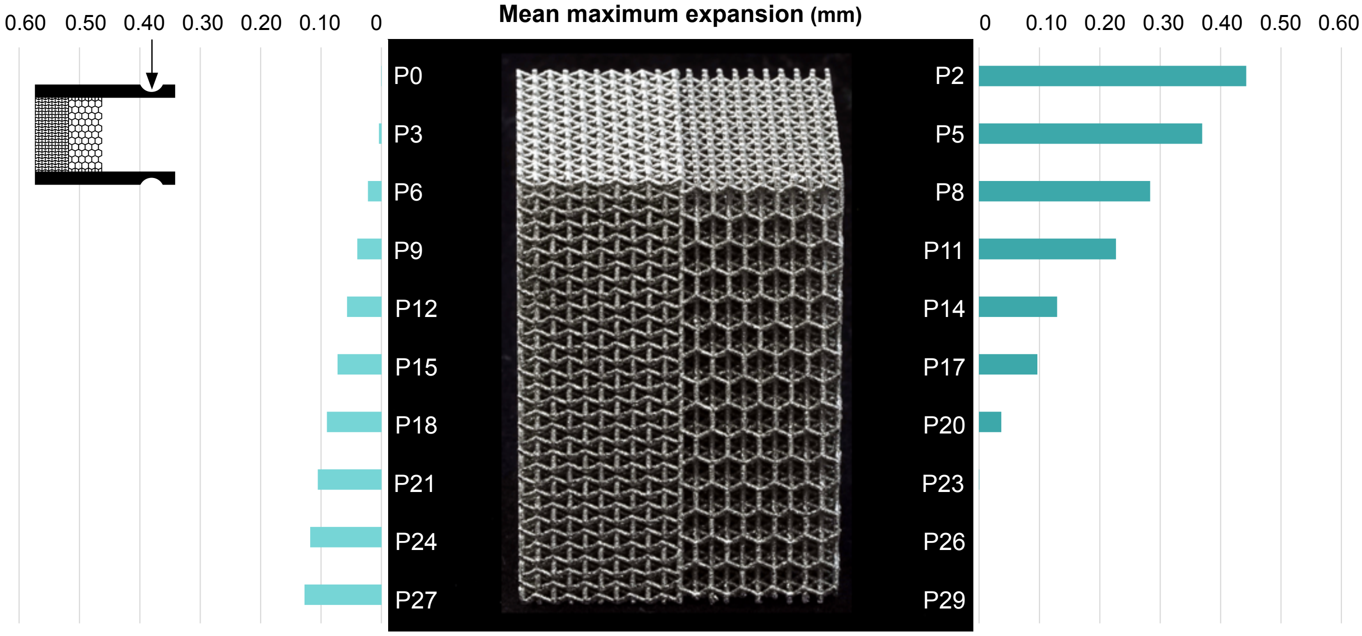

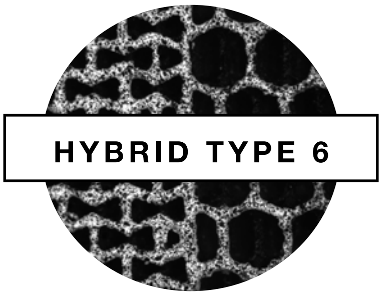

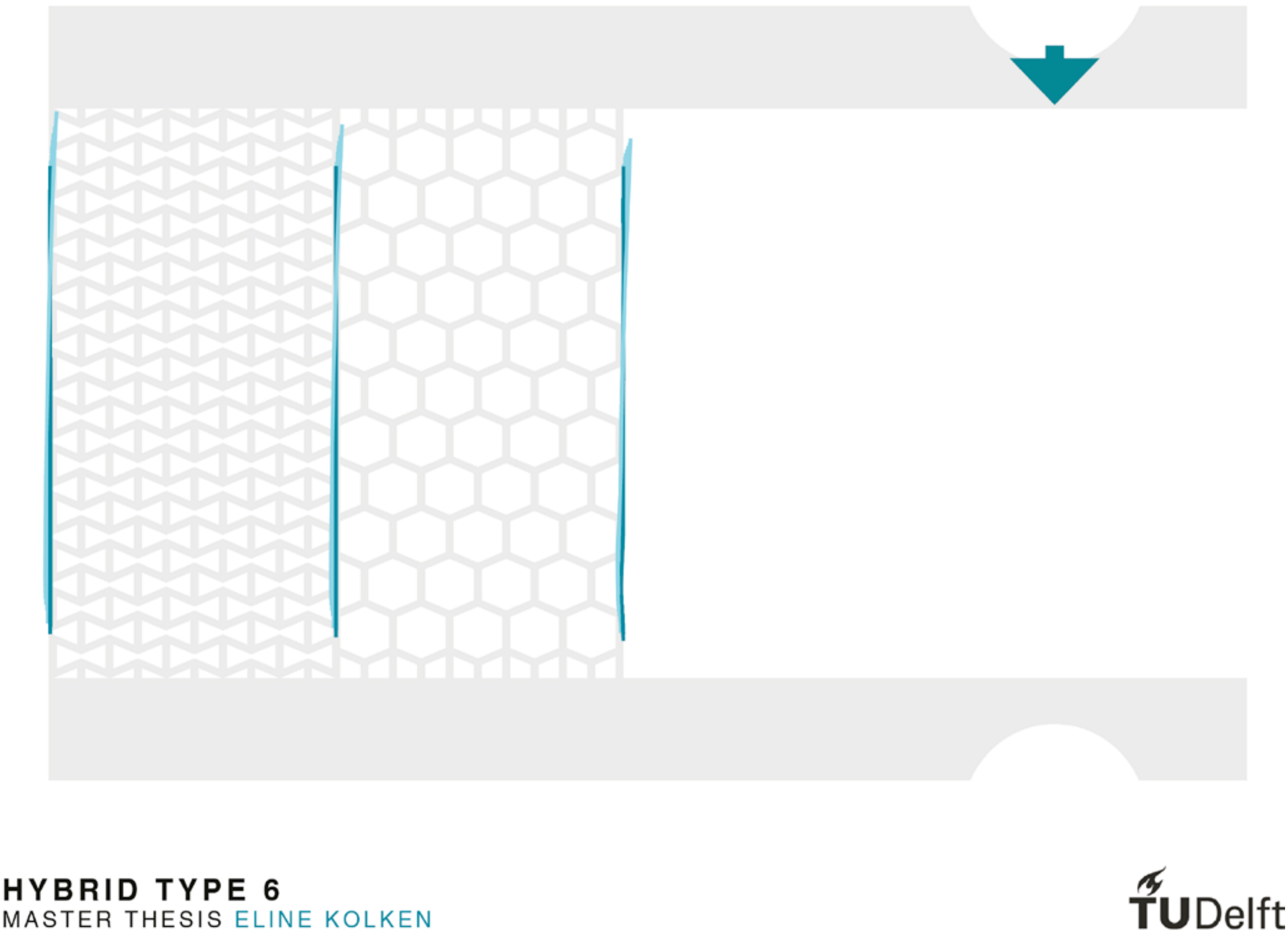

Video A12: Deformation of the borders of Hybrid Type 6 through time - Press to play -

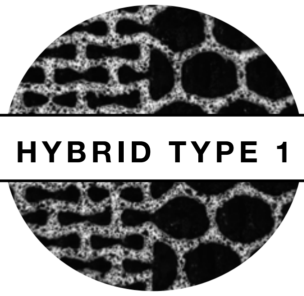

HYBRID TYPE 1

HYBRID TYPE 1 - SAMPLE #1 HYBRID TYPE 1 - SAMPLE #2

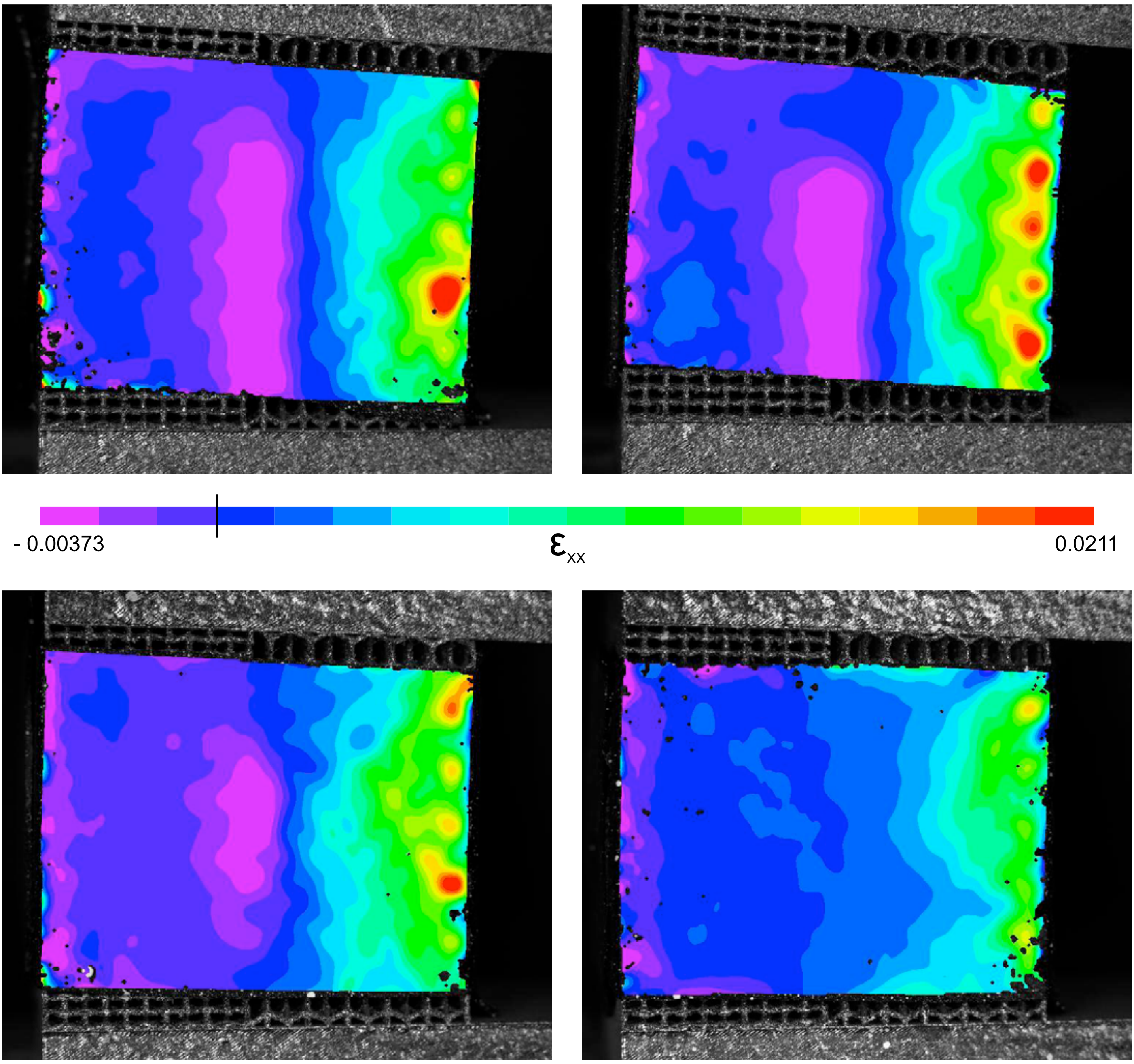

HYBRID TYPE 1 - SAMPLE #3 HYBRID TYPE 1 - SAMPLE #4

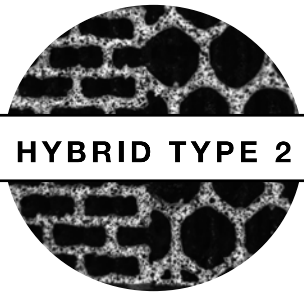

HYBRID TYPE 2

HYBRID TYPE 2 - SAMPLE #1

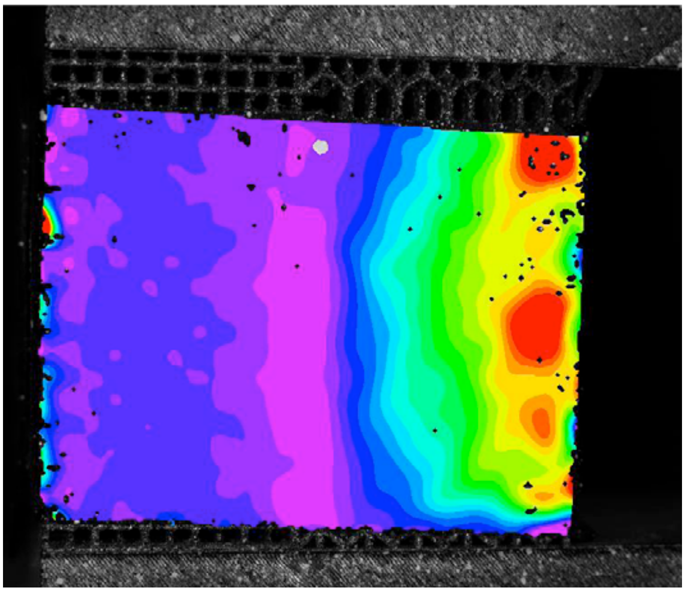

HYBRID TYPE 2 - SAMPLE #2

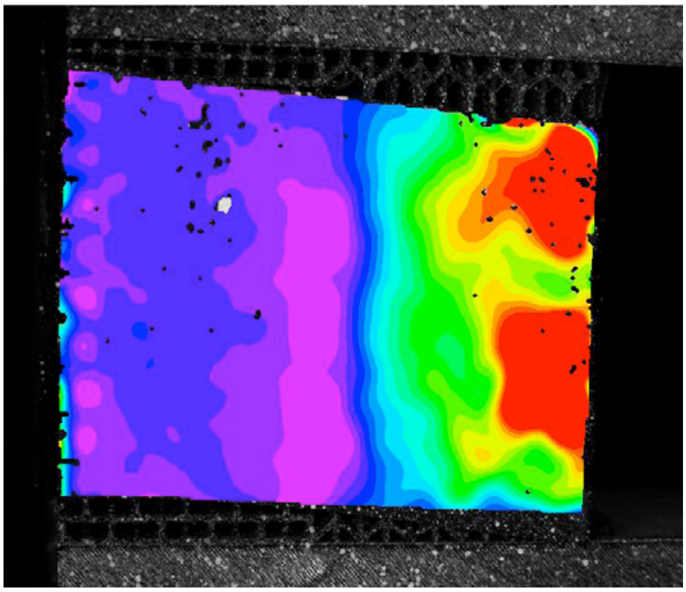

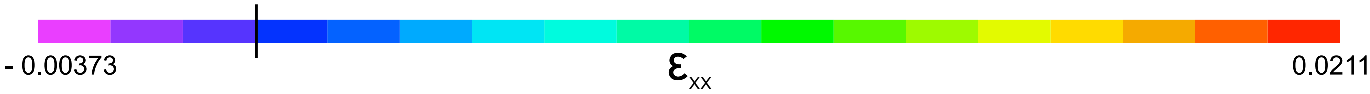

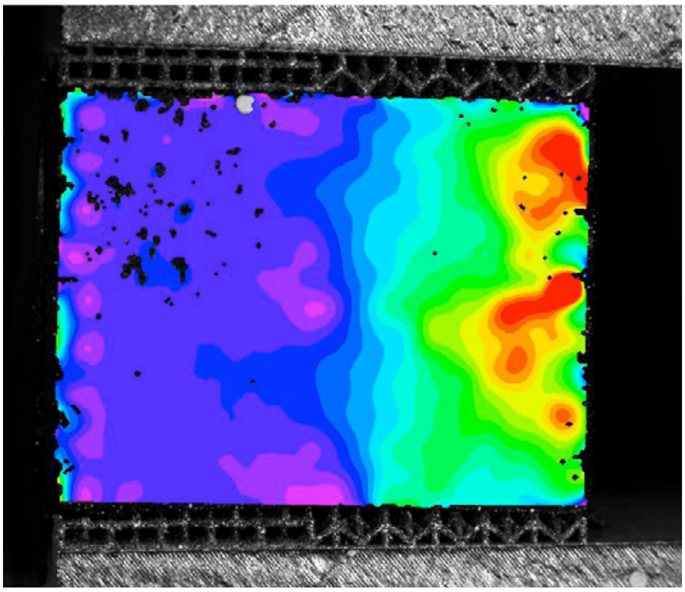

HYBRID TYPE 2 - SAMPLE #3

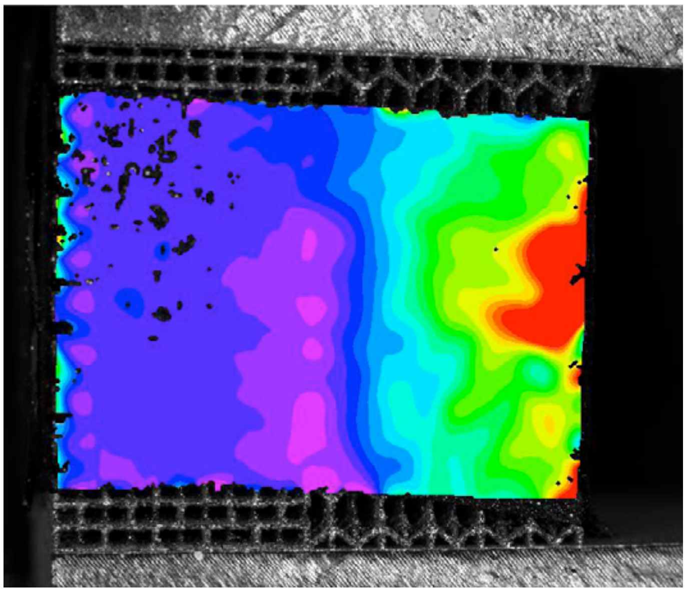

HYBRID TYPE 2 - SAMPLE #4

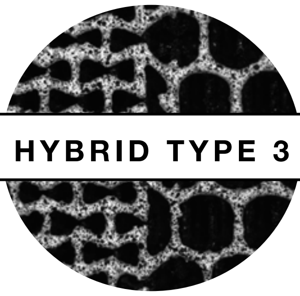

HYBRID TYPE 3

HYBRID TYPE 3 - SAMPLE #1

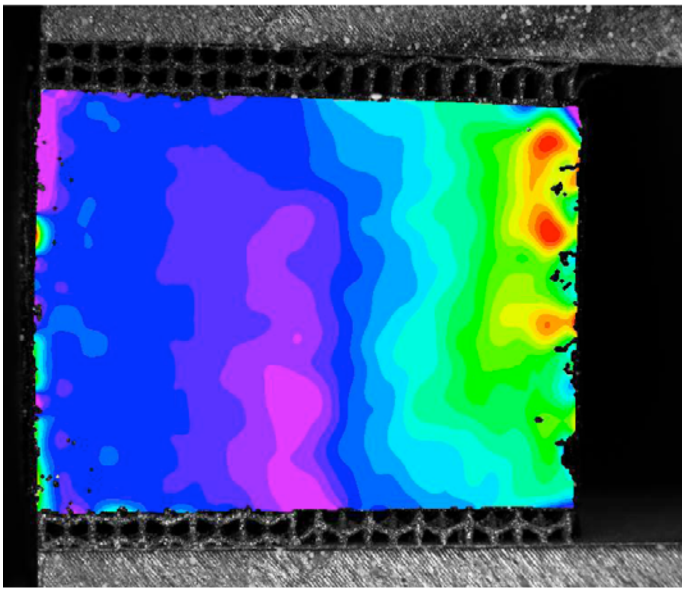

HYBRID TYPE 3 - SAMPLE #2

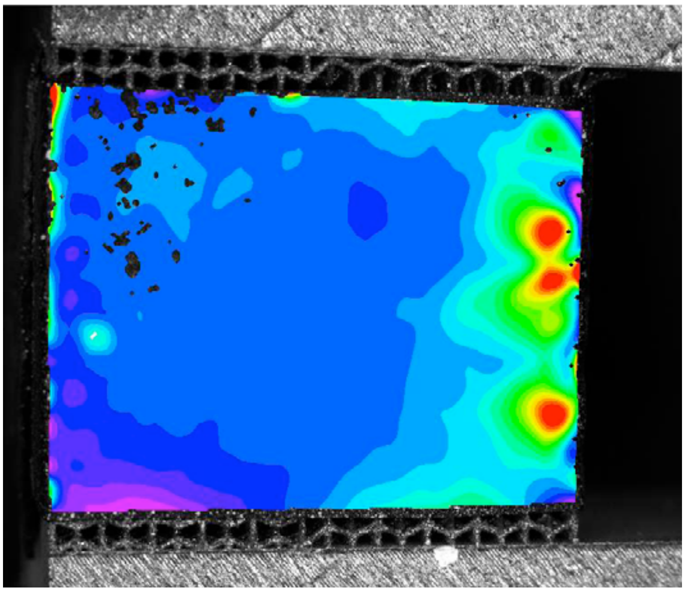

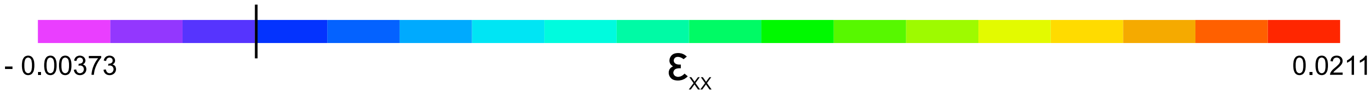

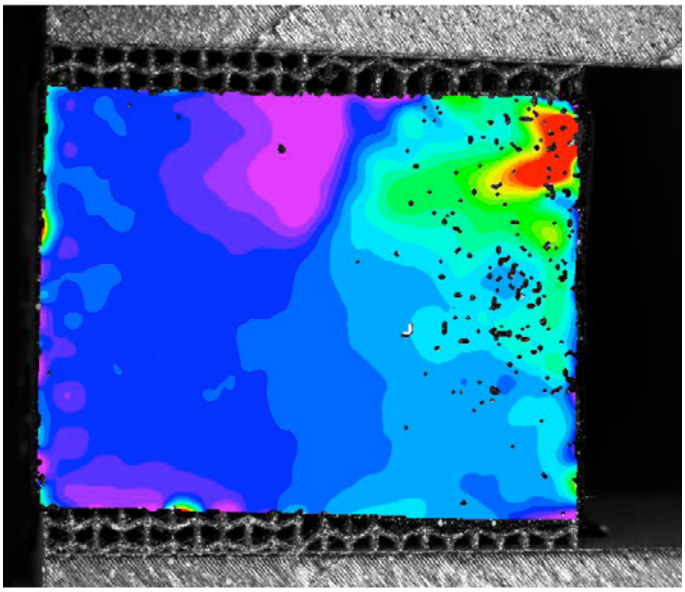

HYBRID TYPE 3 - SAMPLE #3

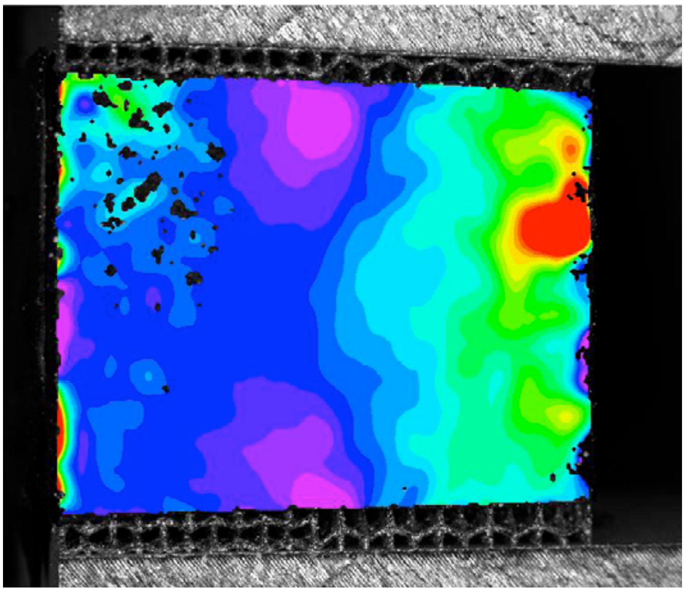

HYBRID TYPE 3 - SAMPLE #4

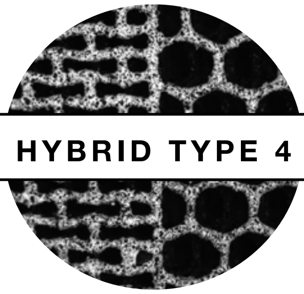

HYBRID TYPE 4

HYBRID TYPE 4 - SAMPLE #1

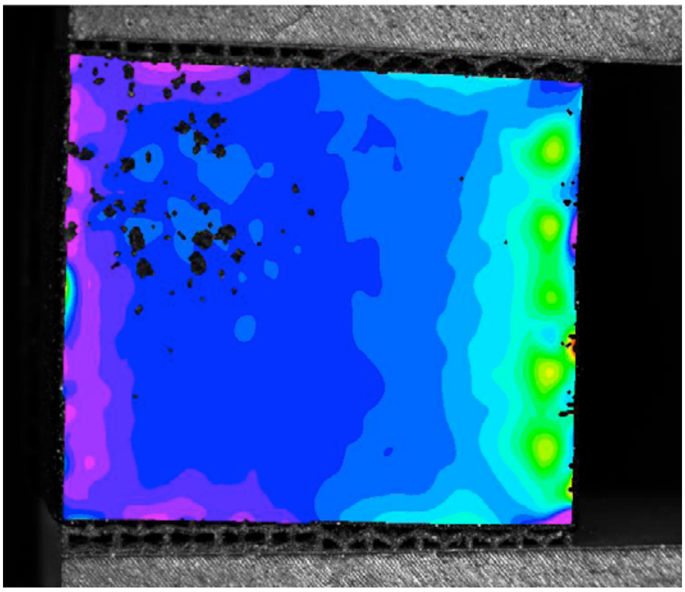

HYBRID TYPE 4 - SAMPLE #2

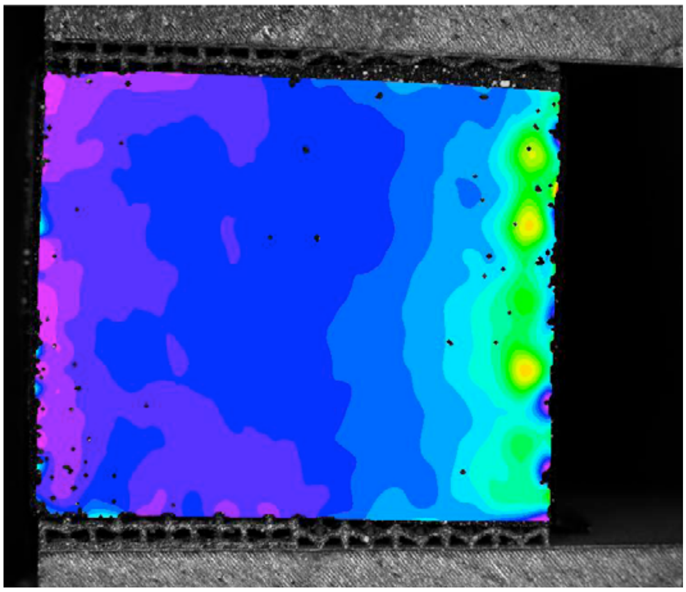

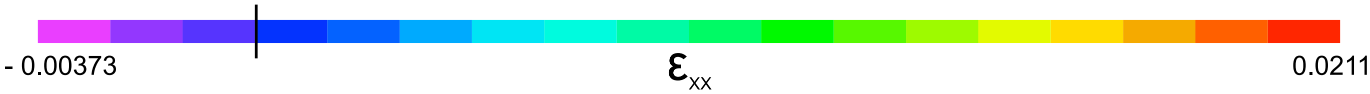

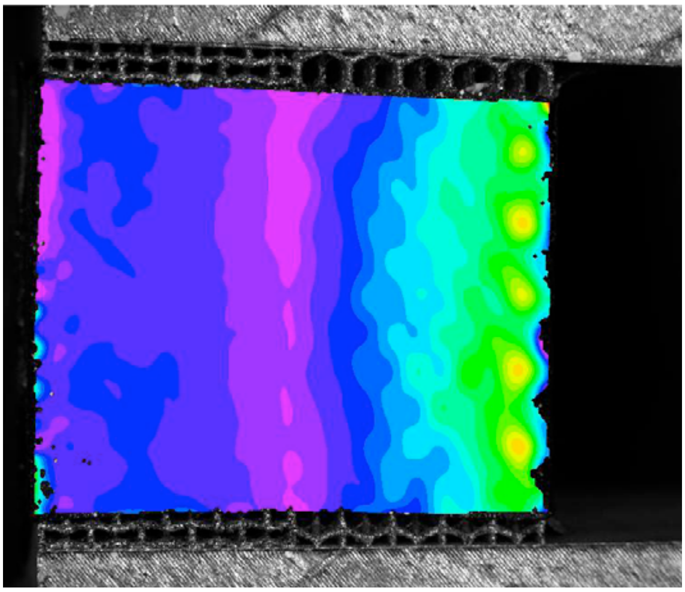

HYBRID TYPE 4 - SAMPLE #3

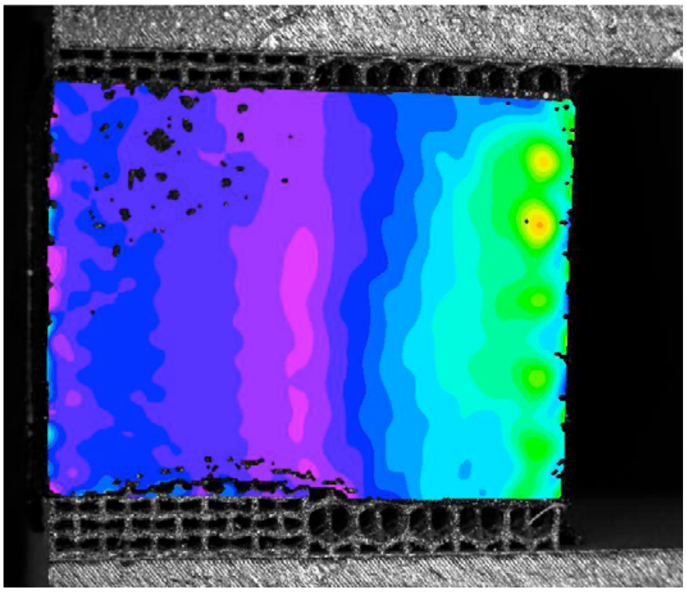

HYBRID TYPE 4 - SAMPLE #4

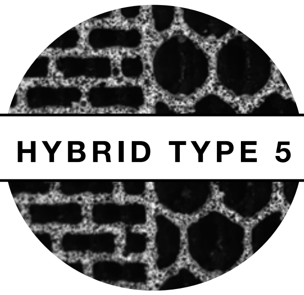

HYBRID TYPE 5

HYBRID TYPE 5 - SAMPLE #1

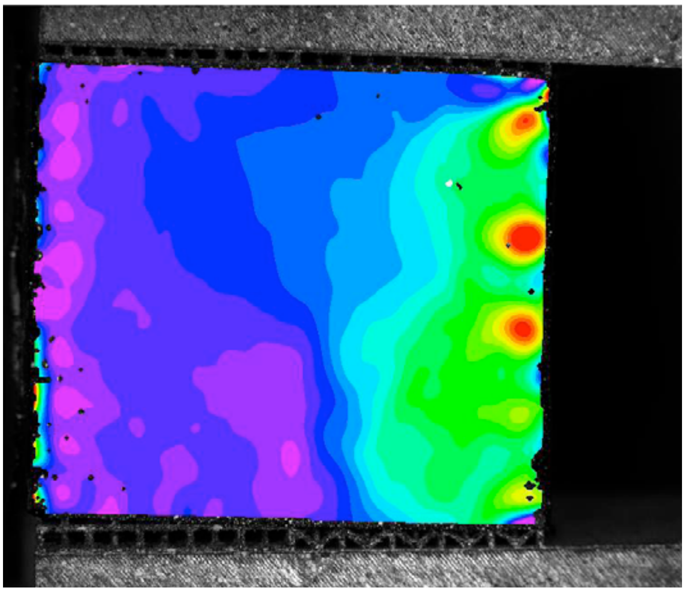

HYBRID TYPE 5 - SAMPLE #2

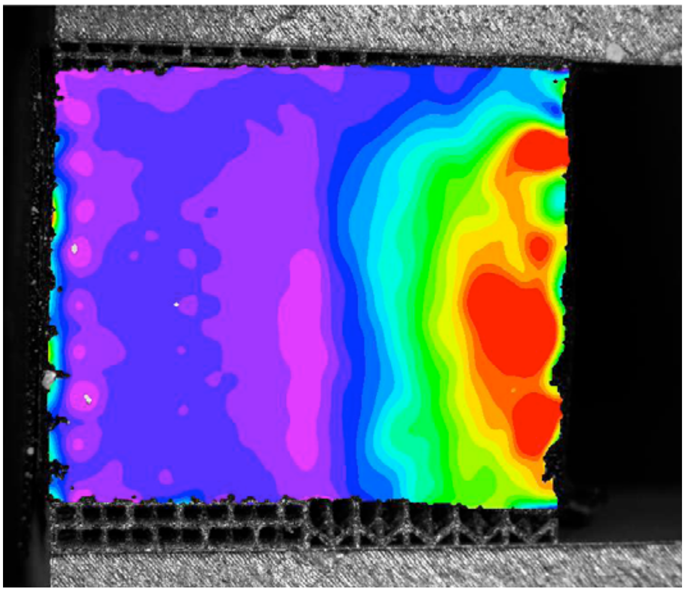

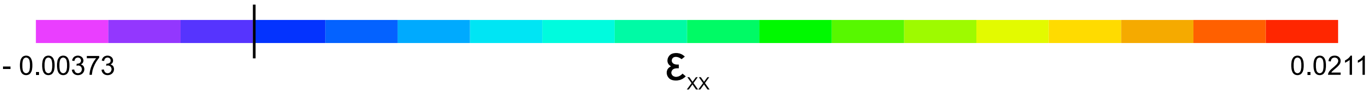

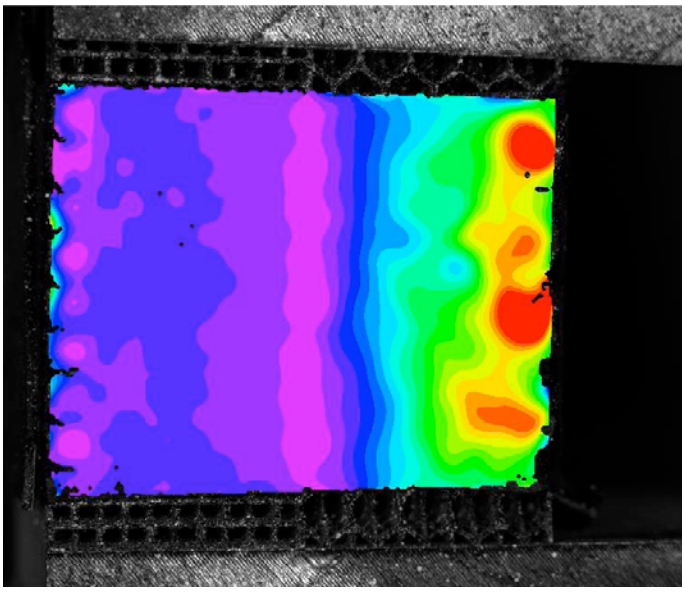

HYBRID TYPE 5 - SAMPLE #3

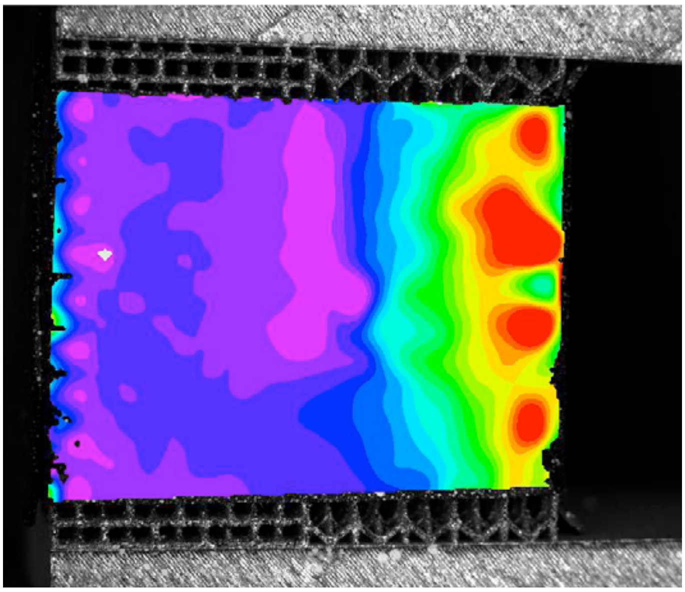

HYBRID TYPE 5 - SAMPLE #4

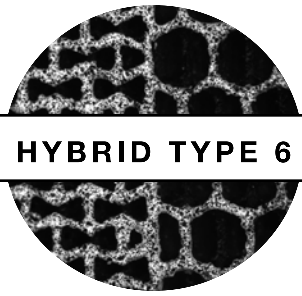

HYBRID TYPE 6

HYBRID TYPE 6 - SAMPLE #1

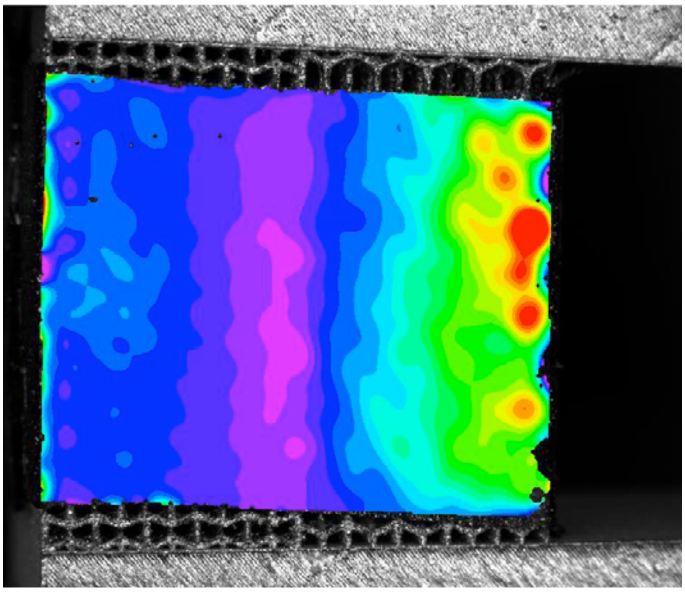

HYBRID TYPE 6 - SAMPLE #2

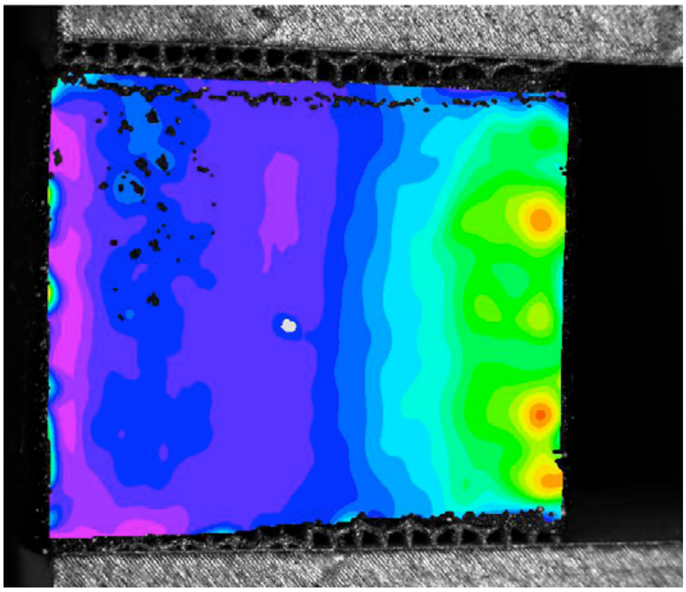

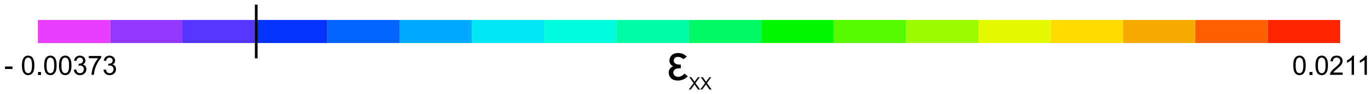

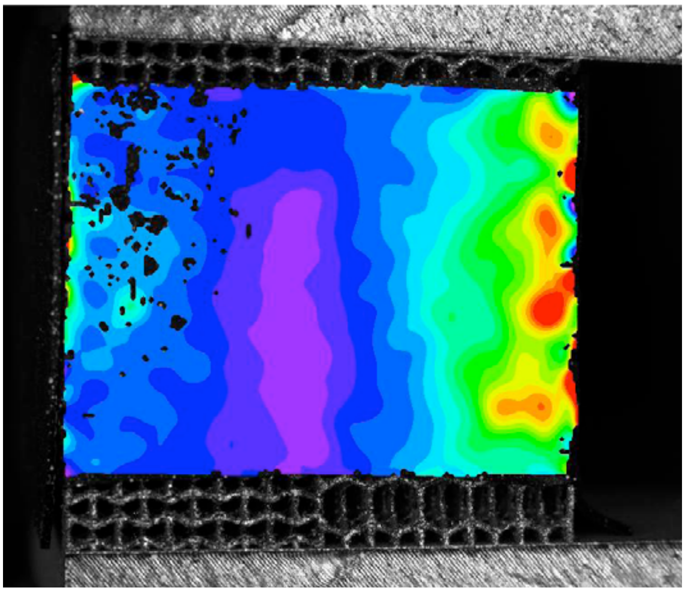

HYBRID TYPE 6 - SAMPLE #3

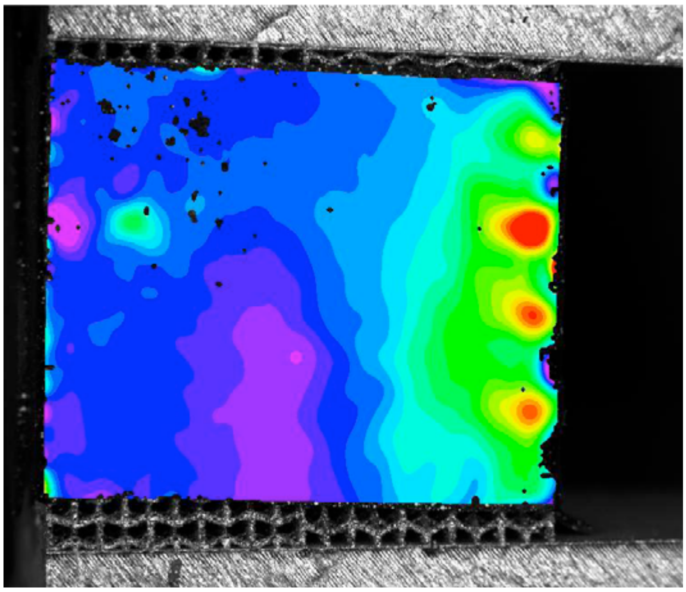

HYBRID TYPE 6 - SAMPLE #4

8.4 DIC RESULTS - META-IMPLANTS

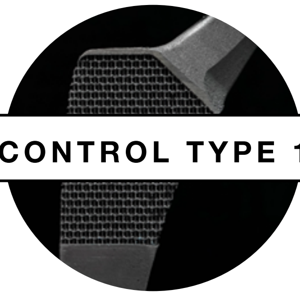

CONTROL TYPE 1

CONTROL TYPE 1 - SAMPLE #1

CONTROL TYPE 1 - SAMPLE #2

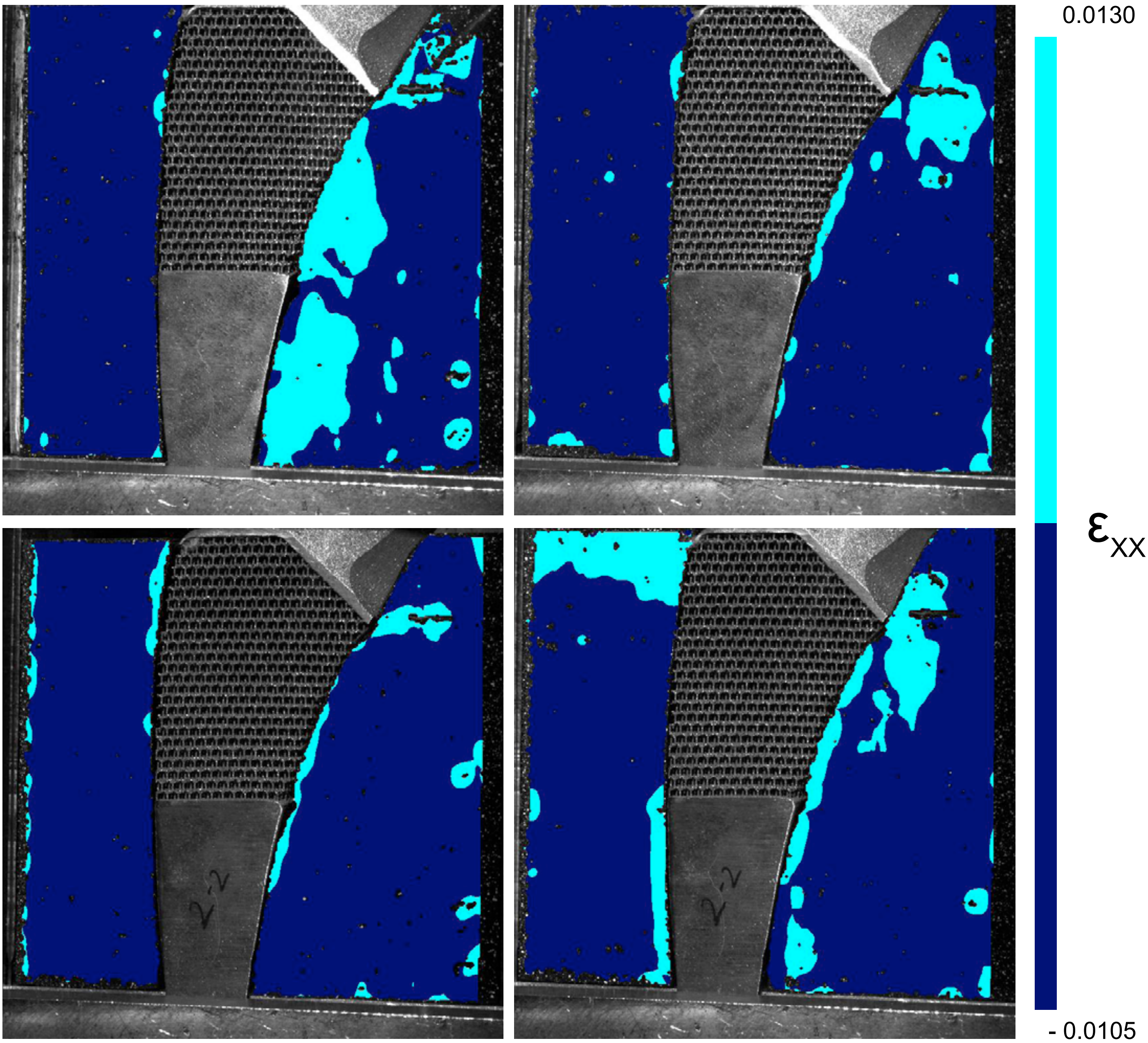

CONTROL TYPE 1 - SAMPLE #3

CONTROL TYPE 1 - SAMPLE #4

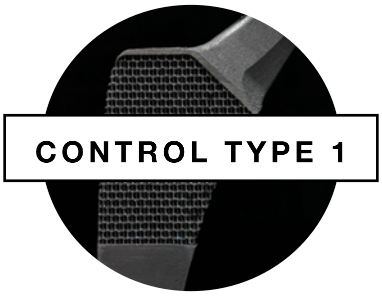

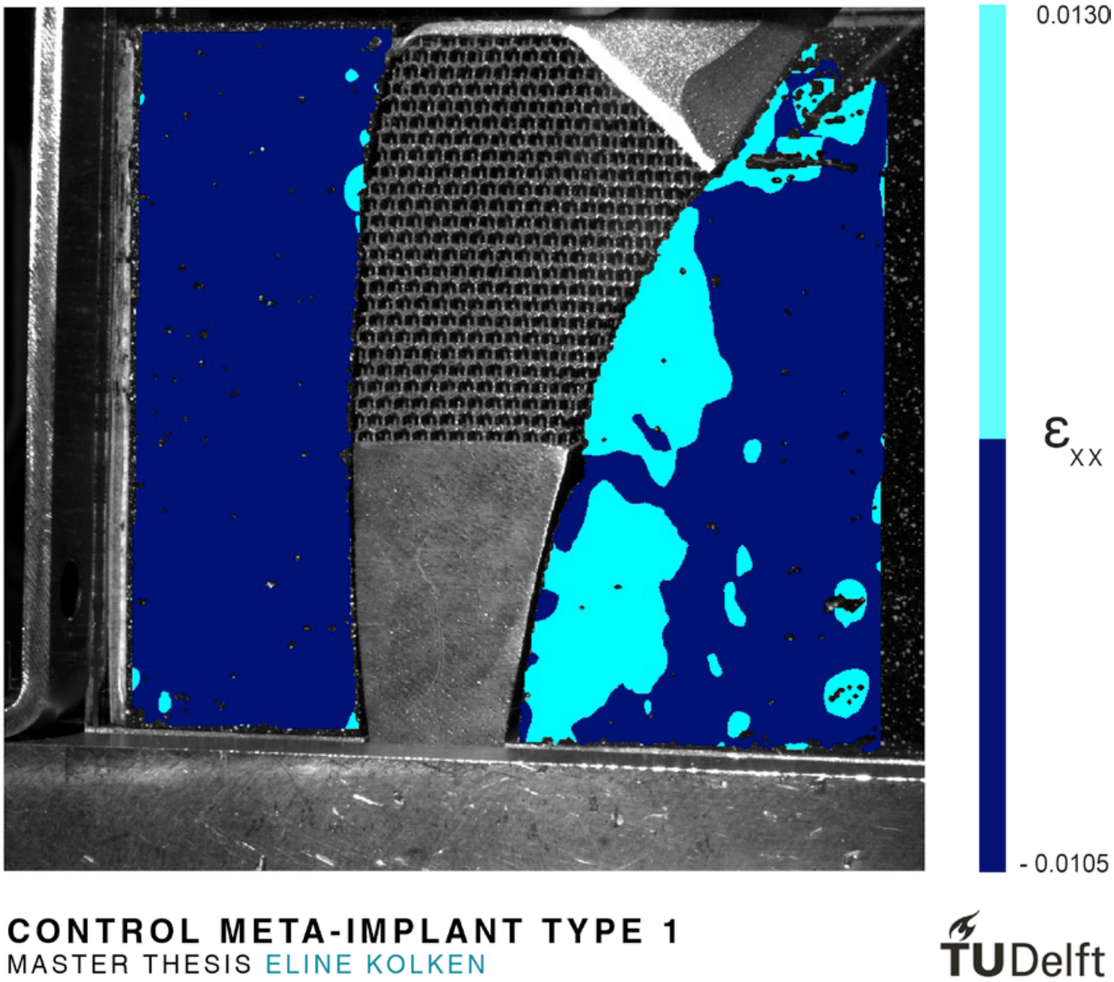

Video A13: Horizontal strain distribution in the foam surrounding Control meta-implant Type 1
- Press to play -

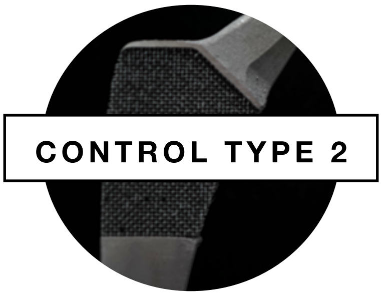
CONTROL TYPE 2

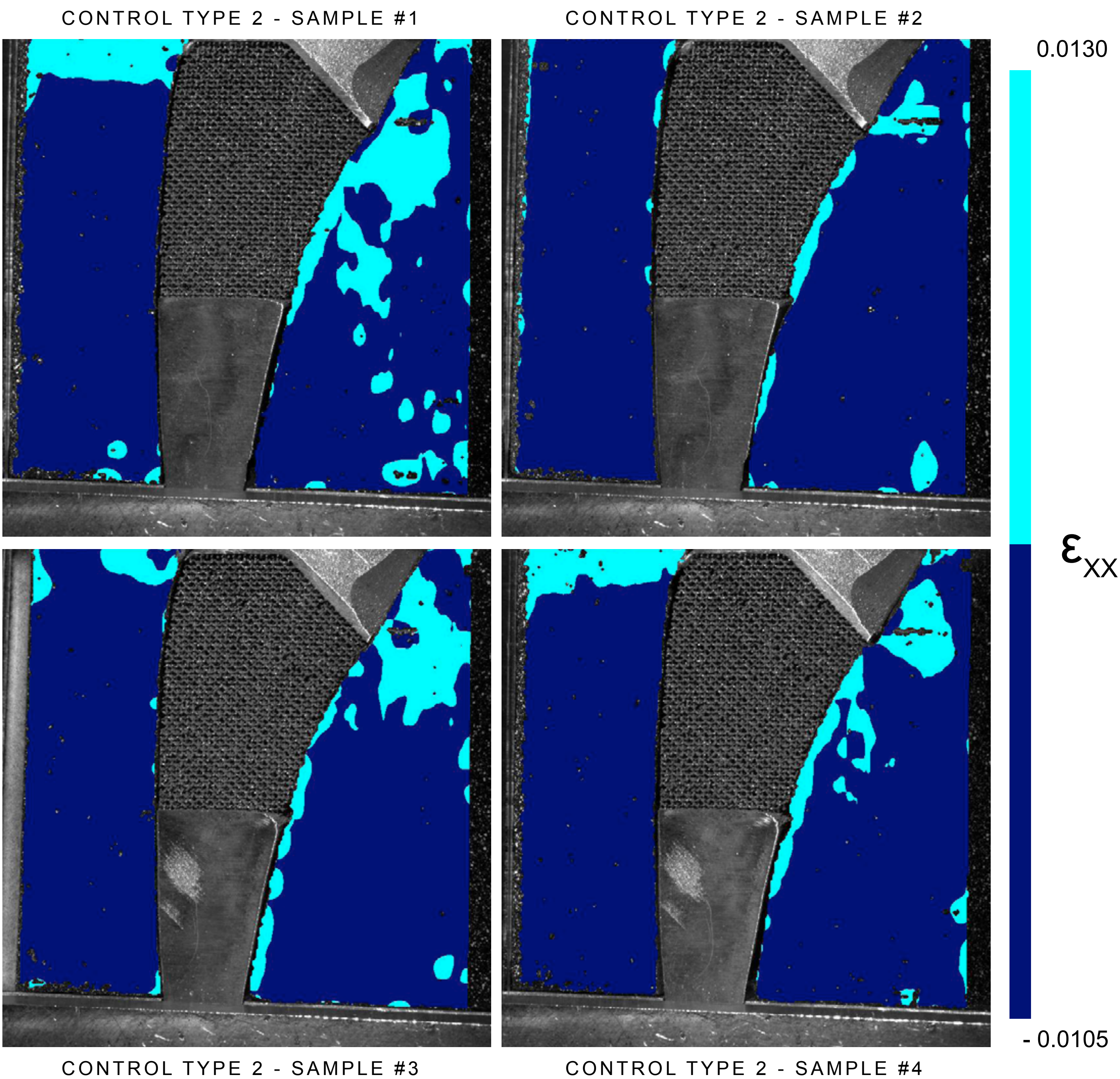
CONTROL TYPE 2 - SAMPLE #1
CONTROL TYPE 2 - SAMPLE #2
0.0130
ε_{XX}
- 0.0105
CONTROL TYPE 2 - SAMPLE #3
CONTROL TYPE 2 - SAMPLE #4

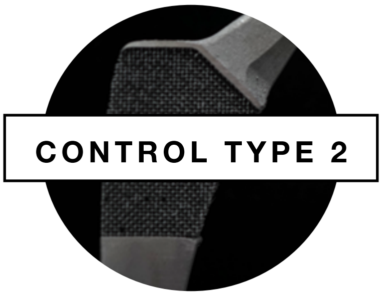

CONTROL TYPE 2

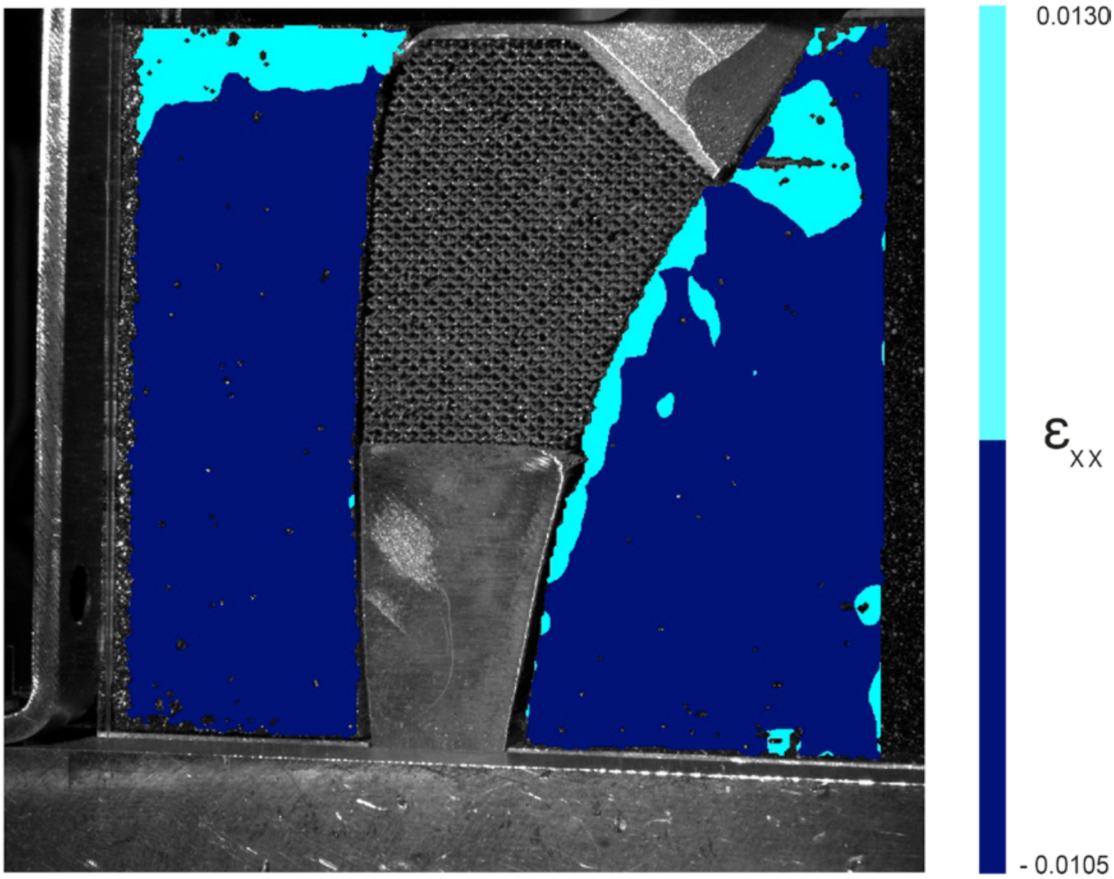

CONTROL META-IMPLANT TYPE 2
MASTER THESIS ELINE KOLKEN

Video A14: Horizontal strain distribution in the foam surrounding Control meta-implant Type 2 - Press to play -

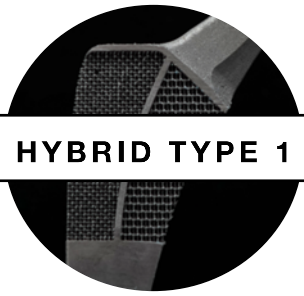

HYBRID TYPE 1

HYBRID TYPE 1 - SAMPLE #1

HYBRID TYPE 1 - SAMPLE #2

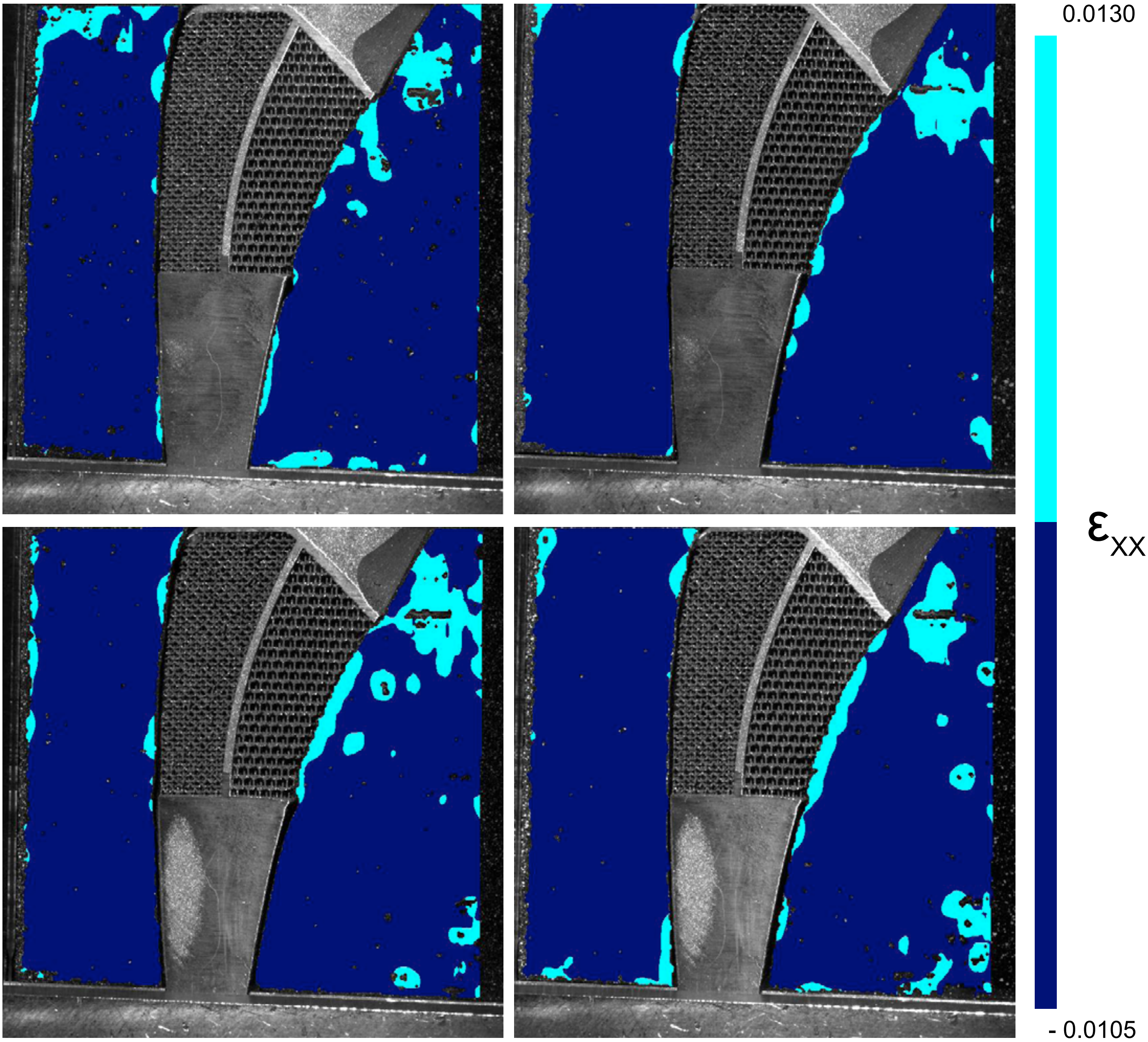

HYBRID TYPE 1 - SAMPLE #3

HYBRID TYPE 1 - SAMPLE #4

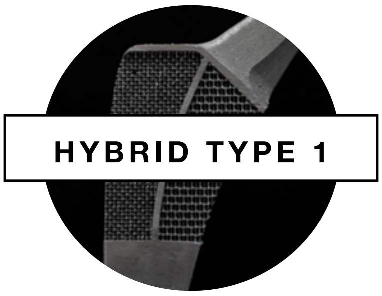

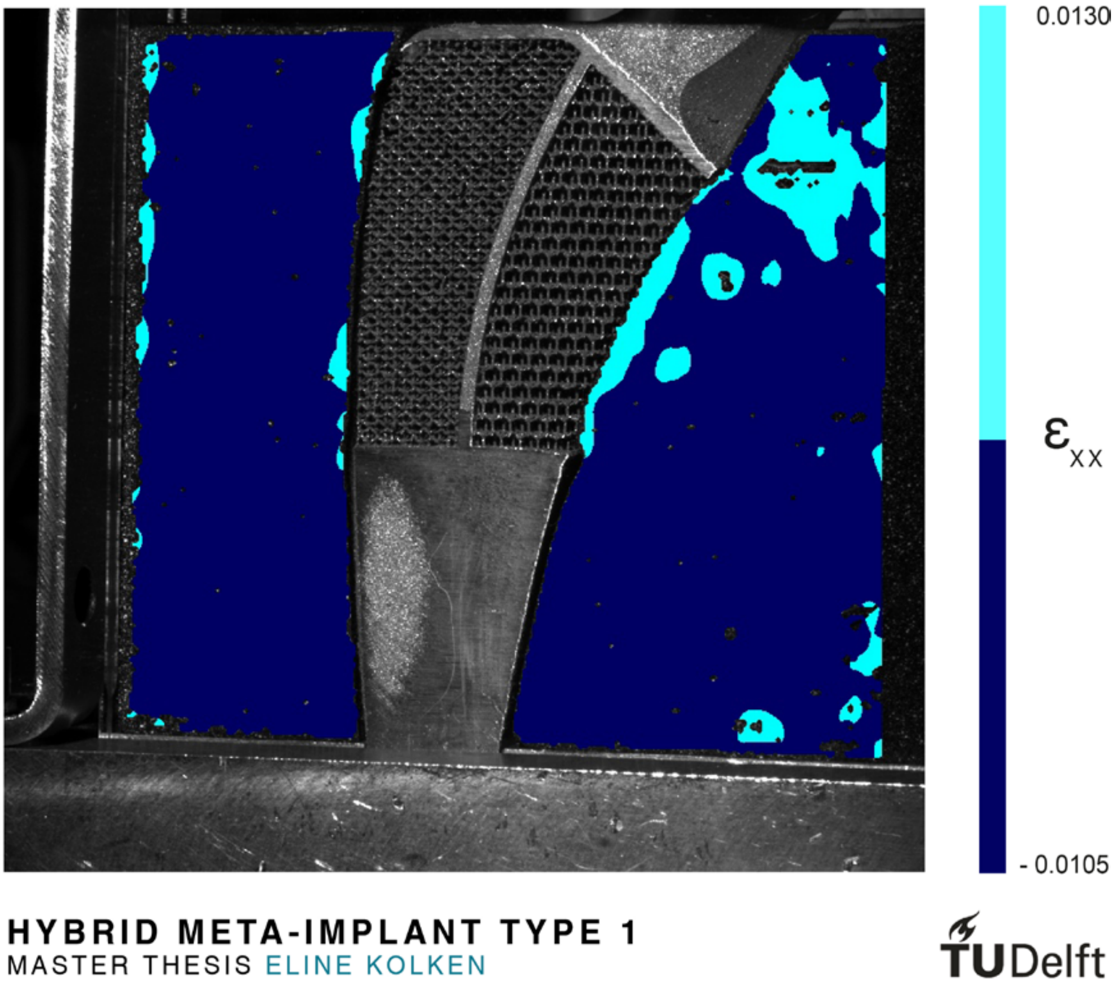

Video A15: Horizontal strain distribution in the foam surrounding Hybrid meta-implant Type 1
- Press to play -

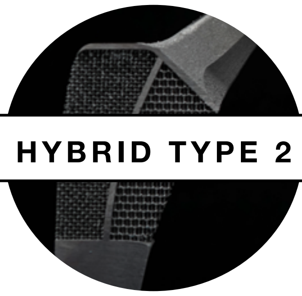

HYBRID TYPE 2

HYBRID TYPE 2 - SAMPLE #1 HYBRID TYPE 2 - SAMPLE #2

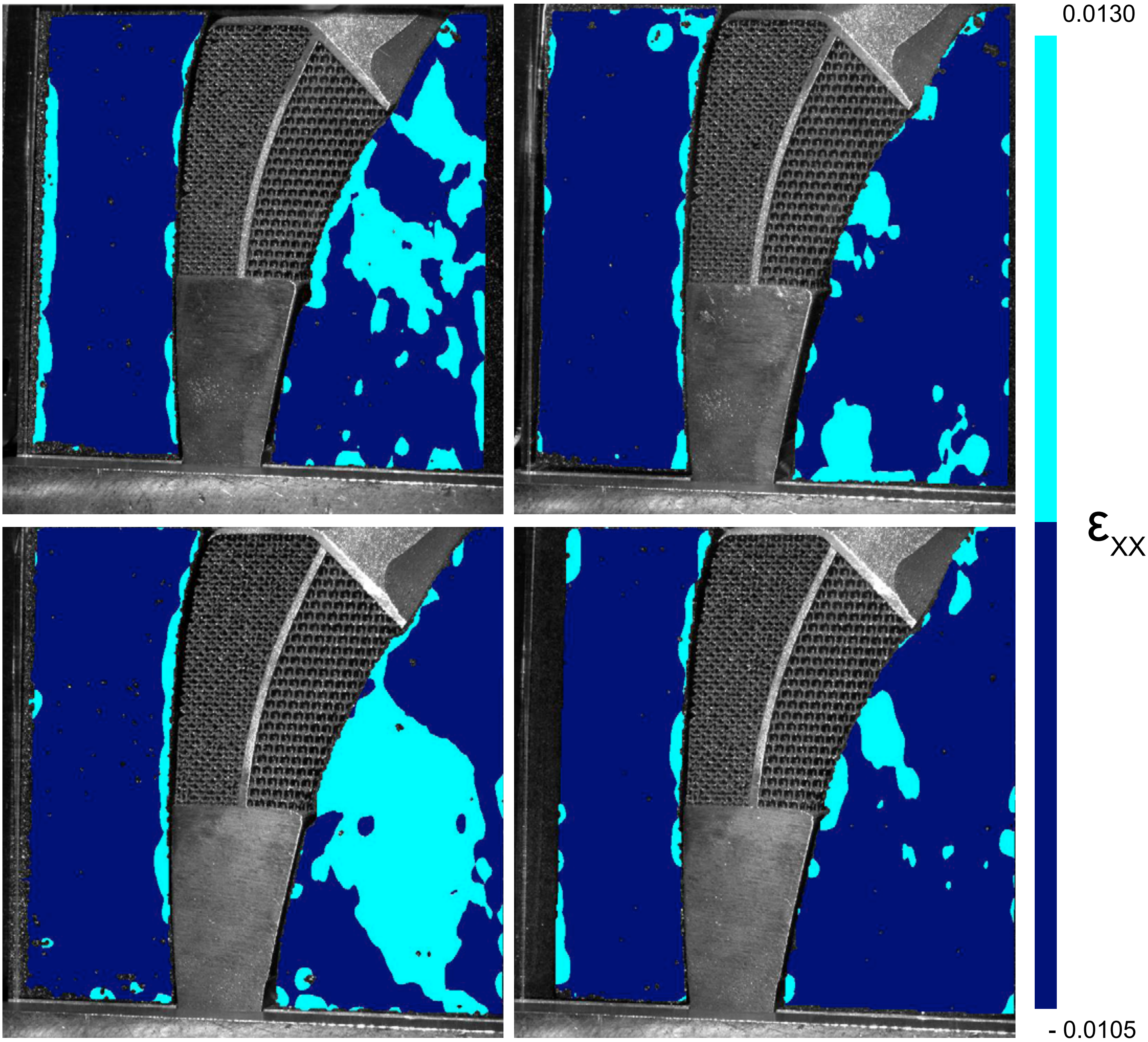

HYBRID TYPE 2 - SAMPLE #3 HYBRID TYPE 2 - SAMPLE #4

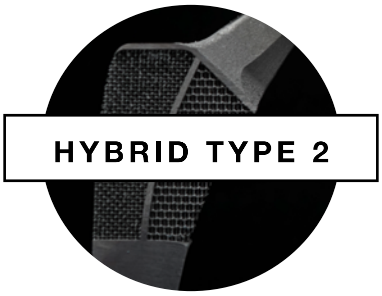

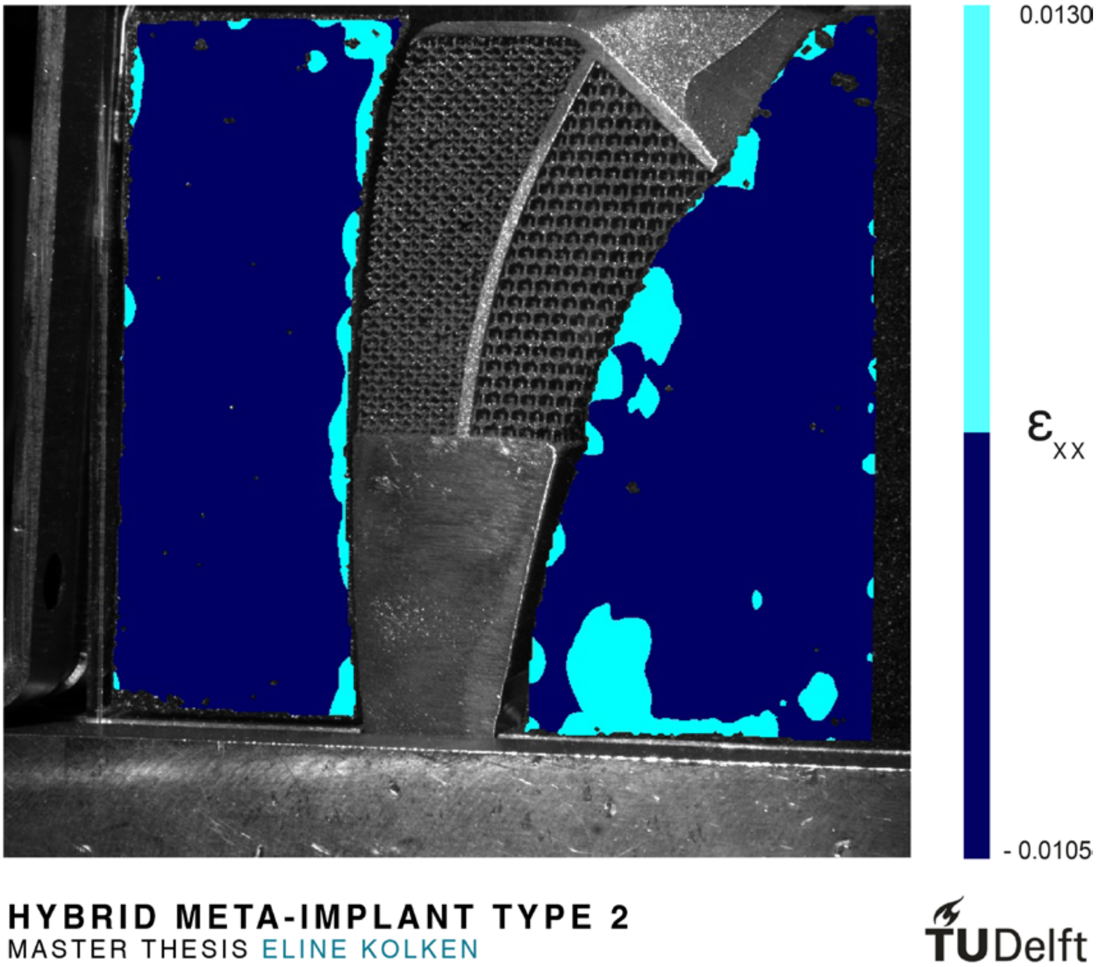

Video A16: Horizontal strain distribution in the foam surrounding Hybrid meta-implant Type 2
- Press to play -

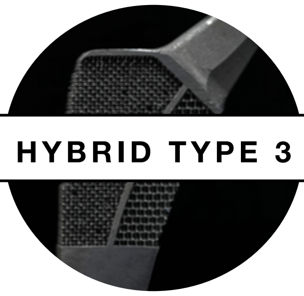

HYBRID TYPE 3

HYBRID TYPE 3 - SAMPLE #1 HYBRID TYPE 3 - SAMPLE #2

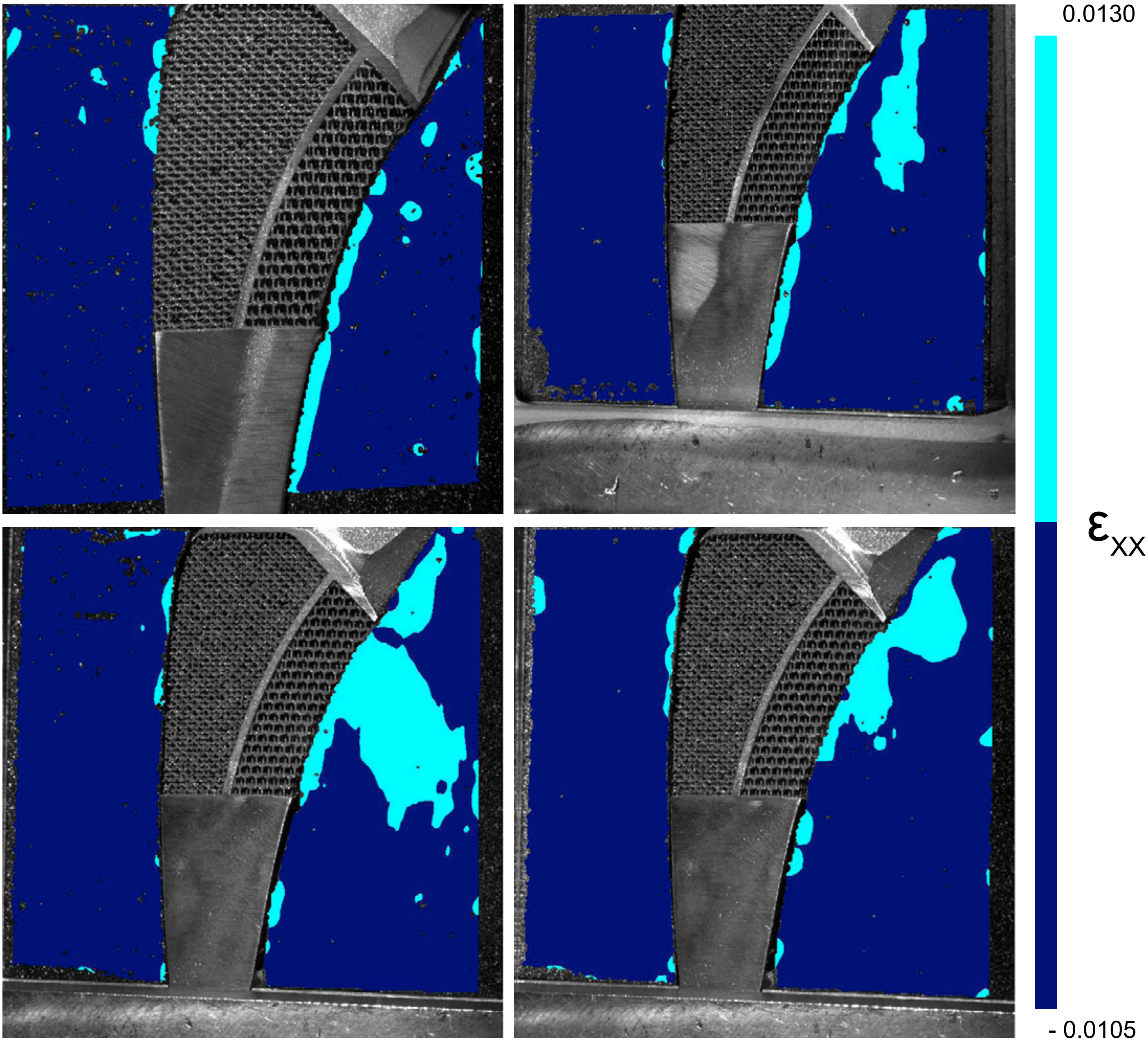

HYBRID TYPE 3 - SAMPLE #3 HYBRID TYPE 3 - SAMPLE #4

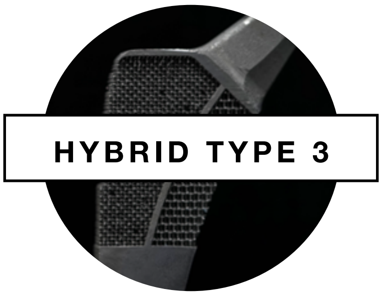

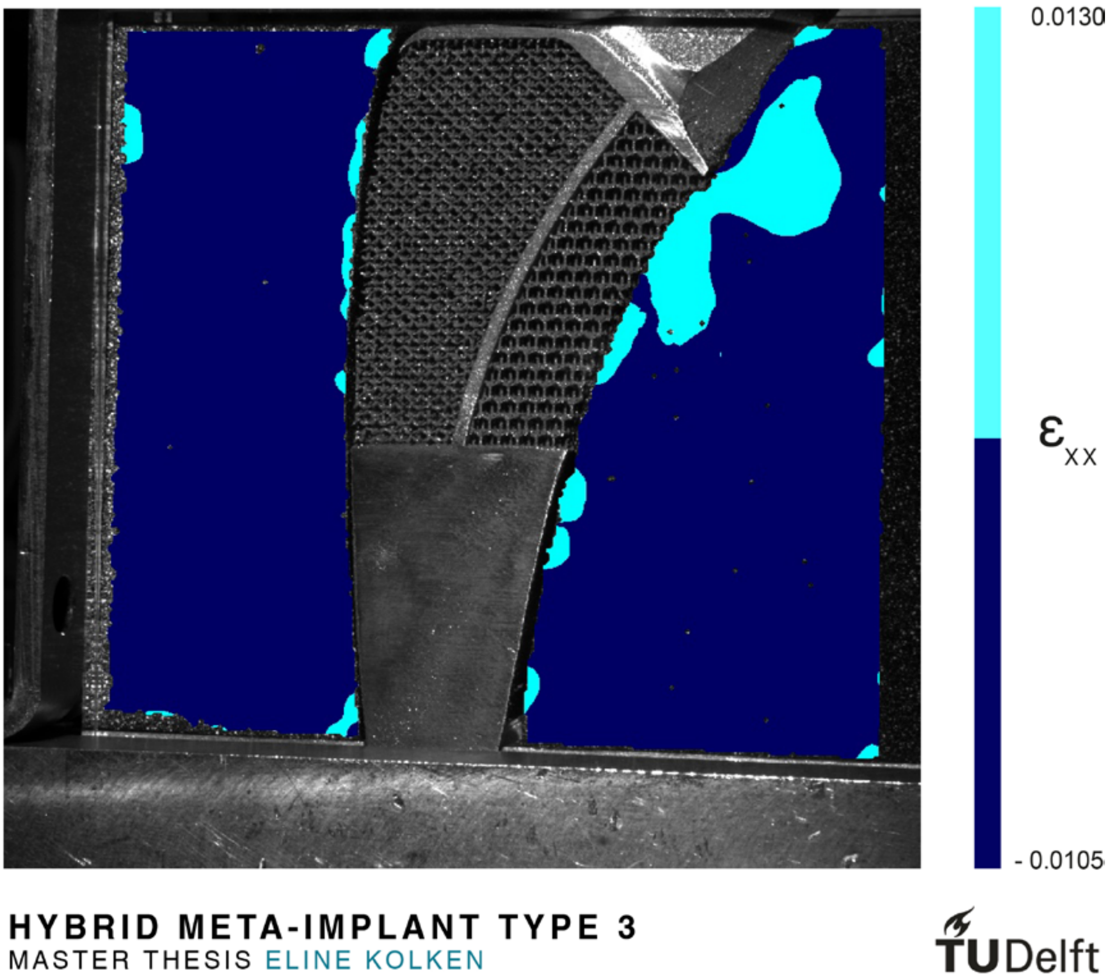

Video A17: Horizontal strain distribution in the foam surrounding Hybrid meta-implant Type 3
- Press to play -